DEVELOPMENT OF HIGH SPEED VIDEO IMAGING AS A PROCESS ANALYTICAL TECHNOLOGY (PAT) TOOL

WANG LIKUN

(B.Eng. (Hons.),Zhejiang University)

A THESIS SUBMITTED

FOR THE DEGREE OF DOCTOR OF PHILOSOPHY

DEPARTMENT OF PHARMACY

NATIONAL UNIVERSITY OF SINGAPORE

2010

ACKNOWLEDGEMENTS

First, I would like to express my appreciation to Associate Professor Paul Heng and Dr. Celine Liew. This thesis would have not been possible without their patient guidance, inspiration and strong support from the initial to the final level. I learnt not only knowledge but also visions from them.

I am grateful to be a recipient of National University of Singapore (NUS) research scholarship, which supported my postgraduate life in Singapore in the last 4 years and allowed me to focus on my research work.

It is a pleasure for me to express thanks to Ms Teresa Ang and Ms Wong Mei Yin, who have consistently provided technical support in the last 4 years. I owe my deep gratitude to Dr. Elaine Tang, who gave valuable advice, guidance and encouragement in the initial stage of my PhD work. I also would like to thank Mr. Yeo Eng Hee from NUS Computer Centre for his dedication in the maintenance of the Matlab distributed computing clusters.

I am indebted to many of my colleagues and friends for their invaluable support and for making my postgraduate life more interesting and memorable.

Last but not least, I would like to show my gratitude to my family, especially Iris, for their love.

Likun, September 2010

TABLE OF CONTENTS

ACKNOWLEDGEMENTS ..... **i**

SUMMARY ..... **vi**

LIST OF TABLES ..... **vii**

LIST OF FIGURES ..... **viii**

LIST OF SYMBOLS ..... **xiii**

CHAPTER 1. INTRODUCTION **1**

1.A. Overview of multiparticulate dosage forms **4**

1.B. Manufacture of multiparticulate dosage forms **6**
1.B.1. Pelletization 6
1.B.1.1. Extrusion-spheronization 7
1.B.1.3. High shear pelletization 11
1.B.1.4. Hot melt extrusion 13
1.B.2. Coating of pellets 14
1.B.2.1. Top spray fluid bed coating 14
1.B.2.2. Bottom spray fluid bed coating 16
1.B.2.3. Tangential spray fluid bed coating 18
1.B.2.4. Huttlin™ fluid bed coating 19

1.C. Quality frameworks for solid dosage form manufacture **20**
1.C.1. Quality by test 20
1.C.2. Quality by design 21

1.D. Process analytical technologies **22**
1.D.1. General control theory 23
1.D.2. Classification of process analyzers 25
1.D.3. Roles of in-process material flow pattern in pharmaceutical processes 27
1.D.4. Visiometric process analyzer & its potential applications 28

1.E. Research gaps in extrusion-spheronization **31**
1.E.1. Particle growth kinetics of spheronization process 33
1.E.2. Relationship between particle motion in the near plate region and particle growth kinetics 36
1.E.3. Relationship between bed surface flow pattern and particle growth kinetics 36

1.F. Research gaps in bottom spray fluid bed coating **37**
1.F.1. Particle recirculation within the partition column 38
1.F.2. The mechanism of particle recirculation within the partition column 40
1.F.3. Particle mass flow rate 40
1.F.4. Annular bed flow pattern 41

CHAPTER 2. HYPOTHESIS AND OBJECTIVES 43

2.A. Hypothesis 44

2.B. Objectives 45

CHAPTER 3. EXPERIMENTAL WORKS 48

3.A. Material 49
3.A.1. Materials for extrusion-spheronization 49
3.A.2. Materials for bottom spray fluid bed coating study 49

3.B. Development of visiometric process analyzer 49
3.B.1. High speed video imaging 50
3.B.2. Particle image velocimetry 50
3.B.3. Morphological image processing 53

3.C. Methods for investigations on the spheronization process 55
3.C.1. Extrusion-spheronization 55
3.C.2. Determination of particle growth kinetics during spheronization 56
3.C.2.1. High speed video imaging 56
3.C.2.2. Particle sizing using Ferret diameter determination of in-process high speed images 58
3.C.2.3 Verification of Ferret diameter measurement 58
3.C.3. Quantification of particle motion in the near plate region in relation to particle growth kinetics and mechanisms 60
3.C.3.1. Development of visiometric process analyzer 60
3.C.3.2. Calculation of mean particle speed (***Vtotal***) and granular temperature (***GTtotal***) in the near plate region 60
3.C.3.3. Visualization of total mean speed (***Vtotal***) and total mean granular temperature (***GTtotal***) in the near plate region 62
3.C.3.4. Particle speed distribution within the fluidization zone 64
3.C.4. Quantification of bed surface flow pattern in relation to particle growth kinetics 65
3.C.4.1. Development of visiometric process analyzer 65
3.C.4.2. Visualization of bed surface flow pattern and particle growth kinetics using 3D scatter plot 67

3.D. Methods for investigations on bottom spray fluid bed coating process 67
3.D.1. Development of visiometric process analyzer for quantification of particle recirculation probability within the partition column 67
3.D.1.1. High speed video imaging of particles moving within the partition column 67
3.D.1.2. Morphological image processing 68
3.D.1.3. Ensemble correlation PIV 69
3.D.1.4. Verification of particle displacement PDF by image tracking 70
3.D.2. Mechanisms of particle recirculation within the partition column 71
3.D.2.1. Base-coating of sugar pellets 71
3.D.2.2. Configuration of visiometric process analyzer for quantification of particle recirculation probability within the partition column 71
3.D.2.3. Estimation of voidage within the partition column 73
3.D.2.4. Air velocity measurement 74
3.D.2.5. Single particle terminal velocity calculation 75
3.D.2.6. Assessment of the extent of spray drying effect during coating 76

3.D.3. Development of visiometric process analyzer for particle mass flow rate measurement in the fountain region 77
3.D.4. Influence of annular bed flow patterns on coat uniformity 79
3.D.4.1. Production of seed pellets for high speed video imaging 79
3.D.4.2. Development of visiometric process analyzer for annular bed detection 79
3.D.4.3. Measurement of particle recirculation probability within the partition column 80
3.D.4.4. Characterization of coating performance using colour coating and tristimulus colourimetry 80
3.D.4.4.1. Colour coating 80
3.D.4.4.2. Tristimulus colourimetry and statistical analysis of colour variance of in-process samples 81

CHAPTER 4. RESULTS AND DISCUSSION 84

4.A. Particle growth kinetics in the spheronization process 85
4.A.1. Verification of Ferret diameter measurement technique for particle size distribution determination 85
4.A.2. Refined model for particle growth kinetics 88

4.B. Relationship between particle motion in the near plate region and particle growth kinetics 93
4.B.1. "Dual kinetic zones" particle flow structure in the near plate region 93
4.B.2. Relationship between mean speed profile in the near plate region and particle growth kinetics 95
4.B.3. Relationship between mean granular temperature profile and particle growth kinetics in the near plate region 99
4.B.4. Particle speed distribution within the fluidization zone 102

4.C. Relationship between bed surface flow pattern and particle growth kinetics during spheronization 107
4.C.1. Effect of velocity vector filtering 107
4.C.2. Relationship between bed surface mean speed and particle growth kinetics 109
4.C.3. Possibility of using of bed surface flow pattern for spheronization process monitoring 112

4.D. Development of visiometric process analyzer for quantifying particle recirculation within the partition column of the bottom spray fluid bed coater 113
4.D.1. Advantages of visiometric process analyzer for quantifying particle recirculation probability 113
4.D.2. Samples of original and pre-processed high speed images 113
4.D.3. Effect of ensemble correlation PIV 114
4.D.4. Particle displacement probability density function verification by image tracking 115
4.D.5. Use of particle displacement PDF data 118
4.D.6. Integration of visiometric process analyzers with current feedback process analyzers 120

4.E. Mechanism of particle recirculation within the partition column of the bottom spray fluid bed coater 121
4.E.1. High speed images within the partition column 121

4.E.2. Effects and verification of particle number measurement 123
4.E.3. Recirculation probability and voidage measurement within the partition column 125
4.E.4. Air velocity within partition column, single particle terminal velocity and boundary layer thickness 127
4.E.5. Effects of meso-scale flow structure on drag force 129
4.E.6. Origins of cluster formation and breakage 131
4.E.7. Comparison with circulating fluidized bed studies 132
4.E.8. The extent of spray drying effect 134
4.E.9. Influences of cluster formation on coating process 135
4.E.10. Control of cluster formation within the partition column 137

4.F. Development of a visiometric process analyzer for measuring particle mass flow rate in the fountain region 138
4.F.1. PIV and morphological image processing results 138
4.F.2.Comparative advantages of measuring downward moving particles 139
4.F.3.Using visiometric process analyzer to investigate the role of partition gap and AAI 140
4.F.3.1. The dual role of partition gap 140
4.F.3.2. AAI diameter - the effectiveness of Venturi effect 141
4.F.4. Uses and integration of online MFR measurement 143

4.G. The influence of annular bed flow pattern on coat uniformity 144
4.G.1. Annular bed flow patterns detected using visiometric process analyzer 145
4.G.2. Coat uniformity of in-process samples 147
4.G.3. Influences of particle recirculation within partition column and particle mass flow rate on coat uniformity 149
4.G.4. Influence of annular bed flow patterns on coat uniformity 151
4.G.5. Significance of annular bed flow pattern 154
4.G.6. Feasibility of monitoring annular bed flow pattern in large scale coating process 157

CHAPTER 5. CONCLUSION 162

5.A. Spheronization process 163

5.B. Bottom spray fluid bed coating 164

5.C. Limitations and future directions 164

REFERENCES 167

LIST OF PUBLICATIONS 188

SUMMARY

This PhD project explored the development of high speed video imaging as a process analytical technology (PAT) tool for better understanding and control of two major multiparticulate manufacturing processes, i.e. extrusion-spheronization and bottom spray fluid bed coating. Particle image velocimetry and image processing were employed for analysis of high speed images to elucidate in-process material flow pattern. From the investigations on the spheronization process, a refined model of particle growth kinetics was proposed. The particle flow patterns in the near frictional base plate region and bed surface were investigated and correlated with particle growth kinetics. It was found that spheronization process monitoring and endpoint determination could be achieved by monitoring particle motion either in the near plate region or in the spheronization bed surface. In the investigations on bottom spray fluid bed coating, the particle motion in the upbed region, fountain region and annular bed region were quantified. With the developed PAT tool, cluster formation and drag reduction were found to be the mechanisms of particle recirculation within the partition column. Real-time measurement of particle mass flow rate was achieved. The influences of annular bed flow patterns on coat uniformity were also clearly demonstrated for the first time.

LIST OF TABLES

No.	Title	Page
Table 1.	Process conditions for high speed video imaging of particle motion in the partition column of the Precision coater	72
Table 2.	Process conditions for determining the extent of spray drying effect	77
Table 3.	Process parameters for MFR measurement	78
Table 4.	Process conditions for high speed video imaging and colour coating	79
Table 5.	Comparison between the riser of the circulating fluid bed and the partition column of the bottom spray fluid bed coater	134
Table 6.	Comparison between characteristics of clusters found in this investigation and those from previous reports on the circulating fluid bed	134
Table 7.	Two-sample *F-test* results for *dE* variance of in-process samples	150

LIST OF FIGURES

No.	Title	Page
Figure 1.	Role of PAT under QbD framework	3
Figure 2.	Schematic diagram of (A) single screw axial extruder, (B) counter rotating twin-screw extruder, (C) single screw radial extruder, (D) Nica™ extruder, (E) rotary-cylinder extruder, (F) rotary-gear extruder and (G) ram extruder	9
Figure 3.	Schematic diagrams of frictional base plates with (A) cross-hatched and (B) radial geometric patterns	10
Figure 4.	(A) Rotary processor in the pelletization mode, (B) rotary processor in drying/coating mode, (C) high shear pelletizer and (D) hot melt extruder	12
Figure 5.	Schematic diagram of (A) top spray, (B) bottom spray (Wurster), (C) Precision, (D) tangential, (E) FlexStream™ and (F) Huttlin™ fluid bed coaters	15
Figure 6.	Schematic diagram for ideal process control	24
Figure 7.	Combination of feedback and feedforward controllers for practical pharmaceutical process control (adapted from Koenig, 2009)	25
Figure 8.	Schematic diagram showing the principles of PIV	30
Figure 9.	Particle growth kinetics for spheronization process proposed by (A) Rowe, (B) Baert *et al.* and (C) Liew *et al.*	34
Figure 10.	(A) Ideal particle motion without recirculation, (B) actual particle motion joining recirculation within the partition column	39
Figure 11.	Schematic diagram of Matlab distributed computing cluster (adapted from the MathWorks, 2010)	52

Figure 12.	(A) Perspective view of spheronizer, (B) product discharge slot used for high speed video imaging, (C) high speed video imaging during spheronization process and (D) time sequence for high speed video imaging	56
Figure 13.	Images of (A) heat sink and cooling fan unit, and (B) 10×10 LED array mounted on the bottom of the heat sink	57
Figure 14.	Schematic diagram of high speed video imaging of spheronization bed surface	65
Figure 15.	Schematic representation of high speed video imaging system setup for capturing particle movement in the bottom spray fluid bed coater	68
Figure 16.	Flow chart of image pre-processing for images of moving particles in the partition column of the bottom spray fluid bed coater	69
Figure 17.	Procedure for ensemble correlation PIV	70
Figure 18.	(A) Time sequence for high speed video imaging of particle motion in the partition column, (B) schematic diagram of AAI with diameter of *d* mm	72
Figure 19.	Flow chart depicting different steps in obtaining the number of particles on the image	74
Figure 20.	Schematic diagram of air velocity measurement within the partition column of the Precision coater	75
Figure 21.	Schematic diagram showing the volume captured by the high speed camera for MFR measurement	77
Figure 22.	Particle size distributions measured using (A) optical microscope and Ferret mean diameter and (B) high speed imaging and Ferret diameter determination	86
Figure 23.	Changes in particle size distributions during spheronization	89
Figure 24.	Schematic diagrams of (A) refined particle growth kinetics and (B) the influences of shear energy input and material plasticity on particle growth kinetics	91

Figure 25. Sample high speed image of particle movement in the near plate region showing the "dual kinetic zones" particle flow structure 95

Figure 26. Sample dimensionless plots of (A) particle mean speed and (B) granular temperature showing the kinetic zones, and of the dimensionless distances corresponding to the end of (C) initial drop in mean speed and (D) the initial surge in granular temperature 96

Figure 27. Changes in the mean speed profile in the near plate region with respect to spheronization time and dimensionless distance from the frictional base plate 98

Figure 28. Changes in mean granular temperature profile in the near plate region with respect to spheronization time and dimensionless distance from the bottom of frictional base plate 100

Figure 29. Particle speed distributions in the fluidization zone with spheronization time 103

Figure 30. Schematic diagram of collisions between (A) coarse and fine particles and (B) coarse and coarse particles 104

Figure 31. Changes in particle speed distributions during the spheronization process (dots) and the fitness to Maxwell (dotted lines) and Gaussian (solid lines) distributions, respectively 105

Figure 32. (A) Decomposition of relative velocity and (B) schematic diagram showing elastic, inelastic and highly inelastic collisions 107

Figure 33. Sample results from the different steps of velocity vector filtering to detect the ring shaped spheronization bed surface 108

Figure 34. Changes in bed surface mean speed with respect to spheronization time and mean particle size 110

Figure 35. (A) Sample of original image from high speed video clips (recording speed: 4219 fps), (B) sample of pre-processed image (air flow rate: 90 m^3/h, atomizing air pressure: 1.5 bar) 114

Figure 36.	Correlation results from (A) a single pair of frames, (B) 20 image pairs, (C) 100 image pairs, and (D) 500 image pairs	115
Figure 37.	Contour plots of particle displacement PDF from (A) ensemble correlation PIV results without image pre-processing, (B) validation data after tracking of 1000 randomly selected particles and (C) ensemble correlation PIV result after image pre-processing	117
Figure 38.	(A) Particle velocity magnitude histograms under atomizing air pressure of 1.5 bar and air flow rates of (i) 80 m^3/h, (ii) 90 m^3/h, (iii) 100 m^3/h; and (B) particle velocity orientation histograms under atomizing aire pressure of 1.5 bar and air flow rates of (i) 80 m^3/h, (ii) 90 m^3/h, (iii) 100 m^3/h	119
Figure 39.	High speed images showing aggregate formation within the partition column	122
Figure 40.	Flow chart with sample images depicting the different steps in morphological image processing for particle number measurement	124
Figure 41.	Verification (○) and morphological image processing results (Δ) for particle number detection	125
Figure 42.	(A) Particle recirculation probability and (B) average voidage within the partition column for (i) 355-425 μm, (ii) 500-600 μm and (iii) 710-850 μm particles	126
Figure 43.	Time series (A) particle recirculation probability, (B) voidage and (C) vertical velocity component of (i) 355-425 μm, (ii) 500-600 μm and (iii) 710-850 μm particles, respectively	128
Figure 44.	Air velocity measurement results within the partition column	129
Figure 45.	Schematic diagram of a typical circulating fluid bed	133
Figure 46.	The extent of spray drying effect of particles with three different size fractions	135

Figure 47.	Schematic diagram showing particle movement and air flow (A) with clustering and (B) without clustering in the partition column of bottom spray fluid bed coater	136
Figure 48.	(A) Sample high speed image and (B) sample PIV results for MFR measurement	138
Figure 49.	(A) Influences of partition gap and air flow rate on particle MFR; (B) influences of atomizing air pressure and AAI diameter on particle MFR	141
Figure 50.	Sample high speed image of annular bed flow	145
Figure 51.	(A) Sample PIV results of annular bed flow using (i) AAI-20, (ii) AAI-24 and (iii) AAI-30; (B) sample streamlines from PIV results using (i) AAI-20, (ii) AAI-24 and (iii) AAI-30	146
Figure 52.	(A) Trends of mean colour difference ($\overline{dE}$) and (B) mean relative colour variation (RCV) of in-process samples obtained from AAI-20, AAI-24 and AAI-30	147
Figure 53.	Schematic representation of annular bed flow regimes with their influences on coating performance	157
Figure 54.	PIV results from 10 cm by 10 cm observation window of (A) global fluidization, (B) localized fluidization and (C) plug flow at time point of (i) 0 ms, (ii) 20 ms and (iii) 40 ms	158
Figure 55.	Scatter plot of time series velocity vectors from three randomly chosen locations (i, ii and iii) under (A) global fluidization, (B) localized fluidization and (C) plug flow	159

LIST OF SYMBOLS

a	Parameter to be fitted in Maxwell distribution
$a_1, b_1, c_1, a_2, b_2, c_2$	Parameter to be fitted in Gaussian distribution
AAI	Air accelerator insert
ANOVA	Analysis of variance
b	Structuring element
c_i	The fluctuating speed of the i^{th} speed with respect to the mean speed
$c_{II}(\Delta x,\Delta y)$	2D cross-correlation coefficient at displacement of($\Delta x,\Delta y$)
dE	Colour difference in the CIE Lab colour space
d_j	A position that is d_j mm away from the frictional base plate
d_p	Particle diameter (μm)
C_D	Drag coefficient of a single particle
$C_{MQD}(\Delta x,\Delta y)$	Quadratic difference at the displacement of($\Delta x,\Delta y$)
$\overline{dE}$	The mean colour difference
D	Position matrix
D_b	Domain of structuring element b
DC	Direct current
D_e	Diameter of partition column
DoE	Design of experiments
$\vec{e}$	Unit vector pointing from particle #2 to particle #1

E	Mean operator
$E(t)$	Mean particle cycle-time (s)
f	Digital image for morphological image processing
$f \oplus b$	Gray-scale dilation
$f \ominus b$	Gray-scale erosion
$f \circ b$	Gray-scale opening
fps	Frames per second
FBRM	Focused beam reflectance measurement
F_D	Drag force (N)
F_{d0}	The drag force without considering multi-particle effect
FDA	Food and Drug Administration
F_{deff}	The effective drag force when multi-particle effect is considered
$\overrightarrow{g_{12}}^{n}$	Normal component of $\overrightarrow{v_{12}}$ with respect to $\overrightarrow{r_{12}}$
$\overrightarrow{g_{12}}^{t}$	Tangential component of $\overrightarrow{v_{12}}$ with respect to $\overrightarrow{r_{12}}$
g	Acceleration of gravity (9.81 m^2/s)
GT	Granular temperature
GT^t	Granular temperature of near plate region at time t ($m \times 1$ vector)
GT^{total}	A matrix containing GT^t of all 30 time points during spheronization ($m \times 30$ matrix)
H	Digital image after thresholding
HPMC	Hydroxypropyl methylcellulose

I	The first digital image of the image pair for PIV analysis
I'	The second digital image of the image pair for PIV analysis
$I(i,j)$	Intensity of pixel located at (i,j) of image I
K	Extent of spray drying effect (%)
LED	Light emitting diode
(L_c, a_c, b_c)	The colour of coated particle in CIE Lab colour space
(L_u, a_u, b_u)	The colour of uncoated particle in CIE Lab colour space
M	Mass of a single particle (g)
m_c	The weight of dry coating material applied to particles
m_f	The final particle weight after coating (g)
m_i	The initial particle weight before coating (g)
mpz_t	The mean particle size at time t
M	Number of pixels along vertical direction of template
M_t	Load of particles (g)
MCC	Microcrystalline cellulose
MFR	Mass flow rate (g/s)
MQD	Minimum quadratic difference
N	The number of particles used in colourimetry
N	Number of pixels along horizontal direction of template
N_p	Particle number

NIR	Near infrared
$p(v)$	Probability of particles with certain speed v
PAT	Process analytical technologies
PDF	Probability density function
PEPT	Positron emission particle tracking
PFFR	Particle-fluid flow ratio
PID	Proportional–integral–derivative
PIV	Particle image velocimetry
Q	Number of fluctuating velocities used in granular temperature calculation
QbD	Quality by design
QbT	Quality by test
$\overrightarrow{r_{12}}$	The vector joining the centres of particle #1 and particle #2
RCV	Relative colour variance
Re	Reynolds number
RMSE	Root mean squared error
S_m	Measured cross-sectional area
SR	Spray rate (g/min)
S_t	Total cross-sectional area of product chamber
Std(t)	Standard deviation of particle cycle-time
STSO	Time series velocity orientation

T	Time (s)
T	Threshold in thresholding operation
$T_{coating}$	Coating duration (s)
$\bar{v}$	Mean speed
$\overrightarrow{v_1}$	Velocity of particle # 1
$\overrightarrow{v_{12}}$	Relative velocity between particle #1 and particle #2
$\overrightarrow{v_2}$	Velocity of particle # 2
v_i	The i^{th} detected speed
v_{ij}^k	Speed detected at position d_{ij}
v_s	Relative velocity between particle and fluid (m/s)
V_p	The volume of a single particle (cm^3)
$Var(t)$	The variance of particle cycle-time
Var_{coat}	Coat variance due to particle cycle-time distribution
V_c	The total volume captured by the high speed camera (cm^3)
V_{peri}	Peripheral speed of spheronizer frictional base plate (m/s)
$\overline{V^{total}}$	A matrix containing $\overline{V^t}$ of all 30 time points during spheronization ($m \times 30$ matrix)
$\overline{V^t}$	Averaged speed matrix along horizontal direction at time t ($m \times 1$ vector)
$\overline{V_{surf}^t}$	Averaged particle speed on the bed surface at time t during spheronization
V_k^t	Speed matrix from the k^{th} image pair at time t
$W_{content}$	Water content (%, w/w)

x	Empirical parameter determined by particle shape, roughness, and Reynolds number respectively
Δx	Displacement along vertical direction
Δy	Displacement along horizontal direction
ε_s	Solids volume fraction in gas-solids flow
ε	Voidage in gas-solid flow
δ_b	Thickness of boundary layer (mm)
$\hat{\theta}$	Estimator
θ	Estimated parameter
μ_φ	The mean of mapped velocity orientation
μ_f	Kinematic viscosity of fluid (m^2/s)
μ_I	The average intensity of template from image I
$\mu_{I'(i+\Delta x,j+\Delta y)}$	Average intensity of I' coincident with the template I at position $(i+\Delta x, j+\Delta y)$
ρ_f	Density of fluid (g/cm^3)
$\hat{\varphi}_i$	The i^{th} velocity orientation mapped to the region between 0 to π
φ_i	Orientation of the i^{th} detected velocity

CHAPTER 1. INTRODUCTION

CHAPTER 1. INTRODUCTION

Most medicines are manufactured in solid dosage forms, e.g. mainly tablets and multiparticulates. Compared to traditional tablets, multiparticulates have advantages of lower gastric irritation, more uniform gastric transit time and less variation in drug release profiles (Hogan, 1995). Ease of coating and their suitability for use in the design of controlled release drug delivery systems are other advantages of multiparticulates.

In accordance to current good manufacturing practice, fixed process parameters are used during the manufacturing of multiparticulates. The decision for the release of the whole batch of products is solely dependent on the test results from a limited number of final product samples (Nasr, 2006). Hence, the current quality control system is also referred to as a quality by test (QbT) system. It has the following limitations. Firstly, use of fixed process parameters directly transfers the batch variations of raw materials into quality variations in the end-product. Secondly, the test results from a limited number of samples may not be representative and thus, may not reflect the true situation of the product quality of the whole batch. Lacking fundamental understanding of the manufacturing process, the current quality system is responsible for low quality pharmaceutical products and product recalls. It was pointed out that the pharmaceutical industry is wasting over 50 billion US dollars per year due to insufficient information technology and misplaced decision making (Nasr, 2006).

In order to overcome the limitations of the current quality system, the United States Food and Drug Administration (FDA) proposed the concept of quality

by design (QbD). In the QbD framework, product quality would be assured by fundamental understanding and robust control of the manufacturing process (Yu, 2008). In order to achieve this, the mapping between process design space and critical product quality attributes needs to be established (Figure 1). The process variability sources are responsible for transferring the variation in raw material properties and process conditions into variations in the final product quality. The timely identification, quantification and control of process variability sources are achieved using process analytical technologies (PAT). PAT tools mainly include process analyzers and process control tools.

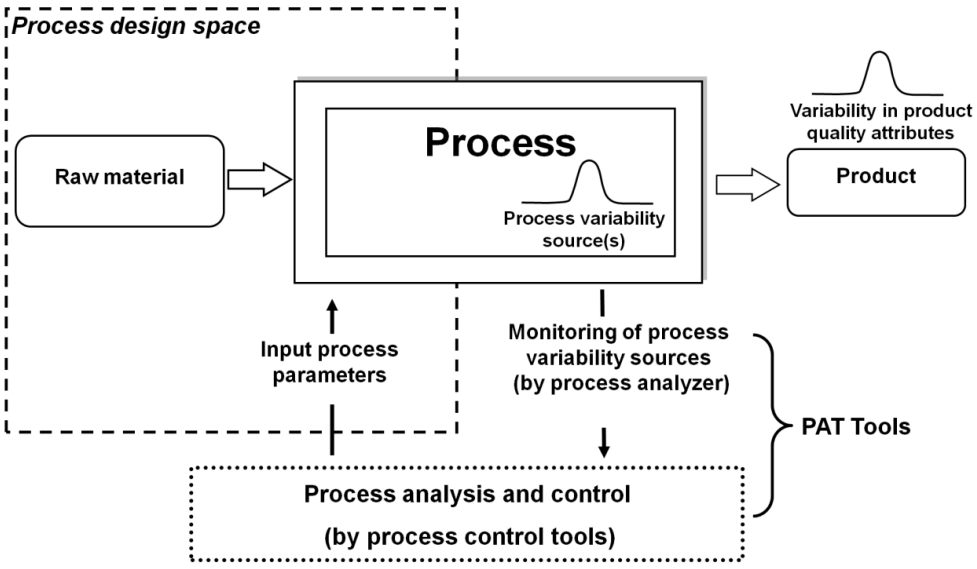

Figure 1. Role of PAT under QbD framework

In this chapter, a review of multiparticulate dosage forms and processes used in their manufacture is given followed by an introduction to QbT, QbD and PAT, and a summary of the challenges (research gaps) of changing from QbT to QbD framework for two main processes of manufacturing multiparticulates. In chapter 2, the research hypothesis is proposed and a series of research

objectives are outlined according to the research gaps. The experimental methods employed in this thesis are described in detail in chapter 3. The experimental results and discussion are given in chapter 4 according to the sequence of the research objectives. In the last chapter, the conclusions on the studies are given together with the future directions.

1.A. Overview of multiparticulate dosage forms

Multiparticulates are defined as medicinal particles that are small in size (usually 0.5-2.0 mm) and narrow in size distribution (Tang *et al.*, 2005). Multiparticulates are usually filled into capsules or compressed into tablets for the convenience of medicine administration (Bodmeier, 1997).

Two designs of multiparticulates can be classified depending on the structure. The first design includes a matrix core containing drug; the second design consists of a core and coat layer(s). For coated multiparticulates, the core can either be a matrix containing drug or it can be inert. When the inert core is used, an active coating layer containing drug and polymer can be applied. Polymers of different solubility and/or molecular weight may be used to tailor the drug release profile (Rowe, 1986; Chang and Robinson, 1990). Diffusion and erosion are the major drug release mechanisms for water insoluble and soluble polymers, respectively (Chang and Robinson, 1990). By using a combination of different types of cores, coat polymers and even multiple coat layers, a number of drug release profiles, e.g. sustained release, delayed release, immediate followed by sustained release, may be obtained (Tang *et al.*, 2005).

Multiparticulate systems for the purpose of controlled release have several advantages over non-disintegrating tablet dosage forms. Firstly, being small in size, multiparticulates can pass through the constricted pyloric sphincter easily and distribute themselves evenly within the gastrointestinal tract. The gastrointestinal transit time for non-disintegrating tablets may be erratic under the influence of the food digestion process within the gastrointestinal tract (Bechgaard and Ladefoged, 1978). Secondly, non-disintegrating tablets can stick to the mucosa of the gastrointestinal tract, releasing drug to a small area of mucosa and causing mucosal damage of the gastrointestinal tract. Comparatively, multiparticulates can minimize irritation to the gastrointestinal tract by their uniform distribution within the gastrointestinal tract (Porter, 2007). Lastly, for coated solid dosage forms, the drug release profiles of coated tablets for modified release purposes are greatly affected by imperfect film coating and poor coat uniformity as the drug can be released rapidly to a dangerous level due to coat defects. Multiparticulates comprise a large number of particles that are administrated together, thus reducing the risk of dose dumping due to coat defects compared to a single coated tablet (Hogan, 1995). This is a reason why multiparticulates are very often coated.

Multiparticulates can be in the form of mini-tablets, drug crystals, granules, or pellets (Hogan, 1995). Pellets, spherical shaped particles, are usually preferred due to the following reasons. Firstly, pellets have minimum surface-to-volume ratio, thus, minimal coating material is needed to achieve the desired coat thickness compared to irregular shaped particles (Hall and Pondell, 1980). Use of pellets as cores for coating offers an economical advantage. Secondly,

given the narrow particle size distribution, the drug release profiles of pellets are also more predictable (Lehmann, 1994). Thirdly, pellets have superior flowability, thus offering advantages in material handling, transfer and capsule filling (Tang *et al.*, 2005).

1.B. Manufacture of multiparticulate dosage forms

Due to the distinct properties of multiparticulates compared to conventional tablets, especially the excellent physical properties of pellets, and the potential advantages of coated pellets as controlled release dosage forms, pelletization and pellet coating processes are very frequently used in the pharmaceutical industry to produce controlled release multiparticulate dosage forms.

1.B.1. Pelletization

Pelletization is a process in which smaller particles are agglomerated into larger, free-flowing and spherical particles (Ghebre-Sellassie and Knoch, 2007). Extrusion-spheronization, rotary processing, high shear pelletization and hot melt extrusion are examples of pelletization methods. Due to the inclusion of the extrusion step, extrusion-spheronization and hot melt extrusion-spheronization are usually able to produce pellets that are more uniform in size, which is a desirable property for controlled release multiparticulate drug delivery systems. For the pharmaceutical industry, while hot melt extrusion is a relatively new process, extrusion-spheronization process has been used extensively for over 40 years and is currently the most popular pelletization method.

1.B.1.1. Extrusion-spheronization

Extrusion-spheronization process is a multi-step pelletization process patented by Nakahara (Nakahara, 1966). The main steps of extrusion-spheronization include dry powder blending, wet granulation, extrusion and spheronization (Erkoboni, 2003). The dry powder is blended to ensure a homogenous powder mixture. The wet granulation step can either be conducted using a planetary mixer or a high shear mixer. In the case where a high shear mixer is used, both dry powder blending and wet granulation can be conducted in the same processor. The amount of granulating fluid required for extrusion-spheronization is typically higher than that used for wet granulation for tabletting purpose (Erkoboni, 2003).

After wet granulation, the wet masses are forced through an orifice or die under controlled conditions for the purpose of forming the wet masses into noodle-like extrudates, which have uniform shape and density (Newton, 2007). There are mainly four types of extruders used in the pharmaceutical industry, namely screen extruder, rotary-cylinder extruder, rotary-gear extruder and ram extruder (Figure 2). Screen extruders can be further classified according to the die shape. An end plate die or dome shape die is usually used together with a single screw or a twin-screw (Figures 2A and 2B). The rotating screw(s) convey the wet mass to the die and force the wet mass to pass through the die to form extrudates. However, under high pressure conditions caused by the rotating screw, excessive heat production and a rise in extrudate temperature may occur due to frictional forces during the extrusion process. A twin-screw and a radial screen die were reported to be able to maintain a constant temperature during the extrusion process (Figures 2B and 2C). Another type

of extruder using a radial screen die is the Nica^{TM} extrusion system (Figure 2D). The system includes two sets of counter-rotating baffles. The inner baffle set presses the wet mass into the outer region within the radial screen die while the outer baffle set forces the wet mass through the radial screen. This unique extrusion mechanism was claimed to possess a minimum working distance during extrusion, thus ensuring uniform moisture distribution and lower temperature rise during the extrusion process (Newton, 2007).

The rotary-cylinder extruder includes two counter-rotating cylinders, a die cylinder and a pressure cylinder. The die cylinder is a cylinder perforated with uniform holes while the surface of the pressure cylinder is smooth (Figure 2E). Upon feeding the wet mass, the counter-rotating motion of the cylinders exerts pressure on the wet mass, forcing the wet mass through the die cylinder and to form extrudates. Good densification and mechanical strength are the main advantages of the rotary-cylinder extruder. The rotary-gear extruder consists of two counter-rotating gears (Figure 2F). The wet mass is drawn into the gap between the toothed cylinders from the hopper and then compacted while passing the toothed gears. The rotary-gear extruder usually produces denser extrudates due to compaction of the wet mass upon passing through the toothed cylinders.

In terms of feeding mechanism, extruders can be classified as screw feeding and gravity feeding. Screw feeding extruders include single screw and twin-screw extruders. The Nica^{TM} extruder, rotary-cylinder and rotary-gear extruders belong to the gravity feeding extruder category.

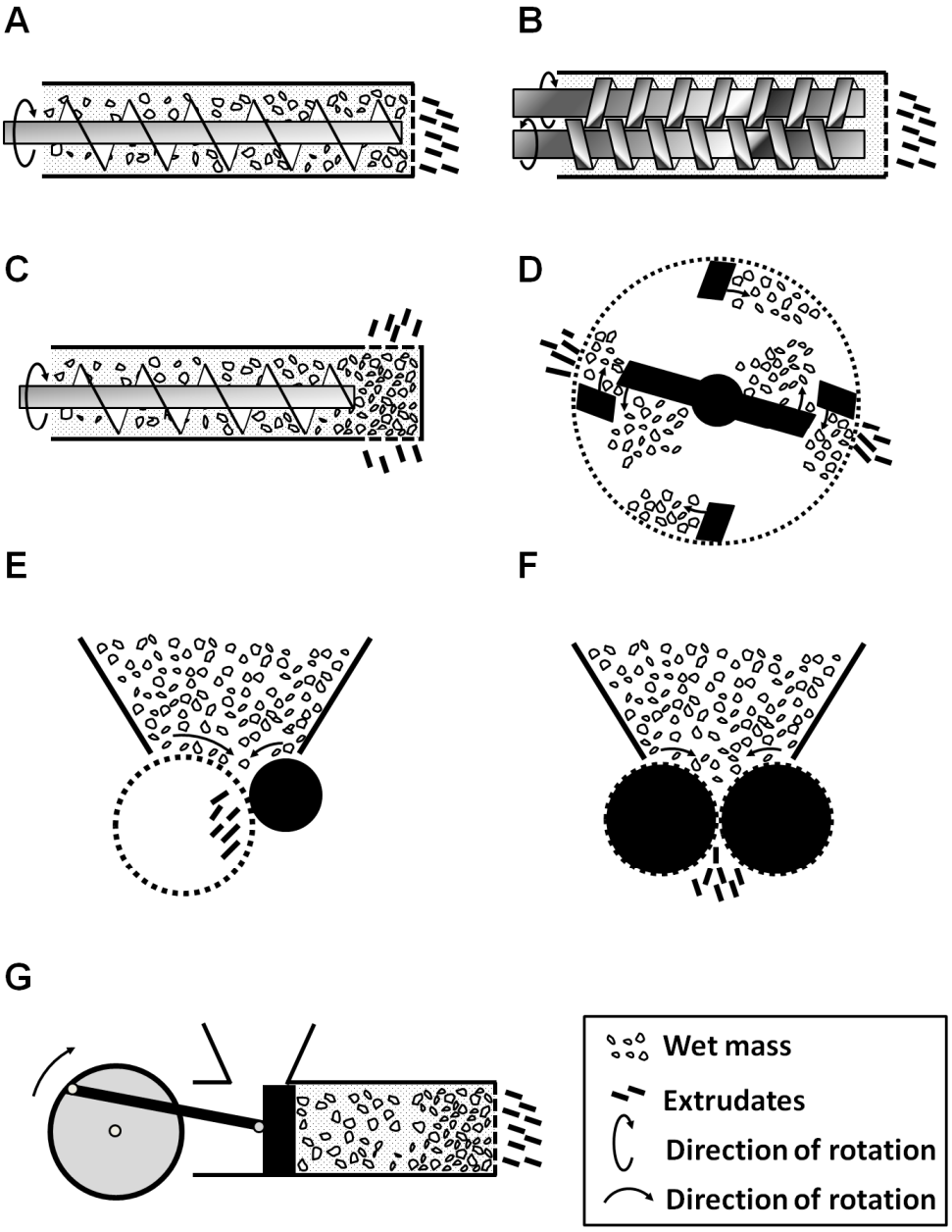

Figure 2. Schematic diagram of (A) single screw axial extruder, (B) counter rotating twin-screw extruder, (C) single screw radial extruder, (D) Nica^{TM} extruder, (E) rotary-cylinder extruder, (F) rotary-gear extruder and (G) ram extruder

For gravity feeding extruders, pressure is not applied on the wet mass before extrusion takes place. However, pressure develops along the rotating screw before extrusion. Hence, denser extrudates can be expected from screw feeding extruders. Due to its inability to work continuously, the ram extruder is mostly used for research and analysis rather than for production (Figure 2G).

Spheronization is the following step after extrusion of wet masses. The extrudates are rounded into pellets in a spheronizer, which has a relatively simpler design compared to the extruder. The spheronizer is composed of a fixed sidewall and a rotating frictional base plate, which maintains the material being spheronized in a tumbling-rope like motion (Reynolds, 1970). The plate surface is usually grooved to promote particle-particle and particle-plate interactions, thus rounding extrudates into pellets. Two types of plate geometric patterns are available, namely cross-hatched pattern and radial pattern (Figure 3). Both types of plates were reported to produce acceptable products (Rowe, 1985).

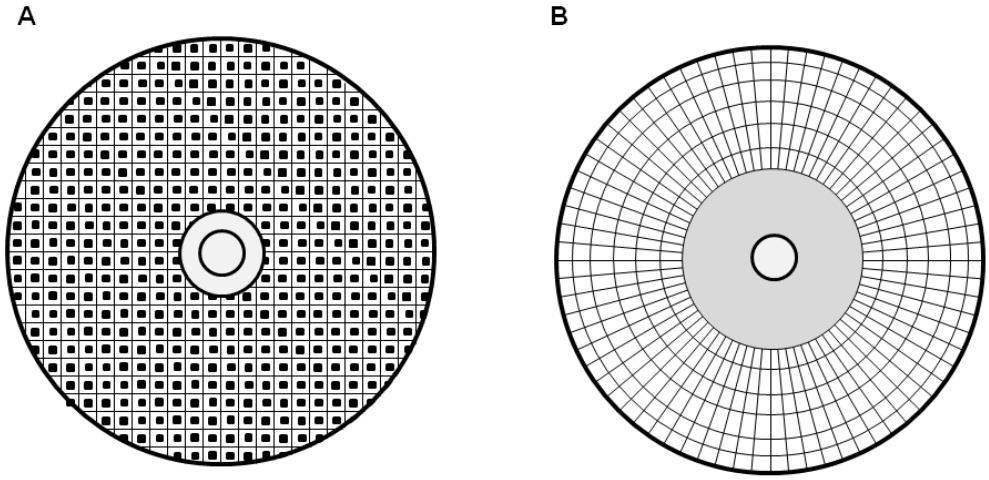

Figure 3. Schematic diagrams of frictional base plates with (A) cross-hatched and (B) radial geometric patterns1.B.1.2. Rotary processing

A rotary processor is mainly composed of a movable inner chamber, an outer chamber, a rotating frictional plate and an air distribution plate (Figure 4A). One or more tangential spray guns are installed near the bottom of the inner chamber. In the pelletization phase, the inner chamber is lowered to confine in-process materials within the inner chamber (Figure 4A). The rotating frictional plate maintains a tumbling rope-like within the inner chamber. The atomized granulation fluid causes particle growth within the inner chamber and the particles are rounded by the tumbling rope-like motion. Nucleation and layering are the major growth mechanisms for pelletization in rotary processing. The inner chamber can be lifted up to enable formed pellets to follow onto the air distribution plate near the outer chamber under centrifugal force. Hot air can pass through the air distribution plate during the drying and coating modes (Figure 4B). This feature allows pelletization, drying and coating to be completed in the same rotary processor. Hence, single-pot processing is a major advantage of rotary processing. However, pellet size distribution may be wider compared to the products from extrusion-spheronization, which uses extrusion as an effective means to control pellet size distribution.

1.B.1.3. High shear pelletization

Compared to the mixer blades used in high shear granulators for preparing granules to be used in tabletting, the shape of mixer blades for pelletization are modified to promote a larger sweep volume as well as a tumbling rope-like material flow pattern within the bowl during processing (Figure 4C).

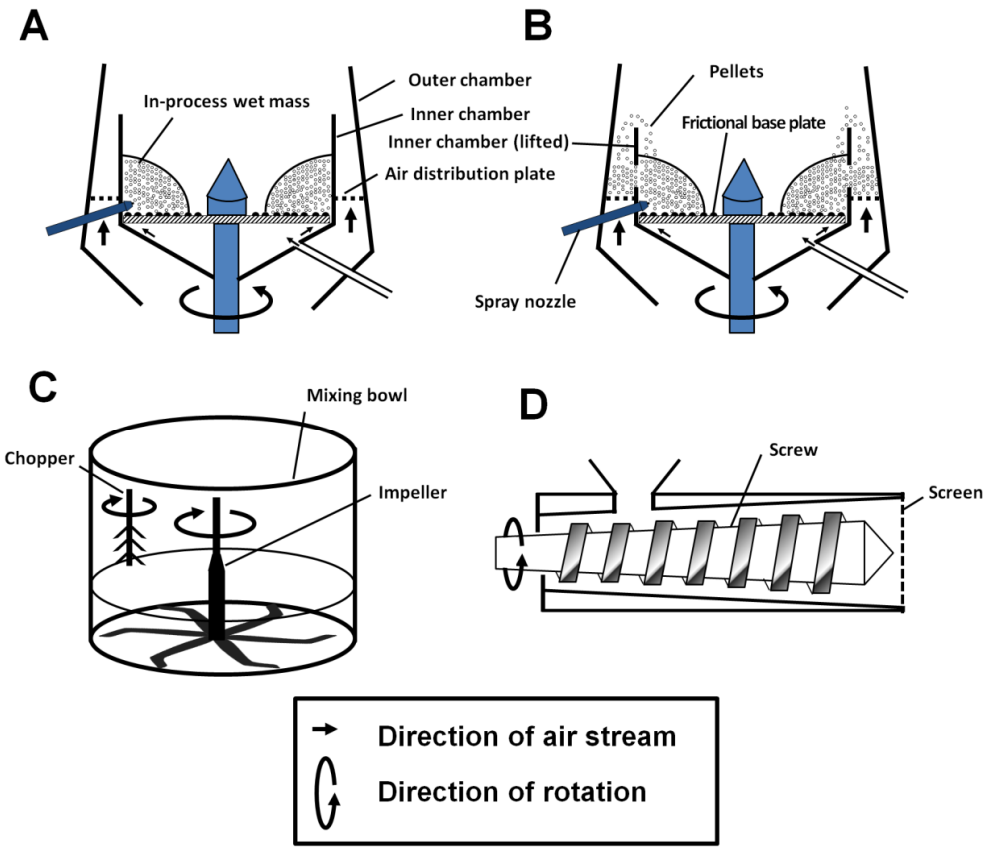

Figure 4. (A) Rotary processor in the pelletization mode, (B) rotary processor in drying/coating mode, (C) high shear pelletizer and (D) hot melt extruder

Two types of high shear pelletization processes can be classified depending on the formulation. The first category, melt pelletization, uses a thermoplastic polymer, which melts and serves as a binder under heat induction from the heat jacket or from the friction induced by the fast rotating mixer blade. Granulation and rounding occur after the melting of the thermoplastic polymer or wax. Melt pelletization is a single-step process for producing pellets. Another advantage of melt pelletization is that no granulation fluid is needed, thus avoiding possible hydrolysis of certain drugs when aqueous granulating fluid is used. The second category uses a formulation similar to that used for

extrusion-spheronization: drug, filler and spheronization aids, i.e. microcrystalline cellulose. With the addition of a granulating fluid and the tumbling rope-like motion within the mixer bowl, pellets can be formed in a single step.

1.B.1.4. Hot melt extrusion

The design of the hot melt extruder is different from the extruders for extrusion-spheronization. Firstly, the zones in the hot melt extruder can be divided into the conveying zone, melting zone and metering zone depending on the design of the screw (Figure 4D). This design was adapted from the polymer industry, where hot melt extrusion is widely used (Cheremisinoff, 1993). In the conveying zone, the screw design is similar to the single screw extruder. The main purpose of the screw in this zone is to convey solids from the hopper to the melting zone. Condensation and compression may occur in this stage. In the melting zone, the screw is designed to exert extensive shearing and mixing on the solids, causing a rise in solids temperature. The heating jacket is also used to transfer heat to the solids in the melting zone and metering zone. In the metering zone, melted solids are forced through the die to form extrudates. Depending on the die shape, rod shape extrudates, granules or films can be obtained. The rod-like extrudates can then either be cooled and cut into shorter extrudates or rounded into pellets using a spheronizer. A continuous spheronizer for hot melt extrusion-spheronization purpose has been patented recently (Ghebre-Sellassie *et al.*, 2007).

Functional excipients used for hot melt extrusion may be classified into matrix carriers, release modifying agents, bulking agents and lubricants.

Thermoplastic polymers or wax can be used as matrix carriers, which melt during hot melt extrusion but are able to bond the other powder ingredients together to form a matrix when cooled down. Hydrophobic, hydrophilic, slow hydrating or gelling matrix carriers have been used in hot melt extrusion processes (McGinity and Zhang, 2003). Hot melt extrusion offers a relatively simple and aqueous-free process for producing controlled release pellets. However, hot melt extrusion is still relatively new and is not suitable for processing heat-sensitive drug.

1.B.2. Coating of pellets

Fluid bed coating rather than pan coating is often used for coating pellets. This is because pellets tend to agglomerate due to their small size and fluid bed systems are preferred due to their higher drying capacities (Jones, 1994). On the other hand, fluid bed coating is less frequently used for tablet coating due to high agitation, which tends to damage the edges of tablets. Fluid bed coaters can be classified into four types, namely top spray fluid bed coaters, bottom spray fluid bed coaters, tangential spray fluid bed coaters and the Huttlin^{TM} fluid bed coaters (Figure 5). Bottom spray fluid coaters have been used more extensively in the pharmaceutical industry for coating of multiparticulates.

1.B.2.1. Top spray fluid bed coating

The top spray fluid bed coater is a direct modification of the fluid bed dryer with an additional spray nozzle above the particle bed surface (Figure 5A). The spray gun faces downwards and a two-fluid nozzle is usually used to atomize the coating fluid. The top spray fluid bed coater is similar to the top spray fluid bed granulator.

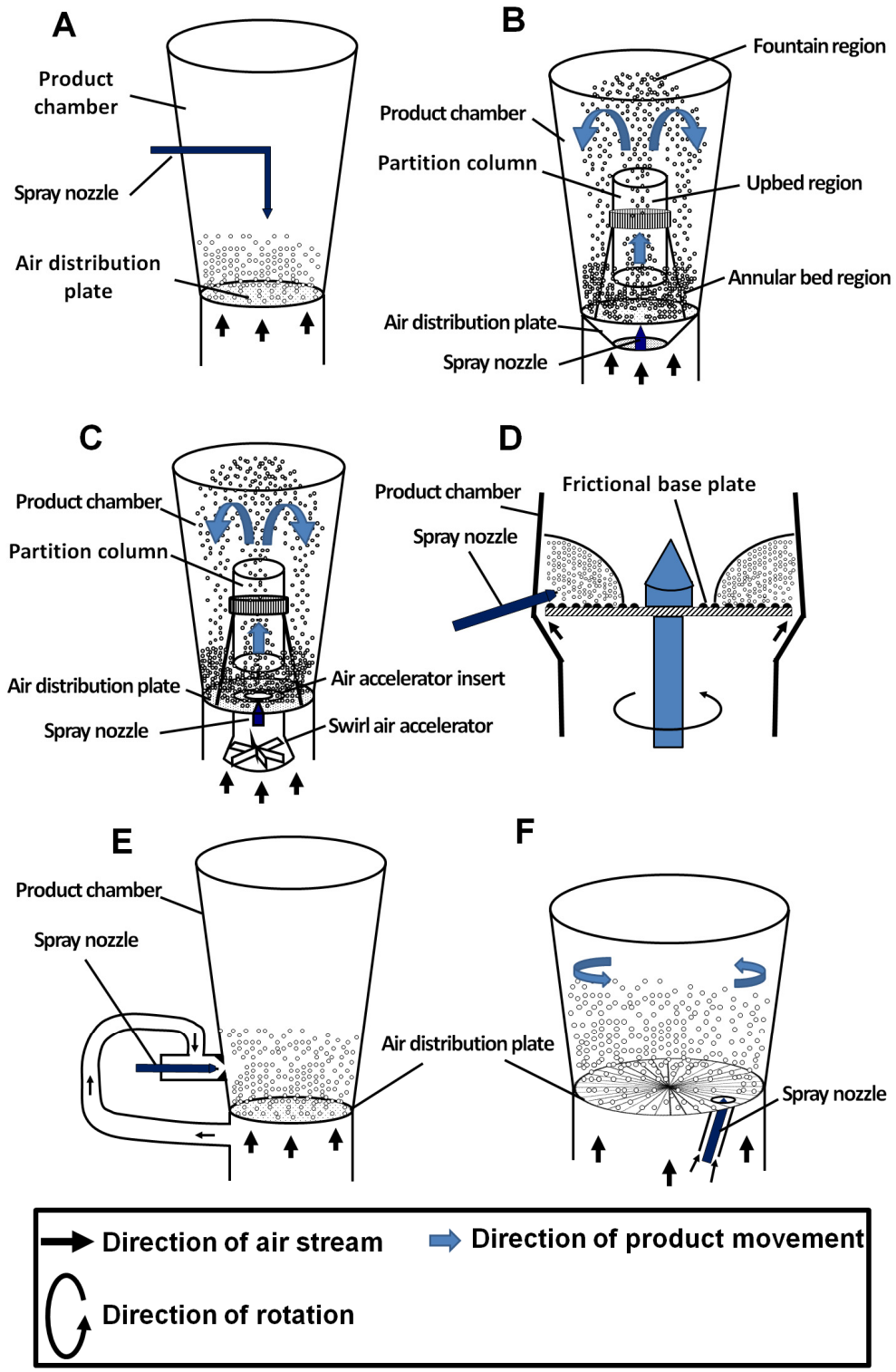

Figure 5. Schematic diagram of (A) top spray, (B) bottom spray (Wurster), (C) Precision, (D) tangential, (E) FlexStream™ and (F) Huttlin™ fluid bed coaters

However, the atomized coating fluid droplet size is usually smaller than that needed for granulation. Consequently, higher atomizing air pressures and lower coating fluid delivery rates may be required for coating. In most cases, a tapered shaped product chamber is used, which generally promotes an upward moving centre and downward moving annular flow pattern (Schaafsma *et al.*, 2006). However, the order of particle motion is largely disturbed by bubble induced particle motion. In the top spray fluid bed coating process, there are no distinct coating and drying zones. Hence, the top spray fluid bed coating process is not very effective in coating small particles due to the tendency for agglomeration and intense attrition.

1.B.2.2. Bottom spray fluid bed coating

The bottom spray fluid bed coater, Wurster coater, is a later modification of the fluid bed dryer (Wurster and Lincllof, 1966). Three major modifications were made (Figure 5B). Firstly, one or more partition column(s) was/were inserted in the middle of the coater, separating the coating zone(s), drying zone and staging area. The fountain-like particle motion ensures that particles pass through the spray zone more orderly than in the top spray fluid bed coater. Secondly, the air distribution plate is designed in such a way that the perforated area directly underneath the partition column is much larger than the other areas of the plate. This design ensures a high velocity, upward moving air stream within the partition column with a much lower air velocity outside the partition column. Thirdly, the spray nozzle is located under the bottom of the partition column. These modifications enable the atomized droplets to have greater chances for depositing on the pellet surfaces compared to the top spray fluid bed coater. This is because in the top spray fluid bed

coater, the atomized coating fluid droplets move against the fluidizing air, causing some of the fine droplets to be taken away by the air stream before they could be deposited on the pellet surfaces. During bottom spray fluid bed coating, the pellets flow into the partition gap, i.e. the gap between partition column and air distribution plate, under gravitational force and fluidization effect. Ideally, pellets at the bottom of the partition column are conveyed upward by the upward moving, high velocity hot air stream, which contains atomized coating fluid droplets. The droplets within the air stream deposit on the pellet surfaces, coalesce, dry and form a continuous film as the pellets travel upwards within the partition column. The upward moving pellets then decelerate and move downwards towards the annular bed surface after passing out of the partition column. This is attributed to the expansion of the air stream(s) into the product chamber, causing air velocity to fall below the terminal velocity of the pellets. Pellets await the next coating cycle after falling back into the annular bed.

The Precision coater is a modified version of the Wurster coater (Walter, 1998). Compared to the typical Wurster coater, three major modifications have been made (Figure 5C). Firstly, an upside down funnel shape of swirl air accelerator is added under the air distribution plate. As air is a highly compressible fluid, the air stream swirls upon passing through the funnel shaped swirl accelerator. A swirling fin located at the bottom of the swirl air accelerator is able to intensify the swirling air stream flowing into the partition column. Secondly, an air accelerator insert (AAI) is added between the air distribution plate and the swirl air accelerator. AAIs of different diameters can

be selected to tune the divergence of the air stream. AAIs with smaller orifice diameters generate more focused air streams of higher air velocities within the partition column. AAIs with larger orifice diameters produce more diverging air streams with lower air velocities. Moreover, due to energy conservation, when the air stream is passing through the narrow orifice of the AAI, Venturi effect occurs and pressure drops near the AAI orifice, drawing pellets into the partition column through the partition gap (Chan *et al.*, 2006). Venturi effect is considered a major feeding mechanism for the Precision coating process (Chan *et al.*, 2006). Thirdly, the spray nozzle is located within the AAI, underneath the air distribution plate, thus avoiding direct contact between pellets and un-atomized coating fluid. This is another advantage of the Precision coater compared to the typical Wurster coater with respect to prevention of agglomeration. Due to the modifications mentioned above, the Precision coater was found to have higher drying efficiency and was able to coat pellets with better coat uniformity and less agglomeration (Heng *et al.*, 2006).

1.B.2.3. Tangential spray fluid bed coating

The tangential spray fluid bed coater is another modification of the fluid bed dryer. The bottom plate is able to rotate to maintain a tumbling rope-like motion of pellets while the motionless outer rim is perforated to allow fluidizing air to pass through (Figure 5D). The direction of the spray nozzle is usually located in the sidewall and the spray path is positioned in a tangential direction to the rotating bottom plate. More than one spray nozzles may be used depending on the scale of the equipment. In the tangential spray fluid bed coating process, droplets of atomized coating fluid deposit on the pellets near

the spray nozzle. The hot air passes through the perforated and motionless outer rim and dries the deposited droplets. The rotating plate maintains the tumbling rope-like motion of pellets, ensuring that pellets pass through the spray zone repetitively. The FlexStream™ system is a modified tangential spray fluid bed coater/granulator (Figure 5E). The major modification includes supplying low pressure air flow in the spray nozzle area to create a particle free zone. This modification avoids direct contact between pellets and un-atomized coating fluid.

1.B.2.4. Huttlin™ fluid bed coating

The Huttlin™ fluid bed coater is classified separately due to the unique design of its air distribution plate as well as three-fluid spray nozzle (Figure 5F). Unlike the rotating plate of the tangential spray fluid bed coater, the Huttlin™ coater has a fixed air distribution plate. Radically distributed air distribution slots were drilled on the air distribution plate. The slots are drilled at 45° against the air distribution plate plane, thus targeting air stream at 45° against the air distribution plate plane as well. The angled air jets fluidize and drive pellets to rotate on the air distribution plate and pass through the spray nozzle repetitively. The three-fluid nozzle is another major modification of the Huttlin™ coater. In the design of a three-fluid nozzle, the typical two-fluid nozzle is jacketed in a third air supplying tube. The jacket air stream confines atomized droplets into a bulb-like zone. The jacket air stream also avoids direct contact between pellets and the un-atomized coating fluid to avoid agglomeration. This design shares similar principles with the Precision coater and FlexStream™ system as spray nozzles are enveloped by fast moving air streams, preventing undeveloped droplets from contacting pellets.

1.C. Quality frameworks for solid dosage form manufacture

According to the FDA, pharmaceutical product quality is defined as the suitability of a drug product for its intent of use (FDA, 2006). A high quality product is further defined as a product free from contamination and which reproducibly delivers therapeutic benefits as claimed in the product label (Woodcock, 2004). QbT is the current quality framework employed in solid dosage form manufacture. Under the QbT framework, drug product quality is ensured by raw material testing, in-process sample testing and end product quality testing (Yu, 2008). QbD, the impending quality system, emphasizes good understanding of manufacturing processes, continuous improvement and builds quality into the product.

1.C.1. Quality by test

Under the QbT framework, the raw materials including drug substance and excipients are subject to the requirements of the regulatory agency (Yu, 2008). Raw materials can be used for manufacturing drug products if their attributes meet the requirements. However, lacking fundamental understanding of the manufacturing processes, the manufacturing process parameters have to be tightly controlled to ensure consistency in the final product quality. In the case of changes in the manufacturing process parameters, the manufacturer needs to file supplementary documents with the regulatory agency. Finished drug products are also subjected to tests to determine whether the products meet the requirements of the regulatory agency.

The products are discarded if the tested samples cannot meet specifications. Without a fundamental understanding of the source causing batch failure, the

manufacturer continues to suffer from risks of batch failures and product losses. Unfortunately, a good understanding of the process source causing batch failure is not encouraged under the QbT framework. Moreover, the rigorous specifications in the QbT system are also responsible for frequent product recalls as well as drug product shortage (Nasr, 2006).

1.C.2. Quality by design

QbD is a systematic, scientific, risk-based, holistic and proactive approach to pharmaceutical development that begins with predefined objectives and emphasizes understanding and control of product and process (FDA, 2006; Nasr, 2006). Under the QbD framework, the critical quality attributes of drug products are identified from the perspective of therapeutic benefits for the patient. The critical quality attributes are then translated into critical process parameters. Hence, taking possible raw material quality variations into consideration, the acceptance ranges of drug product critical quality attributes can then be translated into ranges of operational process parameters, which construct the process design space. Thus, the process design space is a hyperspace resulting from multi-dimensional and interacting process parameters that have been proven to demonstrate quality assurance. Upon approval of the process design space by the regulatory agency, process parameter changes within the design space no longer need to be filed, thus giving more flexibility to the manufacturing process.

The critical quality attributes of drug products need to be determined based on the therapeutic purpose as well as the physicochemical characteristics of each drug product. For instance, according to Nasr, under the QbD framework, the

dissolution profile of a biopharmaceutical class III (high solubility low permeability) drug product need not be as stringent as required under current specifications (Nasr, 2006). This is because from the therapeutic perspective, dissolution is not likely to be the limiting step for biopharmaceutical class III drug products. However, current specifications are the same for all tablet products without considering biopharmaceutical properties of the drugs.

Currently, design of experiments (DoE) is considered a valuable tool for mapping the relationship between formulation and process variables and critical quality attributes. Combining predictive statistical models, e.g. partial least squares, the process parameters can be adjusted to compensate for the raw material quality variations to yield drug products with the desired quality attributes. However, there are two main limitations to this approach. Firstly, thorough experiments are only applicable to small scale batches, and the relationship may not hold after process scale-up. Secondly, despite high goodness of the fitting, this approach may suffer from low capability of prediction. This is because DoE takes a purely statistical approach in modelling the relationships and lacks physical implication in the model.

1.D. Process analytical technologies

The application of process analytical technologies (PAT) is considered as an advanced method under the QbD framework (CDER, 2004; FDA, 2006). PAT tools mainly include process analyzers and process control tools. The process variability sources are monitored by process analyzers and fed to the input of process control tools. Based on the process control model and the control input from process analyzers, the process parameters are tuned in a real-time manner.

It was further pointed out that despite various similarities shared between the chemical engineering and pharmaceutical industries, the pharmaceutical industry is largely lagging behind in terms of process understanding and self-tuning process control (Basu, 2009). Hence, the ultimate goal of PAT should be to promote self-tuning process control systems, which have been widely used in chemical engineering for many years. Unfortunately, although important, the issue of process control is seldom addressed since introduction of the PAT concept. This is mainly because a good understanding of the process at the mathematical level is the basis for developing a self-tuning process controller and relatively few research studies have been carried out to model pharmaceutical processes.

1.D.1. General control theory

According to the control theory, the first step is to develop a mathematical model of the process, which incorporates the relationship between process parameters and product quality attributes. The desired input function/process parameters can be solved by analyzing process models (Chen, 1999) (Figure 6).

However, there is a lack of accurate pharmaceutical process models that are purely based on physical descriptions. This is mainly because most pharmaceutical manufacturing operations involve complex physical processes, i.e. fluidization, multiphase flow and granular systems, which are difficult to be modelled with good accuracy and high predictability. Empirical models can be developed and used for small scale and continuous processes; however it is

not practical to scrutinize each process condition and build empirical models for large scale processes.

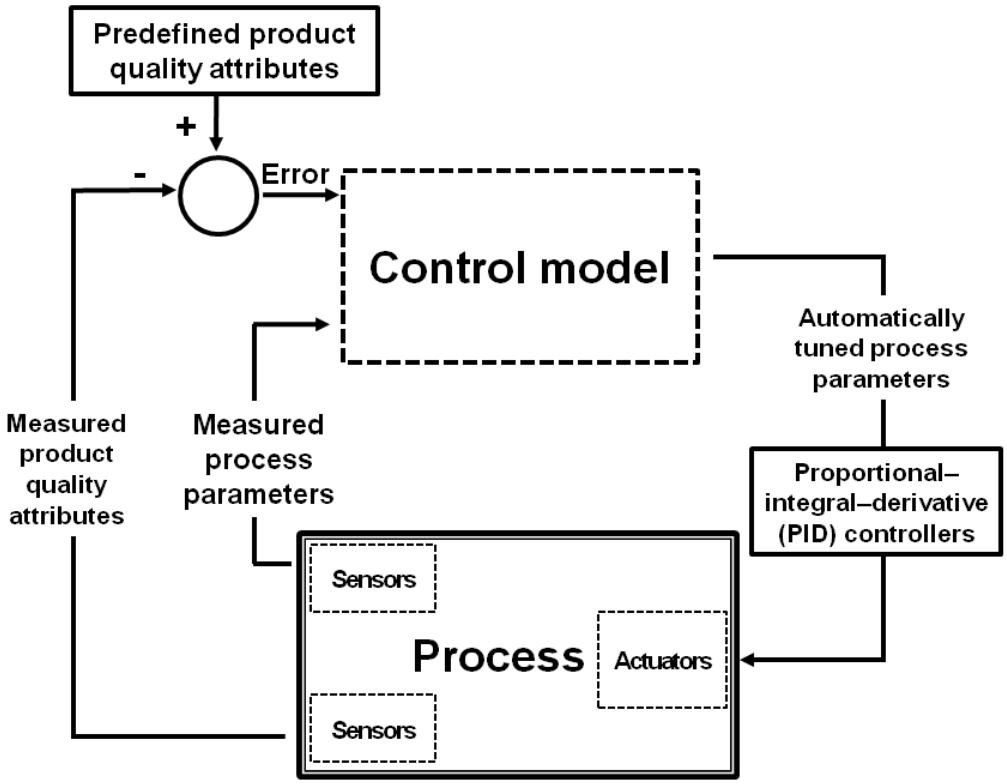

Figure 6. Schematic diagram for ideal process control

Practically, the control system includes feedback and feedforward control (Figure 7) (Koenig, 2009). Feedback control takes corrective actions only if there is an error between expected values and measured values. Feedforward control reacts on the anticipated changes. Again, implication of accurate corrective actions relies on sophisticated process control models, which are largely lacking in pharmaceutical processes.

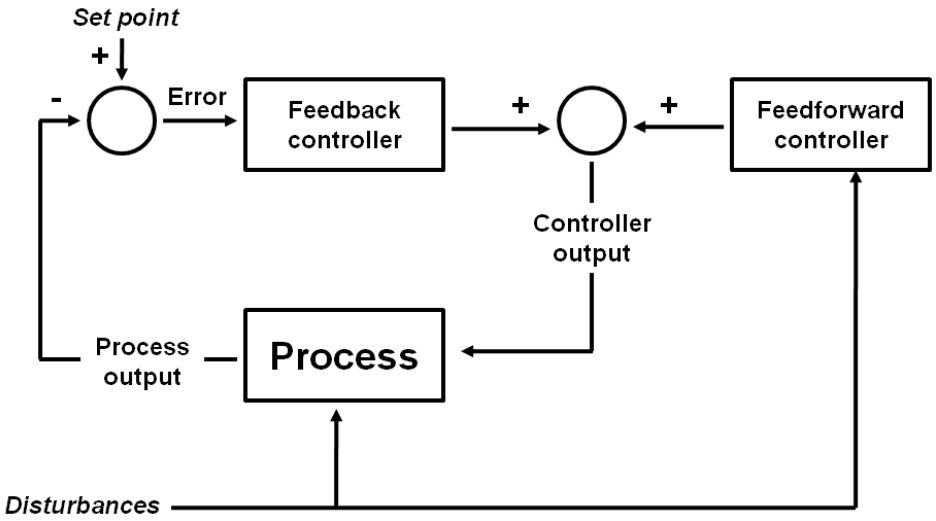

Figure 7. Combination of feedback and feedforward controllers for practical pharmaceutical process control (adapted from Koenig, 2009)

1.D.2. Classification of process analyzers

Current process analyzers for pharmaceutical processing can be classified into two types: process analyzers for measuring the end product quality attributes and process analyzers for assessing the progress of the process. For the first type of process analyzers, end product quality attributes are obtained in real-time manner. For instance, focused beam reflectance measurement (FBRM) has been used to monitor the Ferret diameter of particles during fluid bed granulation (Hu *et al.*, 2008); Raman/ near infrared (NIR) spectrophotometers have been used to monitor the coat thickness during tablet coating (Kirsch and Drennen, 1996; Andersson *et al.*, 1999; Andersson *et al.*, 2000; Romero-Torres *et al.*, 2006). Feedback process analyzers alone may be adequate for controlling relatively simple processes. For example, NIR spectrophotometers have been used in detecting mixing homogeneity; once a certain mixing homogeneity is achieved, the process can be stopped. For more complicated processes with multiple process parameters, as feedback process analyzers monitor the end product quality attributes (outcome/downstream of the

process), the process is still a 'black-box' from a control perspective. Moreover, for pharmaceutical processes, the room for reprocessing is limited. For instance, it is not common to reprocess over-sized pellets or over-processed granules. Hence, the trial-and-error feedback control alone may not work well for pharmaceutical processes, most of which are batch based and non-reversible. Consequently, the understanding and control of pharmaceutical processes is limited by monitoring of endpoint control alone.

The second group of process analyzers either monitor physical parameters that are indicative of the progress of process or, more directly, monitor the variability sources, which cause major changes in critical quality attributes of the final product. For instance, the torque values of a high shear granulation process can be reflective of the progress of the process (Corvari *et al.*, 1992); power consumption is also used in high shear granulation/pelletization to monitor the formation of pellets (Ritala *et al.*, 1988; Heng *et al.*, 1999). Process analyzers focusing on the progress of the process can reveal more detailed information on the process itself, thus facilitating better process understanding and control.

Unfortunately, the focus of most research on current process analyzers is on monitoring the end product quality attributes. However, without sophisticated process models, the information of end product quality attributers cannot be effectively used for better process understanding and control. Hence, it is highly desirable to develop process analyzers that are reflective of the progress of the process.

1.D.3. Roles of in-process material flow pattern in pharmaceutical processes

In-process material flow pattern measurement is a promising approach to be developed as a process analyzer for assessing the progress of the process with the following reasons. Firstly, most pharmaceutical processes essentially maintain a certain flow pattern of drug substance and excipients by means of agitation, suspension or fluidization. Hence, in-process material flow pattern is a basic characteristic of pharmaceutical processes. Secondly, instead of developing models directly from mass, heat and momentum conservation, measured in-process material flow pattern indicates the extent of mass and momentum transfer, which is the basic phenomenon driving the progress of the process (Brennen, 2005). Thirdly, in-process material flow pattern is also influenced by drug product quality attributes, such as particle size and shape etc., hence reflecting the progress of the process.

Studies showing the importance of in-process material flow pattern are not rare. For instance, a tumbling rope-like motion was considered as critical for pellet formation in high shear pelletization and spheronization (Reynolds, 1970; Ramaker *et al.*, 1998). Certain granular flow patterns need to be maintained during silo discharge to prevent arch formation as well as segregation (Cooper, 2001). Particle recirculation within the partition column of the bottom spray fluid bed coater was considered as the major variability source of coat uniformity (Bi and Pugsley, 2007).

1.D.4. Visiometric process analyzer & its potential applications

For the purpose of quantifying in-process material flow pattern, a range of techniques, i.e. imaging, image processing and image analysis, are most frequently used in the study of fluid mechanics as well as granular flow. For the ease of reference in the study of pharmaceutical processes, the concept of a visiometric process analyzer is proposed. A visiometric process analyzer is defined as a process analyzer that uses imaging and image analysis to obtain process related information. A visiometric process analyzer quantifies in-process material flow pattern by capturing and analyzing sequential images of in-process material for flow pattern information.

For visiometric process analyzers, particle image velocimetry (PIV) is the major technique for flow pattern detection. PIV was originally developed for fluid mechanics studies, and laser illumination was used to capture particle motion on the plane of interest (Adrian and Yao, 1985; Adrian, 1988; Adrian, 1991; Keane and Adrian, 1992). In PIV, the images of particles of interest were taken using a double-exposure camera or a high speed camera. The laser illuminates the flow field from an orthogonal direction to the camera. The tracer particles on the illuminated plane scatter laser light and are captured by the camera (Raffel *et al.*, 2007). In the early days of using film cameras for PIV, optical Fourier transformation was used for PIV analysis. However, this method was reported as time-consuming and inaccurate (Westerweel, 1993). Westerweel laid the foundation for transforming PIV analysis from analogue to digital (Westerweel, 1993).

In digital PIV, the adjacent images are divided into sub-images; templates in the sub-images in the first frame are taken and roamed in the corresponding sub-images from the second frame. The similarity between the roaming templates and the corresponding image intensity of sub-images in the second frame are determined. The displacement that maximizes the similarity is then considered as the average displacement of the template (Figure 8). Given the recording speed of sequential images, the velocity of the template can be obtained. Cross-correlation and minimum quadratic differences (MQD) are the two major methods for quantifying image similarity (Suh, 2003). The MQD method is capable to of detecting velocity even when single particles cannot be differentiated, and hence, is more robust than the cross-correlation method (Suh, 2003). However, MQD is more computationally intensive than the cross-correlation method. With similar principles, PIV has been extended into the three-dimensional domain based on volumetric laser illumination, multiple cameras as well as more sophisticated state-space models (Raffel *et al.*, 2007; Elsinga *et al.*, 2008; Hill, 2008).

In recent years, PIV is also gaining increasing attention for applications in quantifying the velocity field of granular movement, e.g. granular movement in the silo discharger or in the high shear mixer (Conway *et al.*, 2005; Ostendorf and Schwedes, 2005; Nilpawar *et al.*, 2006; Darelius *et al.*, 2007; Slominski *et al.*, 2007). Therefore, the application of PIV in granular flow is also referred to as granular PIV. For granular PIV, laser illumination is no longer necessary as long as the images of granular flow can be captured clearly.

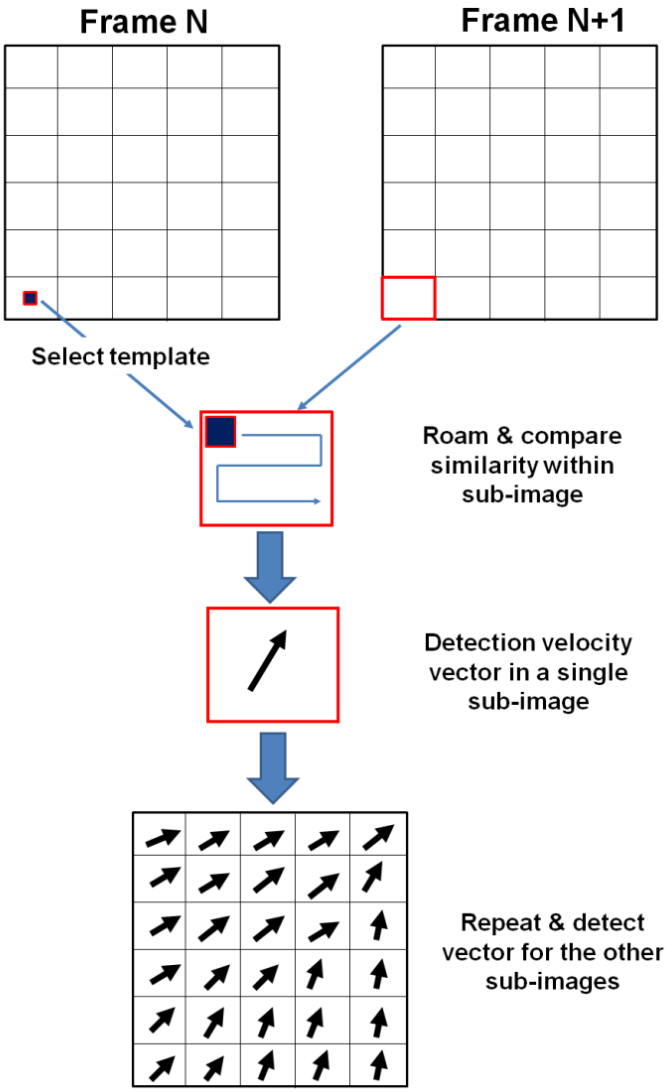

Figure 8. Schematic diagram showing the principles of PIV

Current studies using granular PIV include silo discharge processes, flow pattern in the freeboard region of the fluid bed, and the surface velocity of high shear mixers (Duursma *et al.*, 2001; Bokkers *et al.*, 2004; Conway *et al.*, 2005; Nilpawar *et al.*, 2006; Darelius *et al.*, 2007; Slominski *et al.*, 2007). Nevertheless, the studies carried out to date were not systematic in correlating in-process material flow pattern and product attributes, and the feasibility of utilizing in-process material flow pattern information, using granular PIV in particular, as a process analyzer for monitoring the progress of the process has

yet to be studied. The aim of this PhD project was to develop visiometric process analyzers to monitor in-process material flow pattern for a better understanding and control of pharmaceutical processes, e.g. extrusion-spheronization and bottom spray fluid bed coating in particular.

1.E. Research gaps in extrusion-spheronization

The extrusion-spheronization process has been studied extensively with respect to both the extrusion step and formulation aspects. The extrusion process has been thoroughly investigated, not only in the area of pharmaceutical technology but also in the area of plastic extrusion in the polymer industry. The mathematical models for different types of extruders have been well established (Cheremisinoff, 1993). For pharmaceutical extrusion, the wet mass has been characterized during a ram extrusion process and the performance of different types of extruders compared (Harrison *et al.*, 1985; Baert *et al.*, 1992; Baert *et al.*, 1993). The design of the extruder screen was also investigated (Hellen *et al.*, 1992; Vervaet *et al.*, 1994).

Similarly, the role of formulation factors in extrusion-spheronization is also quite clear. It was pointed out that the addition of a wetting agent (usually water or an aqueous-based fluid) is considered critical as the degree of liquid saturation determines the plasticity of the wet mass. The wet mass needs to possess sufficient plasticity to deform during the extrusion process and be rounded into smaller, uniform particles yet avoiding excessive agglomeration during spheronization (Liew, 1996). Moreover, unlike granulation for tabletting purposes, which is typically stopped at the advanced funicular state, wet masses in the capillary state are usually preferred for extrusion-

spheronization. Hence, over-granulation generally is not an issue in extrusion-spheronization (Erkoboni, 2003). The mixer torque rheometer and ram extruder have been extensively used for characterizing wet masses for extrusion purposes and it was pointed out that the maximum mean torque indicates the capillary state (Harrison *et al.*, 1985; Parker *et al.*, 1990; Rowe and Parker, 1994). Besides microcrystalline cellulose (MCC), sodium carboxymethylcellulose, povidone, alginate, hydroxypropyl methylcellulose (HPMC), starch, crospovidone and alginate have also been explored as alternative spheronization aids (Funck *et al.*, 1991; Liew *et al.*, 2005; Sriamornsak *et al.*, 2006; Sriamornsak *et al.*, 2007).

In comparison, the spheronization process has been less studied. The studies on spheronization so far mainly focused on the influences of process parameters, such as spheronization speed and process time, and on end product characteristics (Wan *et al.*, 1993). Nevertheless, with respect to the QbD framework and self-tuning process control, two important and closely related research questions are still not clear. Firstly, three different theories on the particle growth kinetics during spheronization process exist. An unambiguous knowledge of particle growth kinetics is the basis for the development of process models. Secondly, based on the particle growth kinetics to be investigated, it is desirable to develop a visiometric process analyzer that can be employed to monitor the progress of the process as well as to detect the endpoint.

1.E.1. Particle growth kinetics of spheronization process

In order to lay the basis for process model and process analyzers, the three current theories on particle growth kinetics need to be examined and verified.

The first two theories are based on the formation and breakage of dumb-bell shaped particles (Figures 9A and 9B). According to the theory proposed by Rowe, the ends of the extrudates were first rounded, followed by formation of dumb-bell shaped particles. The dumb-bell shaped particles were then transformed into ellipsoid shaped particles followed by the formation of spheres (Rowe, 1985) (Figure 9A). According to the theory proposed by Baert *et al*., the extrudates were first transformed into bent rope shape, forming twisted dumb-bell shaped particles. The next steps involved the breakage of a twisted dumb-bell particle into two spheres, each with a hollow cavity. In the final step, the spheres with cavities were rounded into spheroids (Baert and Remon, 1993) (Figure 9B). According to the remodelling theory developed by Liew *et al*., which is distinctively different from the previous two theories, extrudates were firstly broken down into fine particles and coarser particles (Liew *et al.*, 2007). The coarser particles grew by layering of the fine particles on their surfaces. Spheroids formed after rounding of the agglomerated particles (Figure 9C). This theory is referred to as the remodelling theory because particles are described to grow by means of breakage and recombination of the extrudate materials (Liew *et al.*, 2007).

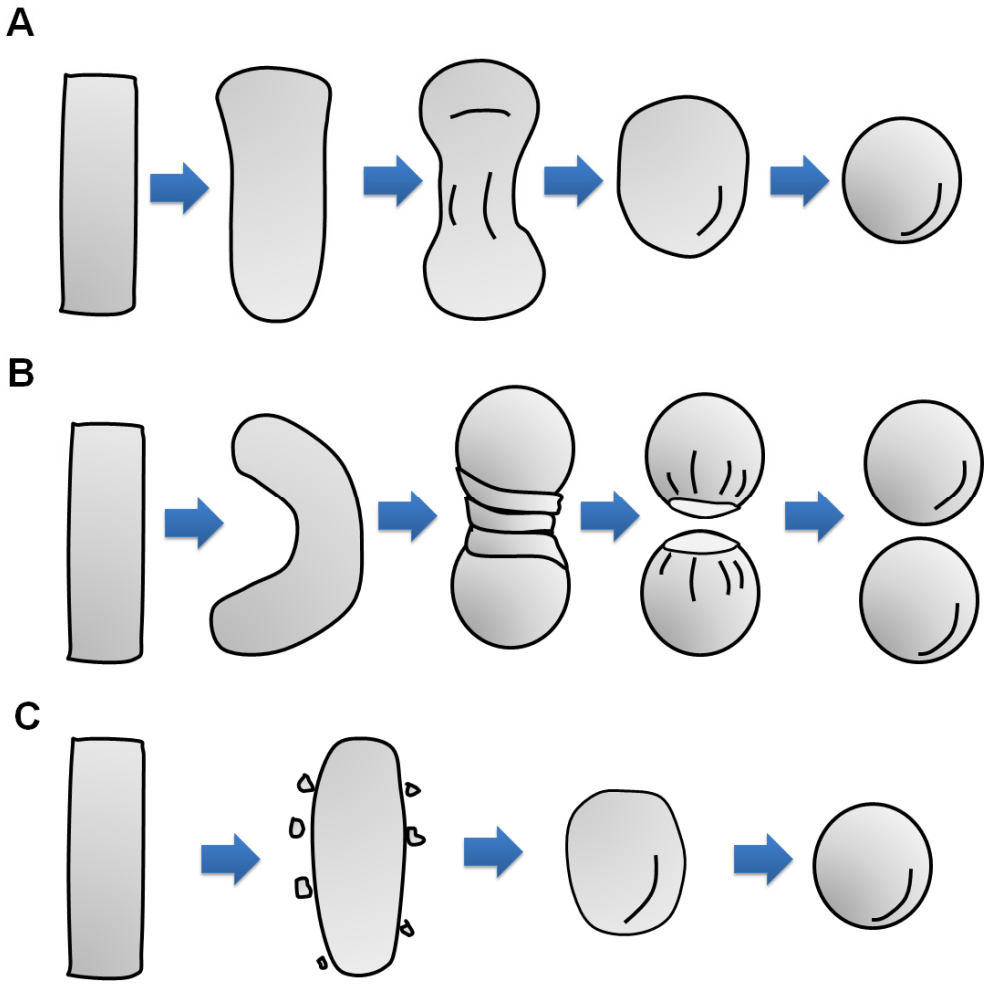

Figure 9. Particle growth kinetics for spheronization process proposed by (A) Rowe, (B) Baert *et al.* and (C) Liew *et al.*

Although the first two theories were proposed much earlier and hence, more widely accepted, they have also been criticized particularly with respect to material usage. In the study carried out by Rowe, MCC contents as high as 50% were used. However, in the pellet manufacturing process, much lower MCC contents are more commonly used, considering the usage of drug as well as filler in the formulation. As extrudates may differ in their viscoelastic properties between formulations with high MCC contents and formulations with low MCC contents, high MCC contents may not be representative of commonly used formulations for extrusion-spheronization (Harrison *et al.*,

1985). Hence, the representativeness of Rowe's growth kinetics model is questionable. As MCC has been depicted as a "molecular sponge" and has high capability to absorb water/granulating liquid, higher binder liquid concentrations may be required for higher MCC content (Harrison, 1984). Moreover, it has also been reported that higher binder concentration may result in lower drug dissolution rate (Baert and Remon, 1993). Hence, higher MCC content may result in a lower drug dissolution rate. In the study carried out by Baert *et al.,* plasticine was used instead of a typical pelletization formulation, and the samples in the different phases during spheronization were obtained by changing spheronization speed of plasticine extrudates but keeping spheronization time the same. Again, it is well known that plasticine is highly plastic and may not be representative of the viscoelastic behaviour of typical pelletization formulations. Moreover, the samples reflecting different stages in the spheronization process should be collected by means of in-process sampling at different time intervals rather than by merely taking the end products of runs carried out with different spheronization speeds. In the third theory, although a typical formulation and in-line sampling were employed to determine particle morphology, only a few combinations of granulating fluid contents and spheronization speeds were studied. It is known that the content of the granulating fluid may alter the plasticity of extrudates and spheronization speed determines the energy input rate in the spheronization process (Wan *et al.*, 1993). Both factors may affect the particle growth kinetics and the full picture of the particle growth kinetics may not be revealed without incorporating combinations with wide ranges of granulating fluid contents and spheronization speeds. Hence, it is desirable to study

particle growth kinetics with respect to relatively wide ranges of granulating fluid contents and spheronization speeds.

1.E.2. Relationship between particle motion in the near plate region and particle growth kinetics

Particle motion, especially in the region near the frictional base plate, is of great importance for the spheronization process. This is because according to the theory of fast sheared granular material, a thin layer of particles, which is referred to as fluidization layer, in the near frictional base plate region may be dominated by much faster motion than the bulk material and massive collisions between particles (Jenkins, 1998). Simulation studies also have shown that the near plate region is the most energy-concentrated region (Taberlet *et al.*, 2007; Wildman *et al.*, 2008). Hence, particle growth may be directly related to the motion in the near plate region and it is desirable to investigate the relationship between particle growth kinetics and particle motion in the near plate region.

1.E.3. Relationship between bed surface flow pattern and particle growth kinetics

In the early days of extrusion-spheronization studies, Reynolds qualitatively described the extrusion-spheronization process and pointed out that bed surface flow pattern was indicative of whether the water content of the extrudates were adequate (Reynolds, 1970). Although this point was widely accepted and cited, the relationships between the bed surface flow pattern and characteristics of extrudates and spheronization speed were not studied quantitatively and systematically (Erkoboni, 2003). Hence, with the aid of

high speed video imaging and granular PIV, it is of interest to track bed surface flow pattern during spheronization and investigate the relationship between bed surface flow pattern and particle growth kinetics with respect to material plasticity as well as spheronization speed.

1.F. Research gaps in bottom spray fluid bed coating

The bottom spray fluid bed coating process is extensively used in the pharmaceutical industry to coat multiparticulates due to the ability of the process to coat fine particles. Studies have been focused on the correlation between coating fluid viscosity and agglomeration, formulation development to prevent agglomeration, modelling of agglomeration, modification of coating apparatus and drying efficiency (Fukumori *et al.*, 1992; Lehmann, 1994; Heng *et al.*, 1996; Heng *et al.*, 2006; Tang *et al.*, 2008).

However, under the QbD framework, the variability sources affecting the critical quality attributes of end products need to be identified and controlled. Coat uniformity is considered as a critical quality attribute and hence the variability sources affecting coat uniformity need to be identified and controlled (Yu, 2008). Currently, particle cycle-time distribution is considered as a major source causing coat non-uniformity. Particle cycle-time refers to the time interval for a randomly chosen particle to consecutively pass through the spray zone twice. As coating is a repetitive process, a narrow particle cycle-time distribution results in uniform coat layer. Investigations have focused on measurement of particle-cycle time distribution using magnetic particle tracking and modelling and simulation of Wurster process based on particle

cycle-time distribution (Xu and Turton, 1997; Cheng and Turton, 2000a; Crites and Turton, 2005; KuShaari *et al.*, 2006).

Although it is clear that particle cycle-time distribution is a major variability source causing coat non-uniformity, few studies to date focused on the monitoring and control of cycle-time distribution. This is because particle movement within the bottom spray fluid bed coater is an ensemble result of particle movement in the upbed, fountain and annular bed regions, where the motions of particles are distinctively different with different influences on coat uniformity (Christensen and Bertelsen, 1997). The particle motions in the upbed, fountain and annular bed regions contribute differently to the particle cycle-time distribution (Crites and Turton, 2005). Hence, it is desirable to develop process analyzers that monitor particle movement in different regions of the bottom spray fluid bed coater. Moreover, it is interesting to investigate the mechanisms of particle motion causing broad particle cycle-time distribution in the different regions.

1.F.1. Particle recirculation within the partition column

Using positron emission particle tracking (PEPT) technique, it was found that particles within the partition column may join recirculation (Palmer *et al.*, 2006). Bi *et al.* discovered that a particle may re-cycle within the partition column up to 15 times before being conveyed through the outlet of the partition column (Bi and Pugsley, 2007). Particle recirculation in the upbed region is considered as the major variability source for two reasons. Firstly, the particles joining recirculation are usually not fully dried and re-entry into the spray zone may cause agglomeration. Secondly, the cycle-time of particles

joining and without joining recirculation can be dramatically different, thus causing a broad particle cycle-time distribution and non-uniform coat in the end products (Figure 10).

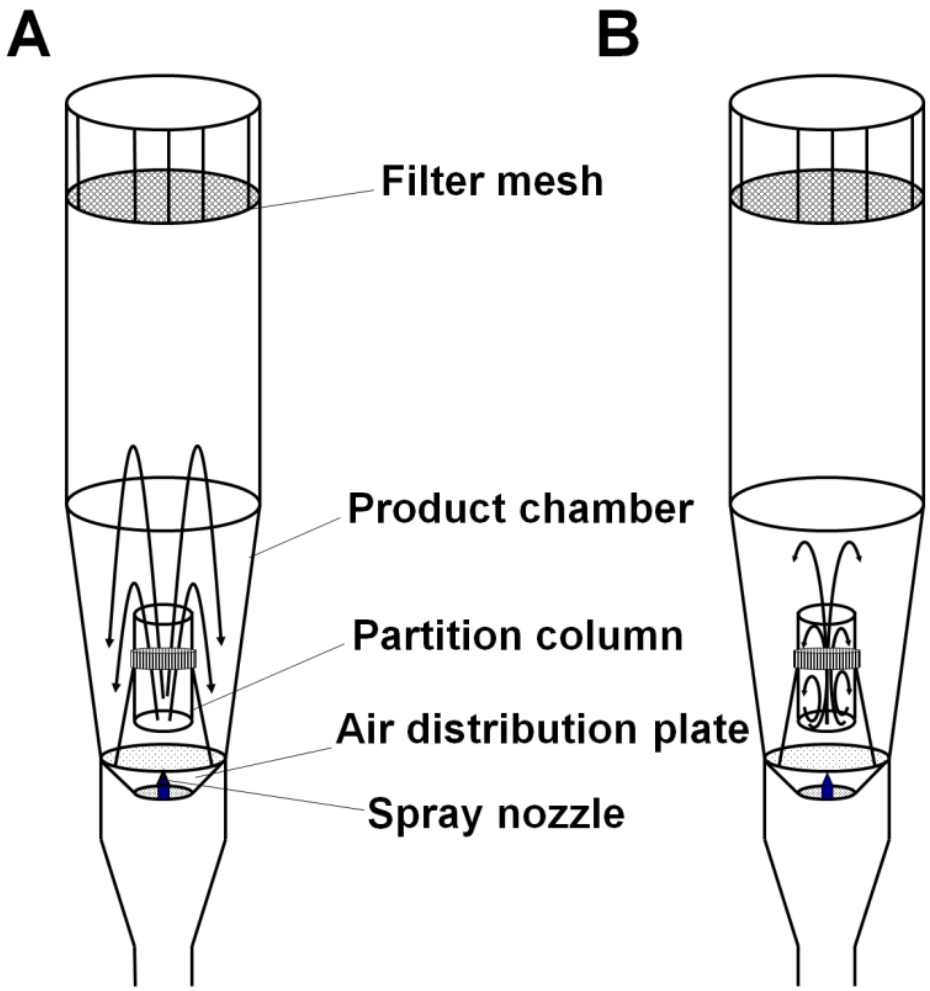

Figure 10. (A) Ideal particle motion without recirculation, (B) actual particle motion joining recirculation within the partition column

Although PEPT can be used for quantifying particle recirculation within the partition column, the gamma camera is difficult to scale up and real-time monitoring is not feasible as the only motion of a single particle can be measured. High speed video imaging was used due to its non-invasive nature and capability to capture the fast particle movement within partition column.

Hence, for the bottom spray fluid bed coating process, the first objective was to develop a visiometric process analyzer for real-time monitoring of particle recirculation within the partition column.

1.F.2. The mechanism of particle recirculation within the partition column

Although particle recirculation within the partition column is considered as a major variability source in bottom spray fluid bed coating, the mechanism of particle recirculation is still unknown. This is mainly because particle recirculation is largely hidden from the operators and there is no process analyzer available to quantify this phenomenon. The mechanism of particle recirculation needs to be investigated to gain a better understanding of the bottom spray fluid bed coating process as it is beneficial to process design and control. Hence, for the study on bottom spray fluid bed coating, the second objective was to investigate the mechanism of particle recirculation within the partition column.

1.F.3. Particle mass flow rate

Particle mass flow rate (MFR) also needs to be monitored and controlled on-line due to two reasons. Firstly, coating is a layering process and coat uniformity is affected by the total number of passes through the spray zone. Under a fixed spray rate, particles are coated more uniformly with a greater number of passes through the spray zone (Crites and Turton, 2005). Hence, particle MFR affects coat uniformity. Secondly, as the "fountain-like" particle movement within the coater is the most basic characteristic flow pattern of the bottom spray fluid bed coating process, particle MFR can serve as an effective

indicator of the "fountain-like" motion. For example, a sudden reduction in MFR may indicate severe agglomeration; sudden changes in MFR may be caused by deviation of air flow rate or atomizing air pressure; an unsteady particle MFR indicates that "choking" or fast fluidization is occurring and an increase in fluidizing air is needed (Geldart and Rhodes, 1985; Bi *et al.*, 1993; Grace and Bi, 1997). The current MFR measurement method collects particles by placing an additional particle collector inside the product chamber, stopping particle cycling and recording the time taken for all the particles to flow into the collector (Chan *et al.*, 2006). MFR can be calculated according to the following equation:

$$MFR = \frac{M_t}{t} \quad (1)$$

where M_t is the load of particles and t is the time for particles to flow into the collector. However, this method has two limitations. Firstly, MFR can only be measured at the start-up of the process, when the fluidizing air and MFR have yet to stabilize. Secondly, this method cannot be developed as a process analyzer due to its invasive and interruptive nature. As such, it is highly desirable to develop a method that is capable of accurately measuring particle MFR on-line for the bottom spray fluid bed coating process. For bottom spray fluid bed coating, the third objective was to develop a visiometric process analyzer that is able to measure particle MFR online.

1.F.4. Annular bed flow pattern

The influence of annular bed flow pattern on bottom spray fluid bed coating has largely been neglected with few studies carried out on annular bed flow patterns. In previous studies, the influences of annular bed flow pattern were

confounded by particle recirculation within the partition column and particle MFR (Xu and Turton, 1997; Sudsakorn and Turton, 2000; Crites and Turton, 2005). Without experimental support, bubbling fluidization pattern was described qualitatively and mathematically as the default annular bed flow pattern (Crites and Turton, 2005). As a result, the types and behaviour of annular bed flow patterns remained unclear. Furthermore, the influence of annular bed flow pattern on particle coat uniformity has not been determined experimentally. Therefore, there is a need to systematically study annular bed flow pattern and its possible influences on particle coating, particularly on coat uniformity. Hence, for bottom spray fluid bed coating, the last objective was to classify annular bed flow pattern and study the influence of annular bed flow pattern on coat uniformity. Moreover, it is also desirable to investigate the feasibility of using a visiometric process analyzer to monitor annular bed flow pattern in a real-time manner.

CHAPTER 2. HYPOTHESIS AND OBJECTIVES

CHAPTER 2. HYPOTHESIS AND OBJECTIVES

2.A. Hypothesis

As shown in Chapter 1, the spaces for reprocessing are generally limited for pharmaceutical products. Monitoring of both the end product quality attributes and the progress of the process are desirable for better process understanding and control. However, there are few process analyzers available at present. It is thus advantageous to develop process analyzers that are able to predictively track the progress of a process rather than simply measuring the end product characteristics, which are the outcomes and down-stream of the process. In-process material flow pattern may be used to monitor the status of the process as in-process material flow pattern influences the extent of mass, heat and momentum transfer and in-process material flow pattern may also reflect the end product quality attributes. Visiometric process analyzers, which are based on imaging and image analysis methods, are preferred for quantifying flow pattern due to their accuracy and non-invasive nature. The focus of this study was on extrusion-spheronization and bottom spray fluid bed coating, which are the major processes for manufacture of multiparticulate dosage forms. It was hypothesized that visiometric process analyzers can be developed for better understanding and control of manufacturing, extrusion-spheronization and bottom spray fluid bed coating.

2.B. Objectives

Under the QbD framework, research gaps in extrusion-spheronization and bottom spray fluid bed coating are summarized below:

- **Research gaps in the spheronization process**
  - The particle growth kinetics during spheronization is still not clear, especially for lower MCC content formulations. The influences of a relatively broad range of spheronization speeds and water contents on particle growth kinetics are not well understood as well.
  - Based on the theory of fast sheared dry granular materials, the particle motion in the near plate region may affect particle growth kinetics due to massive collision between particles (Jenkins, 1998; Taberlet *et al.*, 2007). However, in the spheronization process, the relationship between particle motion in the near plate region and particle growth kinetics is not known.
  - Although it is accepted that bed surface flow pattern is indicative of extrudate plasticity, efforts have yet been taken to systematically quantify and investigate the relationship between bed surface flow pattern and particle growth kinetics.

- **Research gaps in bottom spray fluid bed coating**
  - Particle recirculation within the partition column of the bottom spray fluid bed coater is considered as a major variability source influencing coat uniformity in bottom spray fluid bed coating. However, no

process analyzer is available for quantifying particle recirculation probability in a timely manner.

- The mechanism of particle recirculation within the partition column is not known.
- Although particle MFR affects coat uniformity and gives valuable information about the bottom spray fluid bed coating process, there are no process analyzers available for online particle MFR measurement.
- The effects of annular bed flow pattern in coat uniformity were confounded by other factors, i.e. particle recirculation within the partition column and particle MFR. It is desirable to develop a visiometric process analyzer to classify and systematically study influence of annular bed flow patterns on coat uniformity experimentally.

In view of the hypothesis and research gaps, the following objectives were targeted.

- **Objectives for spheronization**
  - To determine particle growth kinetics with respect to the influences of relatively broad ranges of water contents and spheronization speeds.
  - To investigate the relationship between particle motion in the near plate region and particle growth kinetics. To study the feasibility of using fast sheared dry granular theory to model particle motion in the near plate region.
  - To study the relationship between bed surface flow pattern and particle growth kinetics.

- **Objectives for bottom spray fluid bed coating**
  - To develop a visiometric process analyzer for quantifying particle recirculation probability within the partition column of the bottom spray fluid bed coater.
  - To investigate the mechanism of particle recirculation within the partition column of the bottom spray fluid bed coater.
  - To develop a visiometric process analyzer that is capable of quantifying particle MFR online for the bottom spray fluid bed coating process.
  - To classify the annular bed flow pattern and determine the influence of annular bed flow patterns on coat uniformity experimentally.

The results of this PhD project can provide a better understanding of the extrusion-spheronization and bottom spray fluid bed coating processes. Better process control is expected by using the developed visiometric process analyzers.

CHAPTER 3. EXPERIMENTAL WORKS

CHAPTER 3. EXPERIMENTAL WORKS

3.A. Material

3.A.1. Materials for extrusion-spheronization

Lactose α-monohydrate particles (200M, Pharmatose, DMV-Fonterra Excipients, the Netherlands) was used as a filler and microcrystalline cellulose (MCC, PH-101, Avicel, FMC BioPolymer, USA) was used as the spheronization aid. Deionised water was used as the granulating fluid in the wet massing stage of the extrusion-spheronization process.

3.A.2. Materials for bottom spray fluid bed coating study

Sugar pellets (1.72 g/cm^3 density, Hanns G. Werner, Germany) of three different size fractions, i.e. 355-425 μm, 500-600 μm and 710-850 μm, respectively, were used as the cores for coating. Hydroxypropyl methylcellulose (HPMC, E3-LV, Dow Chemical, USA) was used to base-coat the sugar pellets to protect pellet integrity. HPMC aqueous solution of 10% w/w was obtained by dispersing in hot water and then hydrating in the refrigerator overnight. A red colour pigmented aqueous suspension (10% w/w, Opadry II, Colourcon, USA) was used to colour-coat the sugar pellets.

3.B. Development of visiometric process analyzer

High speed video imaging, PIV and morphological image processing are the three common pillars in the development of visiometric process analyzers for a better understanding and control of the processes, spheronization and bottom spray fluid bed coating in particular. High speed video imaging was used to capture sequential images of in-process material and PIV was employed to detect in-process material flow patterns. A range of morphological image

processing techniques was also used to preprocess the high speed images as well as extract morphological information from the high speed images.

3.B.1. High speed video imaging

The high speed video images of in-process material flow were captured using a high speed video camera (MotionPro HS-3, Red Lake, USA). The camera was controlled by calling the routines of the Red Lake software development kit in Matlab (R2007b, The MathWorks, USA). A set of high speed images was precisely captured at the predefined time points. The software control of pulsed imaging served as a means of time-series sampling, thus ensuring good representativeness of captured images in the different studies. Moreover, precise imaging pulses controlled by Matlab allowed for accurate monitoring of the spheronization process. Major parameters for high speed video imaging include imaging recording speed (in frames per second, fps, in short), image size (pixels by pixels as well as actual size), number of recording pulses and duration of each pulse.

3.B.2. Particle image velocimetry

In digital PIV, the adjacent images are divided into sub-images; the central parts (usually up to one-ninth of the total area of the sub-images) of sub-images in the first image were taken and roamed within the corresponding sub-images in the second image. The similarities between the roaming parts from the first image and the stationary parts from the second image were determined. The displacement that maximizes the similarity is then considered as the average displacement of the sub-image. Cross-correlation and MQD are the two major methods for determining similarity between roaming parts and

stationary parts. The two-dimensional (2D) correlation coefficients $c_{II}(x, y)$ were calculated according to equations (2-5) (Raffel *et al.*, 2007):

$$c_{II}(\Delta x, \Delta y) = \frac{cT_{II}(\Delta x,\Delta y)}{\sqrt{\sigma_I(\Delta x,\Delta y)} \times \sqrt{\sigma'_I(\Delta x,\Delta y)}} \quad (2)$$

where

$$cT_{II}(\Delta x, \Delta y) = \sum_{i=1}^{M}\sum_{j=1}^{N}[I(i,j) - \mu_I][I'(i+\Delta x, j+\Delta y) - \mu_{I'}(i+\Delta x, j+\Delta y)] \quad (3)$$

$$\sigma_I(\Delta x, \Delta y) = \sum_{i=1}^{M}\sum_{j=1}^{N}[I(i,j) - \mu_I]^2 \quad (4)$$

$$\sigma'_I(\Delta x, \Delta y) = \sum_{i=1}^{M}\sum_{j=1}^{N}[I'(i,j) - \mu_{I'}(i+\Delta x, j+\Delta y)]^2 \quad (5)$$

where *I(i, j)* is the image intensity field of the template at position *(i, j)* from the first frame, *I'(i+Δx, j+Δy)* is the image intensity field of the template at position *(i+Δx, j+Δy)* from the second frame, μ_I is the average intensity of the template and $\mu_{I'}(i + \Delta x, j + \Delta y)$is the average intensity of *I'* coincident with the template *I* at position *(i+Δx, j+Δy)*. The cross-correlation coefficient, $c_{II}(\Delta x, \Delta y)$, ranges from -1 to 1, where a negative result indicates negative correlation and a positive result indicates positive correlation. *M* and *N* are height and width of the template respectively.

Quadratic difference C_{MQD} was calculated as follows (Suh, 2003):

$$C_{MQD}(\Delta x, \Delta y) = \sum_{i=1}^{M}\sum_{j=1}^{N}|I(i,j) - I'(i+\Delta x, j+\Delta y)| \quad (6)$$

For investigation on particle recirculation in bottom spray fluid bed coating, a programme written in Matlab was employed for ensemble correlation analysis. PIV analyses in the rest of this project were carried out using the Matlab functions of MPIV toolbox (Mori and Chang, 2006). Overlapping ratio between neighbouring sub-images and the size of sub-images are the major parameters for PIV analyses. An overlapping ratio of 0.5 is most frequently

used (Mori and Chang, 2006). Based on the image recording speed information and the in-process material displacement results from PIV, the velocity of in-process material flow pattern can be calculated.

Due to the large amount of data to be analyzed (over 500 GB in total) and the time-consuming PIV analysis (typically around 1 minute for one image pair of 1280-by-1024-pixels), a Matlab distributed computing cluster was used for PIV analysis. In the Matlab distributed computing, the data to be analyzed and the analysis code were first upload to the scheduler, which is the server coordinating computers at a higher level. Then the scheduler distributes computing tasks equally to computational work stations at a lower level (Figure 11). The scheduler collects computational results after the assigned computational tasks are finished. The computing results can be downloaded from the scheduler after the completion of all the computational tasks.

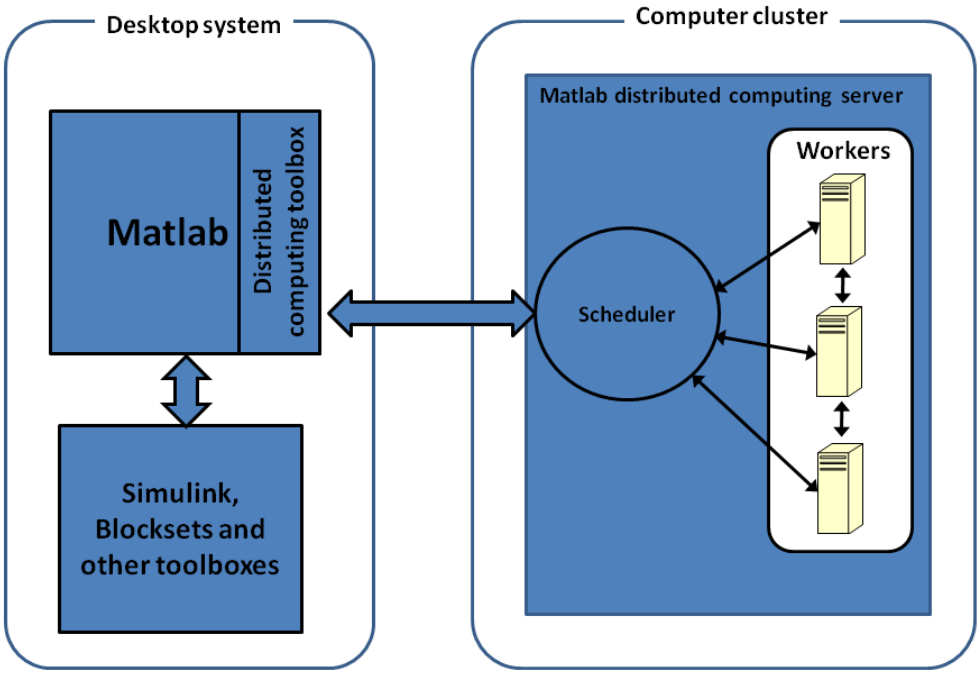

Figure 11. Schematic diagram of Matlab distributed computing cluster (adapted from the MathWorks, 2010)

3.B.3. Morphological image processing

Morphological image processing extracts relevant structures of the image by probing the image with another set of known shape called structuring element (Soille, 2003c). A combination of several elementary operations was used for morphological image processing due to the different characteristics in each individual problem to be solved. The definitions of the basic morphological image processing operations used in this project are given below.

The gray-scale dilation and erosion of image *f* are defined as (Gonzalez *et al.*, 2004b):

$$(f \oplus b)(x,y) = max\{f(x-x', y-y') + b(x',y') \in D_b\} \quad (7)$$

and

$$(f \ominus b)(x,y) = min\{f(x+x', y+y') - b(x',y') \in D_b\} \quad (8)$$

respectively, where b is the structuring element and D_b is the domain of b. Accordingly, gray-scale opening $f \circ b$ of an image f was defined as:

$$f \circ b = (f \ominus b) \oplus b \quad (9)$$

For morphological opening, a flat disk shaped structuring element was created and used to probe the image. The disk shaped structuring element was approximated by a sequence of 4 periodic lines (Jones, 1996).

Regional maxima are connected components of pixels with a constant intensity value with all the external boundary values having smaller intensity values. The regional maxima were set as 1 and all the other pixels were set as 0 (Soille, 2003b).

Image reconstruction dilates a marker image with respect to the mask image until stability is achieved (Soille, 2003b). In image labelling process, different gray-scale values were used for each connected components and the assigned gray-scale values are called labels. The number of labels corresponds to the number of connected components and hence, the number of particles to be counted (Soille, 2003c). Morphological opening, regional maxima, image reconstruction and image labelling were performed using the built-in functions in the Matlab image processing toolbox.

Thresholding is a process that extracts the objects from the background by selecting a threshold *T* that separates these modes (Gonzalez *et al.*, 2004a):

$$h(x,y) = \begin{cases} 1 \; if \; f(x,y) \geq T \\ 0 \; if \; f(x,y) < T \end{cases} \tag{10}$$

where $h(x,y)$ is the image after thresholding and *f(x,y)* is the original image. The threshold of the image is detected using Ostu's method, which is realized using the Matlab image processing toolbox (Otsu, 1979).

Binary image filling is defined as the operation of changing connected background pixels, i.e. 0, into foreground pixels, i.e. 1 (Gonzalez *et al.*, 2004b). Image filling stops when the object boundary is reached. For binary images, a hole is defined as background pixels that cannot be reached by filling from the edges of the image and hole filling refers to the operation of setting hole(s) into foreground pixels (Gonzalez *et al.*, 2004b).

3.C. Methods for investigations on the spheronization process

3.C.1. Extrusion-spheronization

A load of 2 kg MCC: lactose powder in a 1: 3 w/w ratio was mixed and granulated using a bottom driven high shear mixer (PMA1, Aeromatic-Fielder, GEA Pharma Systems, UK). In the dry powder mixing stage, the impeller speed was kept under 1000 rpm for 2 min. The impeller speed was then turned down to 450 rpm for wet massing and deionised water was added into the mixer at a delivery rate of 533 g/min using a peristaltic pump (323 RL, Watson-Marlow, USA). The wet mass was further mixed for 1 min after water addition. Irrespective of the different water contents, 800 g wet mass was weighed and extruded using a counter-rotating extruder (E-140, Nica^{TM}, GEA Pharma Systems, UK). The extrudates were then collected and transferred into a spheronizer (S-320, Nica^{TM}, GEA Pharma Systems, UK) for 300 seconds. A full factorial combination of 3 different water contents ($W_{content}$), i.e. 35.0%, 37.5% and 40.0% w/w, and 5 different peripheral speeds (V_{peri}), i.e. 4, 6, 8, 10, and 12 m/s, of the spheronizer frictional base plate were used. Wet masses of 35.0%, 37.5% and 40.0% water contents were used to represent low, medium and high material plasticity, respectively. Considering triplicate batches for each experimental condition, the whole design was repeated 3 times for the purpose of capturing particle motion in the near plate region and another 3 times for the purpose of studying bed surface flow pattern during spheronization. The same set of high speed images were used for particle growth kinetics determination as well as PIV analyses for particle motion in the near plate region.

3.C.2. Determination of particle growth kinetics during spheronization

3.C.2.1. High speed video imaging

The high speed images of moving particles in the near plate region, i.e. the region above the frictional base plate were captured using the high speed video camera. This was achieved by replacing the product discharge plug with a piece of transparent acrylic sheet of the same size (Figures 12A and 12B). The camera was controlled using Matlab such that a 100-frame-length high speed video clip was taken with every 10 s time lapse after the start of the spheronization process. The capturing speed was 2000 fps and the image size was 520 pixels by 715 pixels, which corresponded to an actual area of 20 mm by 27.5 mm. The experimental setup for high speed video imaging is shown in Figure 12C and the time sequence for high speed photography is shown in Figure 12D.

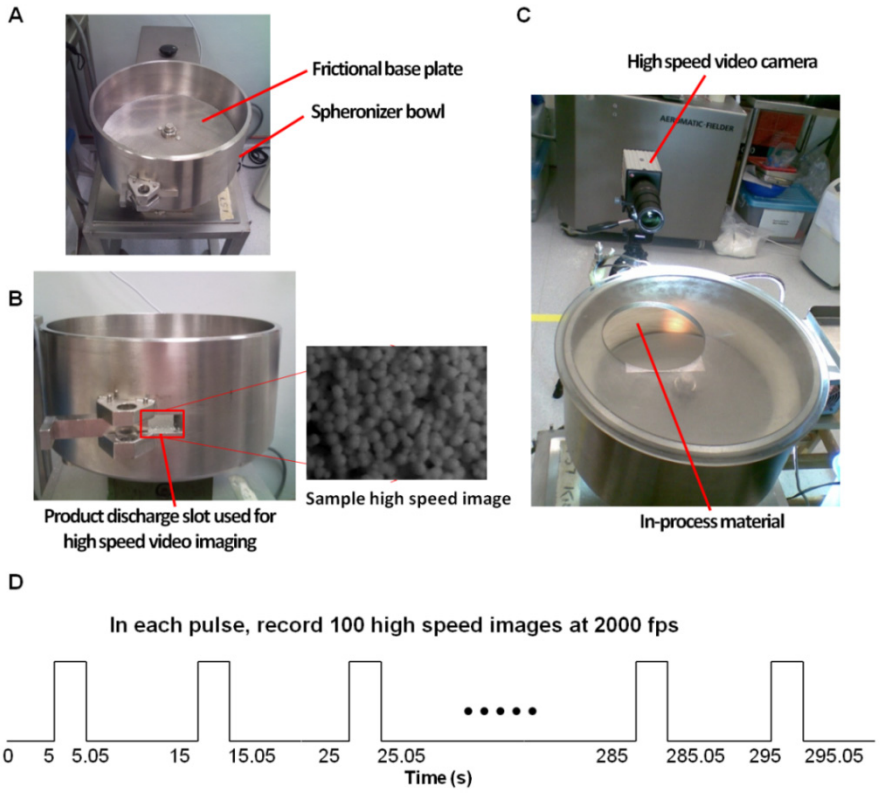

Figure 12. (A) Perspective view of spheronizer, (B) product discharge slot used for high speed video imaging, (C) high speed video imaging during spheronization process and (D) time sequence for high speed video imaging

Due to the short exposure time in high speed video imaging, highly intense light was needed. Hence, the commonly used halogen light had to be replaced to prevent the exposure of in-process material to excessive heat. A customized high power light-emitting diode (LED) array (GT-P300W, GeTian Opto-Electronics, China), was used for illumination due to its high efficiency and minimal heat generation. The high power LED array consists of 100 LED units, which have a power of 3 watt per unit. A constant current (up to 10 amps) direct current (DC) power source was used to drive the LED array. A heat sink and a cooling fan were mounted with the LED array to dissipate the heat induced by the high current (Figure 13).

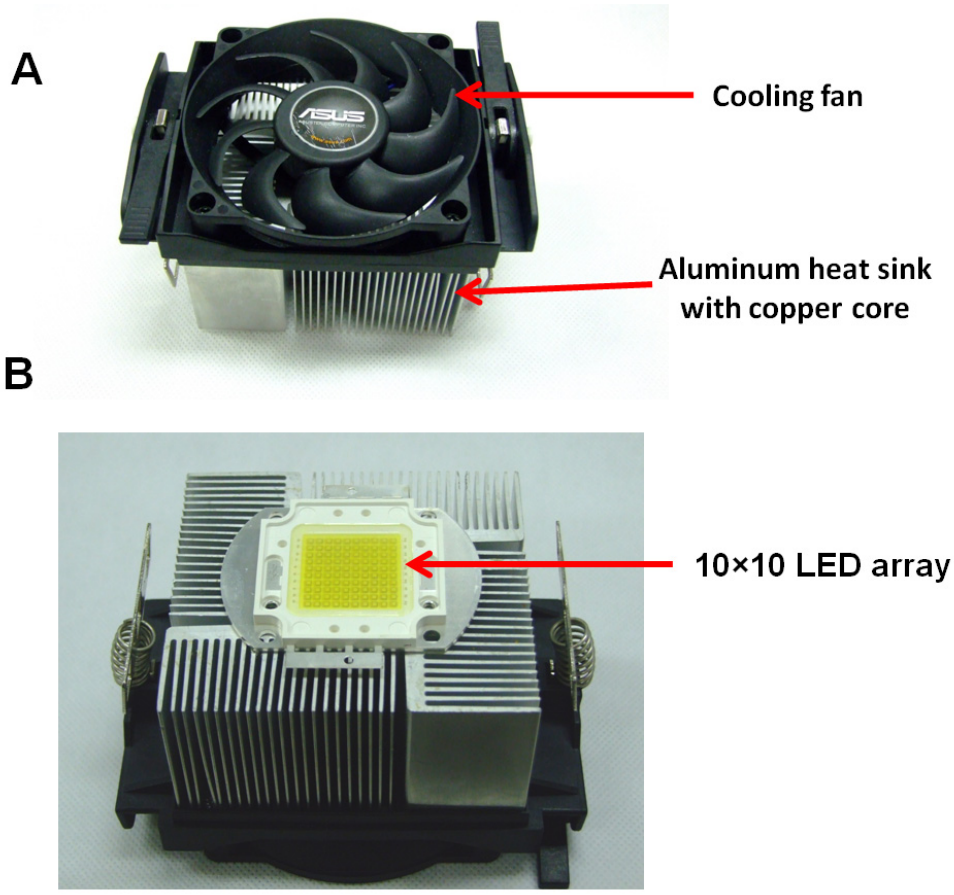

Figure 13. Images of (A) heat sink and cooling fan unit, and (B) 10×10 LED array mounted on the bottom of the heat sink

3.C.2.2. Particle sizing using Ferret diameter determination of in-process high speed images

In order to study the particle growth kinetics, the changes in particle size were monitored by measuring the Ferret diameter of particles on the high speed images. Ferret diameter is defined as distance between two parallel tangents on opposite sides of the image of a randomly oriented particle (Merkus, 2009). In this investigation, the parallel tangents that were perpendicular to the frictional base plate were chosen for Ferret diameter measurement. Spatial calibration of images and Ferret diameter measurement from a single orientation were carried out using an image analysis software (Image-Pro Plus 6.3, Mediacybernetics, USA). For each video clip, the Ferret diameters of 200 particles were determined and hence, 270,000 particles in total were measured for 1350 video clips.

3.C.2.3 Verification of Ferret diameter measurement

In order to verify the accuracy of Ferret diameter measurements, the particle size changes of a typical spheronization process was determined using high speed imaging and Ferret diameter measurement, and compared with another more accurate and widely accepted sizing method. Taking images under the optical microscope and determination of particle size according to the definition of Ferret mean diameter is considered as the "gold standard" and is adapted as the standard method for verification of Ferret diameter measurement on high speed images. Ferret mean diameter is defined as the mean value of Ferret diameter over more than one orientation (Merkus, 2009). In this investigation, for the purpose of Ferret mean diameter measurement, the image of particles was rotated 180 degrees in steps of 2 degrees. The

Ferret diameters from those steps were then averaged to yield the Ferret mean diameter.

In this investigation, 37.5% water content and 10 m/s plate peripheral speed were chosen for method verification. This was because this set of experimental conditions covered a sufficiently wide span of particle size. One sample was collected every 10 s during spheronization, and 30 in-process samples were collected into a sealed sample container to prevent moisture loss. The in-process sampling was carefully carried out and was synchronized with the recording pulses of high speed video imaging. The images of sample particles were taken under an optical microscope (SZH, Olympus, USA) immediately. The images of the sample particles were then analyzed using the image analysis software to determine the Ferret mean diameter. The root mean squared error (*RMSE*) between the two measurement results, i.e. high speed imaging coupled with Ferret diameter measurement and in-process sampling followed by Ferret mean diameter determination under the optical microscope, was then calculated. *RMSE* was defined as:

$$RMSE = \sqrt{E[(\hat{\theta} - \theta)^2]} \tag{11}$$

where E is the mean operator and $\hat{\theta}$ is the estimator with respect to the estimated parameter θ. In this investigation, $\hat{\theta}$ are the high speed imaging coupled with Ferret diameter measurement results and θ are the results from in-process sampling followed by Ferret mean diameter determination under the optical microscope.

3.C.3. Quantification of particle motion in the near plate region in relation to particle growth kinetics and mechanisms

3.C.3.1. Development of visiometric process analyzer

The same set of high speed images obtained in section **3.C.2.1** was also employed for PIV analysis in the near plate region. MQD method was employed to analyze the high speed images due to its robustness. The sub-image size was set as 32 pixels by 64 pixels as most particles moves along the frictional base plate. The overlapping ratio between sub-images was set as 0.5. Morphological image processing was not required for this particular visiometric process analyzer.

3.C.3.2. Calculation of mean particle speed ($\overline{V^{total}}$) and granular temperature (GT^{total}) in the near plate region

PIV analysis of the k^{th} pair of images at time point, t, returns a speed matrix:

$$V_k^t = \begin{bmatrix} v_{11}^k & v_{12}^k & v_{13}^k & \dots & v_{1n}^k \\ v_{21}^k & v_{22}^k & v_{23}^k & \dots & v_{2n}^k \\ v_{31}^k & v_{32}^k & v_{33}^k & \cdots & v_{3n}^k \\ \vdots & \vdots & \vdots & v_{ij}^k & \vdots \\ v_{m1}^k & v_{m2}^k & v_{m3}^k & \cdots & v_{mn}^k \end{bmatrix} \quad (12)$$

where v_{ij}^k corresponds to the speed detected at position d_{ij} in the position matrix $D = \begin{bmatrix} d_{11} & d_{12} & d_{13} & \dots & d_{1n} \\ d_{21} & d_{22} & d_{23} & \dots & d_{2n} \\ d_{31} & d_{32} & d_{33} & \cdots & d_{3n} \\ \vdots & \vdots & \vdots & d_{ij} & \vdots \\ d_{m1} & d_{m2} & d_{m3} & \cdots & d_{mn} \end{bmatrix}$ (13)

where d_{ij} denotes a position that is d_i mm away from the left border and d_j mm away from the bottom border of the image. D is determined by the image size, sub-image size as well as the overlapping ratio. Hence, the position matrix is fixed as long as the same set of PIV parameters was used. According to the settings for high speed video imaging mentioned in section **3.C.2.1.**, 100

frames of high speed images were taken at the time points of 5, 15, 25... 295 s. Hence, for each time point, 99 speed matrices are available, i.e. $V_1^t, V_2^t, V_3^t \ldots V_{99}^t$, and the vector containing mean speed, $\overline{V^t}$, at time point *t* was calculated by averaging speeds that are located at equal distances from the frictional base plate through all the 99 speed matrices at time point *t*:

$$\overline{V^t} = \begin{bmatrix} \sum_{k=1}^{99}\sum_{j=1}^{n} v_{1j}^k/99 \times n \\ \sum_{k=1}^{99}\sum_{j=1}^{n} v_{2j}^k/99 \times n \\ \sum_{k=1}^{99}\sum_{j=1}^{n} v_{3j}^k/99 \times n \\ \vdots \\ \sum_{k=1}^{99}\sum_{j=1}^{n} v_{mj}^k/99 \times n \end{bmatrix} \equiv \begin{bmatrix} \vartheta_1^t \\ \vartheta_2^t \\ \vartheta_3^t \\ \vdots \\ \vartheta_m^t \end{bmatrix} \tag{14}$$

where $\overline{V^t}$ is a $m \times 1$ vector and hence, all the mean speed information through all the time points of the spheronization process can be expressed as:

$$\overline{V^{total}} = [\overline{V^5} \quad \overline{V^{15}} \quad \overline{V^{25}} \quad \ldots \quad \overline{V^{295}}] \equiv \begin{bmatrix} \vartheta_1^5 & \vartheta_1^{15} & \vartheta_1^{25} & \cdots & \vartheta_1^{295} \\ \vartheta_2^5 & \vartheta_2^{15} & \vartheta_2^{25} & \cdots & \vartheta_2^{295} \\ \vartheta_3^5 & \vartheta_2^{15} & \vartheta_3^{25} & \cdots & \vartheta_3^{295} \\ \vdots & \vdots & \vdots & \vartheta_j^t & \vdots \\ \vartheta_m^5 & \vartheta_m^{15} & \vartheta_m^{25} & \cdots & \vartheta_m^{295} \end{bmatrix} \tag{15}$$

where ϑ_j^t refers to the total mean speed of all detected speed at time point *t* and d_j mm away from the bottom plate.

Granular temperature, *GT*, is defined as follows (Brilliantov and Poschel, 2004):

$$GT = \frac{1}{3} \times \left[\frac{\sum_{i=1}^{q} c_i^2}{q}\right] \tag{16}$$

where c_i is the fluctuating speed with respect to the mean speed: $c_i = v_i - \bar{v}$, q is the number of fluctuating speed involved in the calculation of granular temperature. Granular temperature is a parameter frequently used in the kinetics theory and is an indicator of fluctuating energy. With respect to the

investigation of particle motion in the near plate region, the granular temperature at time point *t*, GT^t, is defined as follow:

$$GT^t = \begin{bmatrix} \frac{1}{3} \times (\sum_{k=1}^{99} \sum_{j=1}^{n} (v_{1j}^k - \vartheta_1^t)^2 / 99 \times n) \\ \frac{1}{3} \times (\sum_{k=1}^{99} \sum_{j=1}^{n} (v_{2j}^k - \vartheta_2^t)^2 / 99 \times n) \\ \frac{1}{3} \times (\sum_{k=1}^{99} \sum_{j=1}^{n} (v_{3j}^k - \vartheta_3^t)^2 / 99 \times n) \\ \vdots \\ \frac{1}{3} \times (\sum_{k=1}^{99} \sum_{j=1}^{n} (v_{mj}^k - \vartheta_m^t)^2 / 99 \times n) \end{bmatrix} \equiv \begin{bmatrix} GT_1^t \\ GT_2^t \\ GT_3^t \\ \vdots \\ GT_m^t \end{bmatrix} \quad (17)$$

Similarly, GT^t is also a $m \times 1$ vector and hence, the total granular temperature through all the time points of the spheronization process can be expressed as:

$$GT^{total} = [GT^5 \quad GT^{15} \quad GT^{25} \quad \cdots \quad GT^{295}] \equiv$$

$$\begin{bmatrix} GT_1^5 & GT_1^{15} & GT_1^{25} & \cdots & GT_1^{295} \\ GT_2^5 & GT_2^{15} & GT_2^{25} & \cdots & GT_2^{295} \\ GT_3^5 & GT_2^{15} & GT_3^{25} & \cdots & GT_3^{295} \\ \vdots & \vdots & \vdots & GT_j^t & \vdots \\ GT_m^5 & GT_m^{15} & GT_m^{25} & \cdots & GT_m^{295} \end{bmatrix} \quad (18)$$

where GT_j^t refers to the total mean granular temperature of all detected speeds at time point *t* and d_j mm away from the bottom plate.

3.C.3.3. Visualization of total mean speed ($\overline{V^{total}}$) and total mean granular temperature (GT^{total}) in the near plate region

The objective of section **2.C.3.** was to investigate the relationship between particle motion in the near region and particle growth kinetics. Hence it is desirable to plot changes in particle size together with total mean speed, i.e.$\overline{V^{total}}$, and total mean granular temperature, i.e.GT^{total}, respectively. The concept of dimensionless plot was introduced from the area of granular physics (Taberlet *et al.*, 2007). In the normal three-dimensional (3D) surface plot, the total mean speed matrix, i.e.

$\overline{V^{total}} \equiv \begin{bmatrix} \vartheta_1^5 & \vartheta_1^{15} & \vartheta_1^{25} & \cdots & \vartheta_1^{295} \\ \vartheta_2^5 & \vartheta_2^{15} & \vartheta_2^{25} & \cdots & \vartheta_2^{295} \\ \vartheta_3^5 & \vartheta_2^{15} & \vartheta_3^{25} & \cdots & \vartheta_3^{295} \\ \vdots & \vdots & \vdots & \vartheta_j^t & \vdots \\ \vartheta_m^5 & \vartheta_m^{15} & \vartheta_m^{25} & \cdots & \vartheta_m^{295} \end{bmatrix}$ or the total mean granular temperature matrix, i.e. $GT^{total} \equiv \begin{bmatrix} GT_1^5 & GT_1^{15} & GT_1^{25} & \cdots & GT_1^{295} \\ GT_2^5 & GT_2^{15} & GT_2^{25} & \cdots & GT_2^{295} \\ GT_3^5 & GT_2^{15} & GT_3^{25} & \cdots & GT_3^{295} \\ \vdots & \vdots & \vdots & GT_j^t & \vdots \\ GT_m^5 & GT_m^{15} & GT_m^{25} & \cdots & GT_m^{295} \end{bmatrix}$, were plotted against the time matrix $\begin{bmatrix} 5 & 15 & 25 & \ldots & 295 \\ 5 & 15 & 25 & \ldots & 295 \\ 5 & 15 & 25 & \cdots & 295 \\ \vdots & \vdots & \vdots & t & \vdots \\ 5 & 15 & 25 & \cdots & 295 \end{bmatrix}$ and distance from the frictional base plate matrix $\begin{bmatrix} d_1 & d_1 & d_1 & \ldots & d_1 \\ d_2 & d_2 & d_2 & \ldots & d_2 \\ d_3 & d_3 & d_3 & \cdots & d_3 \\ \vdots & \vdots & \vdots & d_j & \vdots \\ d_m & d_m & d_m & \cdots & d_m \end{bmatrix}$.

In dimensionless plot, the speed matrix and the time matrix remained unchanged. However, the distance from the frictional base plate matrix was changed

into $\begin{bmatrix} d_1/mpz_5 & d_1/mpz_{15} & d_1/mpz_{25} & \ldots & d_1/mpz_{295} \\ d_2/mpz_5 & d_2/mpz_{15} & d_2/mpz_{25} & \ldots & d_2/mpz_{295} \\ d_3/mpz_5 & d_3/mpz_{15} & d_3/mpz_{25} & \cdots & d_3/mpz_{295} \\ \vdots & \vdots & \vdots & d_j/mpz_t & \vdots \\ d_m/mpz_5 & d_m/mpz_{15} & d_m/mpz_{25} & \cdots & d_m/mpz_{295} \end{bmatrix}$ (19)

where mpz_t is the mean particle size at time t measured using Ferret diameter measurement. As d_1, $d_2 \ldots d_m$ were determined by the PIV parameters and they were fixed values, the changes in mean particle size can be directly obtained by examining the degree of compression of the surface mesh along the dimensionless axis.

3.C.3.4. Particle speed distribution within the fluidization zone

The particle speed located on the last three rows nearest to the frictional base plate were collected and calculated for their amplitudes. The actual calculated thickness is around 1.5 mm above the frictional base plate, thus reflecting the particle speed in the fluidization zone. The particle speed distribution was then plotted against time points and fitted using the Maxwell distribution as well as the sum of two Gaussian distributions. Maxwell distribution was used in the fitting process because it is the speed distribution of fast sheared elastic granular material (Brilliantov and Poschel, 2004). Gaussian distribution was also employed as it is the most common distribution for modelling random variables. The sum of two Gaussian distributions was used to model potential multimodal speed distributions.

The Maxwell distribution is defined as follows (Brilliantov and Poschel, 2004):

$$p(v) = \sqrt{\frac{2}{2\pi}} \times \frac{v^2 e^{-v^2/2a^2}}{a^3} \tag{20}$$

where p is the probability of particles with certain speed v and a is the parameter to be fitted.

The sum of two Gaussian distributions is defined as:

$$p(v) = a_1 \times e^{[-((v-b_1)/c_1)^2]} + a_2 \times e^{[-((v-b_2)/c_2)^2]} \tag{21}$$

where $a_1, b_1, c_1, a_2, b_2, c_2$ are the parameters to be fitted.

3.C.4. Quantification of bed surface flow pattern in relation to particle growth kinetics

3.C.4.1. Development of visiometric process analyzer

The high speed camera was placed above the spheronizer and the LED light was used to prevent moisture loss during experimentations. The schematic diagram for experiment setup is shown in Figure 14. The time sequences for high speed photography were the same as given in Figure 12D and the recording speed was 400 fps. The image size was set as 1024 pixels by 1280 pixels, which corresponded to an actual area of 370 mm by 463 mm. MQD method was used for interrogating sequential images; a 32-by-32 pixels sub-image and an overlapping ratio of 0.5 were used.

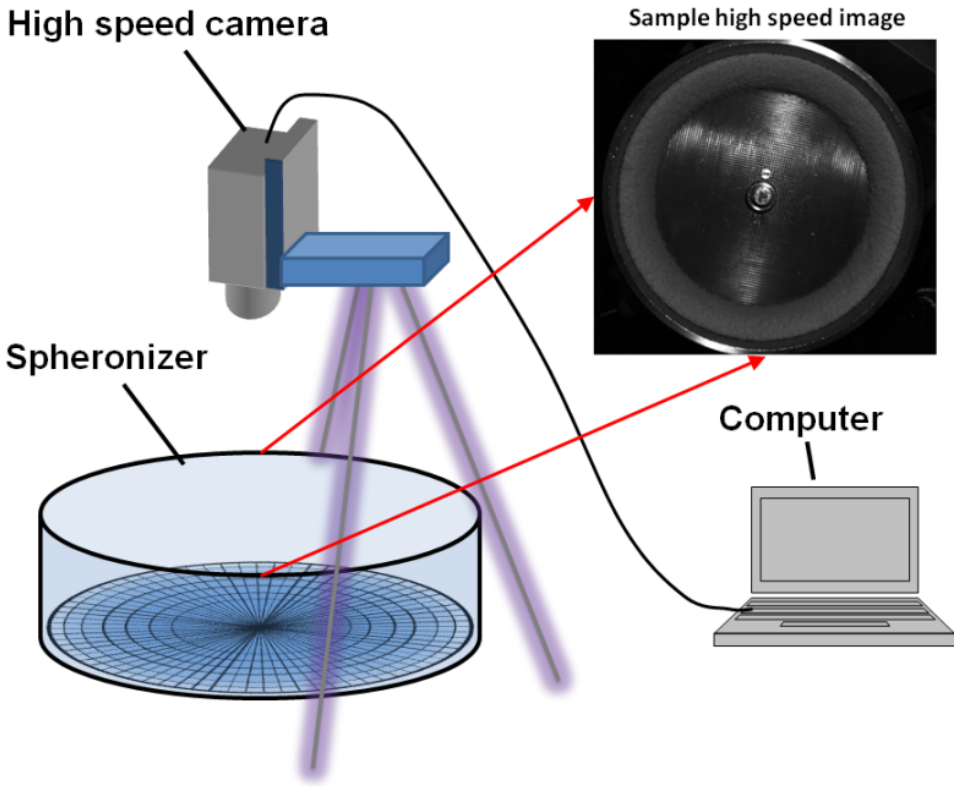

Figure 14. Schematic diagram of high speed video imaging of spheronization bed surface

Not all the velocity vectors from raw PIV results belong to the in-process material. For example, the velocity of the frictional base plate may also be picked up by the PIV algorithm. Hence, the aim of post-processing was to filter velocity vectors that do not belong to the ring shaped in-process material bed surface. Post-processing of PIV results included the following steps.

Firstly, the thresholding operation was employed to convert gray-scale images into binary images. Secondly, the holes on the image were filled. Thirdly, the minor white objects were cleared. Fourthly, the outline of the major white object was tracked and a circle was fitted into the outline using the least square method. Finally, in order to determine the inner radius of the ring shaped in-process material bed surface, a series of circles were drawn based on the detected centre with increasing radius from 0 to the outer boundary, at a step of 1 pixel. Then the mean gray-scale intensity of pixels located on each circle was calculated and the circle with the lowest mean gray-scale intensity of pixels corresponded to the inner radius of the ring shaped in-process material bed surface. This was because the LED light was located above the centre of the spheronizer. The light intensity reflected by the frictional base plate decayed from the centre and in-process material reflected light stronger than the frictional base plate on the average. In the final step, the velocity vectors lying outside the ring shaped in-process material bed surface were removed.

3.C.4.2. Visualization of bed surface flow pattern and particle growth kinetics using 3D scatter plot

In the investigation on bed surface flow pattern, the bed surface mean speed at time point *t*, $\overline{V_{surf}^{t}}$, was calculated by averaging the amplitudes of all the filtered velocity vectors through all the 99 speed matrixes at time point *t*:

$$\overline{V_{surf}^{t}} = \sum_{k=1}^{99} \sum_{i=1}^{m} \sum_{j=1}^{n} v_{ij}^{k} \quad (22)$$

3D scatter plot was then used to visualize the mean speed of bed surface, $\overline{V^{t}}$, with respect to spheronization time, *t*, as well as mean particle size at *t*, mpz_t.

3.D. Methods for investigations on bottom spray fluid bed coating process

3.D.1. Development of visiometric process analyzer for quantification of particle recirculation probability within the partition column

3.D.1.1. High speed video imaging of particles moving within the partition column

The base-coated particles (700 g) were loaded into the product chamber of a bottom spray fluid bed coater (Wurster module, MP-1, Aeromatic-Fielder, GEA Pharma Systems, UK). Transparent acrylic partition column and product chamber were used so that high speed images of the particles within the partition column could be captured by a high speed video camera. The partition column and product chamber were pre-treated with a static control detergent (Static Remover 8001, 3M, USA) to prevent static charge development. The partition gap between the partition column and the air distribution plate was set at 10 mm. The air flow rate and atomizing air pressure were set at 90 m^3/h and 1.5 bar respectively. The high speed video camera recorded video clips of a 1 cm by 1 cm area (248 pixels by 248 pixels image) in the middle of the partition column (Figure 15). The exposure time of

the camera was 100 μs and the recording speed was 4219 fps. Five video clips with 100 frames in each clip were recorded.

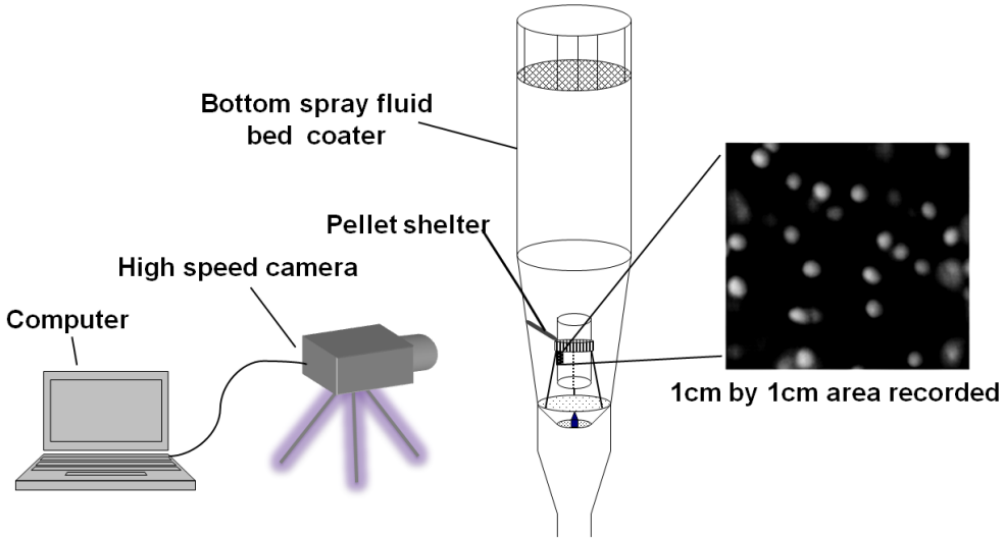

Figure 15. Schematic representation of high speed video imaging system setup for capturing particle movement in the bottom spray fluid bed coater

3.D.1.2. Morphological image processing

For the purpose of investigating the influence of particle image diameter on measurement accuracy, two copies of high speed images were prepared. One set was analyzed directly using ensemble correlation PIV while the other set was pre-processed using morphological image processing to decrease particle image diameter before ensemble correlation PIV was applied.

The high speed images were analyzed using Matlab. The flow chart for morphological image processing is shown in Figure 16. A disk shaped structuring element with 2 pixels diameter was used in the morphological opening operation. Morphological image processing was carried out using the method described by Soille (Soille, 2003a; 2003b; 2003d).

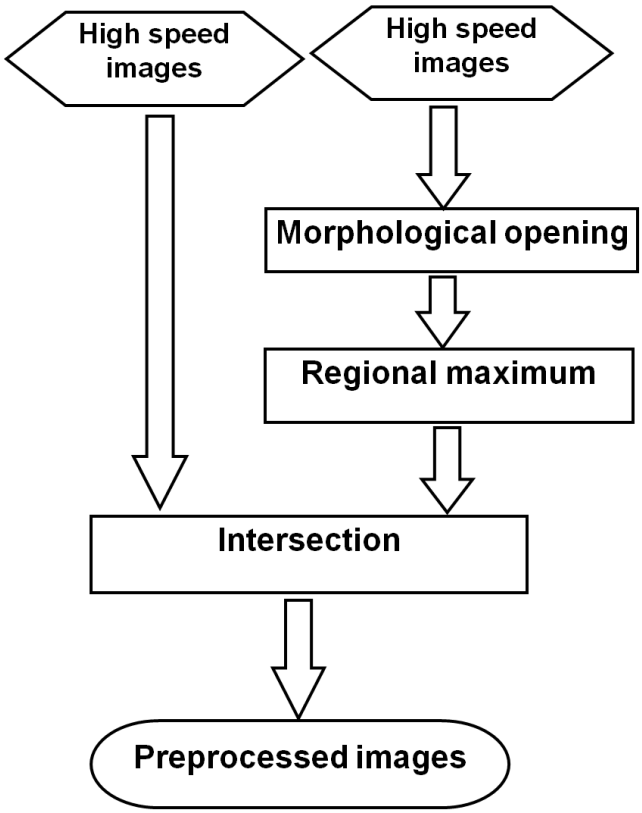

Figure 16. Flow chart of image pre-processing for images of moving particles in the partition column of the bottom spray fluid bed coater

3.D.1.3. Ensemble correlation PIV

Pre-processing and ensemble correlation PIV of high speed images were analyzed using Matlab. The correlation template was set as one ninth of the full image area. Cross-correlation method was selected for template matching. In ensemble correlation PIV, the calculated cross-correlation planes from adjacent frames were summed and averaged for noise suppression as well as particle displacement probability density function (PDF). This procedure is illustrated in Figure 17. The results from a single correlation plane, 20, 100, and 500 correlation planes were calculated separately to determine the effect of noise suppression.

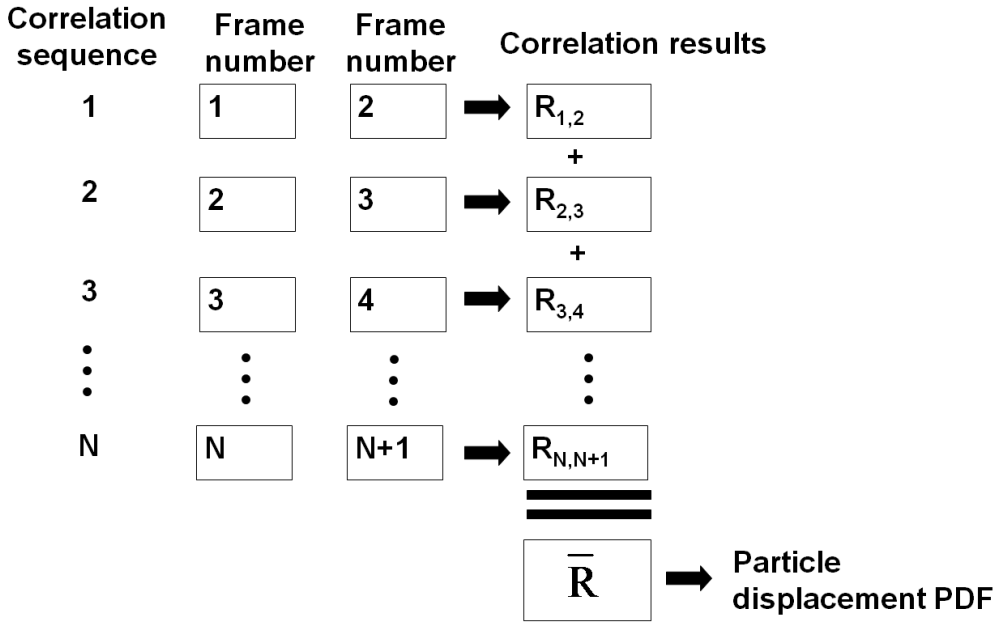

Figure 17. Procedure for ensemble correlation PIV

3.D.1.4. Verification of particle displacement PDF by image tracking

This study represented the very first effort to apply ensemble correlation PIV to the bottom spray fluid bed coating process. Hence, it was necessary to verify the accuracy of this method. Verification was carried out by particle tracking using the same set of high speed images. One thousand particles were randomly selected from the video clips and tracked across three frames using an image tracking software (TEMA Version 2.6, Image Systems AB, Sweden). Particle displacement (measured in pixels) was tracked and calculated by the software with the aid of human supervision. Particle displacement PDF was obtained from the tracking results to verify the particle velocity distribution data obtained from ensemble correlation PIV.

3.D.2. Mechanisms of particle recirculation within the partition column

3.D.2.1. Base-coating of sugar pellets

Sugar pellets of three different size fractions (355-425 μm, 500-600 μm and 710-850 μm respectively) were used as model particles. Particles were base-coated to 10% weight gain using HPMC to protect particle integrity.

3.D.2.2. Configuration of visiometric process analyzer for quantification of particle recirculation probability within the partition column

For the purpose of quantifying particle recirculation within the partition column, the visiometric process analyzers developed in section **3.D.1.** was used. The configurations of visiometric process analyzer setup were listed as below. A load of 1 kg base-coated particles were loaded into the product chamber of a bottom spray fluid bed coater (Precision coater module, MP-1, Aeromatic-Fielder, GEA Pharma Systems, UK). The recording speed was set as 4000 fps with a 248 pixels by 744 pixels resolution. For each combination of coating parameters, one video clip was taken in the first 12.5 ms of each second for 30 seconds (Figure 18A). AAIs with different diameters were used (Figure 18B). The combinations of coating parameters used for high speed video imaging were listed in Table 1.

Ensemble correlation PIV was used to obtain particle displacement PDF as well as particle recirculation probability as discussed in section **3.D.1.**. An ensemble of 1500 correlation plans was employed for each set of process conditions.

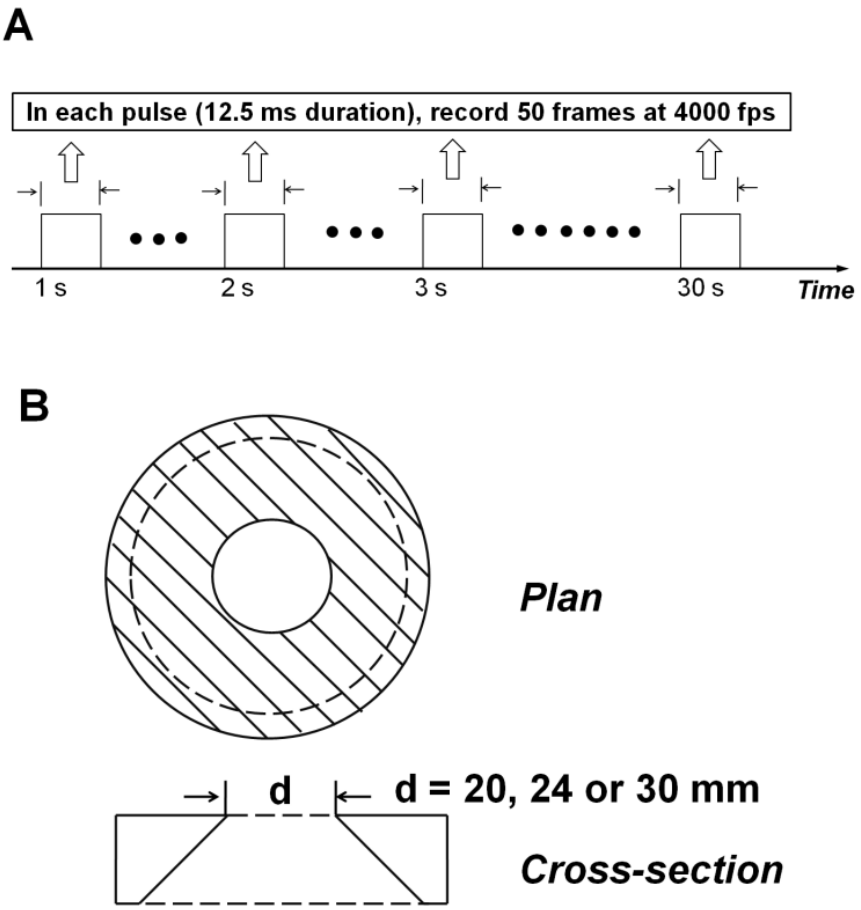

Figure 18. (A) Time sequence for high speed video imaging of particle motion in the partition column, (B) schematic diagram of AAI with diameter of *d* mm

Table 1. Process conditions for high speed video imaging of particle motion in the partition column of the Precision coater

Process parameters	**Values**
Air flow rate	90 m^3/h
Atomizing air pressure	2.0 bar
Air accelerator insert diameter	20, 24, 30 and 40 mm
Partition gap	10 mm
Particle size fraction	355-425, 500-600 and 710-850

3.D.2.3. Estimation of voidage within the partition column

The voidage, ε, within the partition column is estimated using the following equation:

$$\varepsilon = 1 - \frac{N_p V_p}{V_c} \tag{23}$$

where N_p is the number of particles on the image, which is also referred to as particle number below, V_p is the volume of a single particle and V_c is the total volume captured by the high speed camera. In this investigation, V_p was estimated using the mean pellet diameter, which was 780 μm; V_c was approximately 1.5 cm^3. The particles on the image were determined by applying morphological image processing steps as shown in Figure 19.

A disk shaped structuring element of 2-pixel diameter was used in the morphological opening operation and the disk shaped structuring element was approximated by a sequence of 4 periodic lines (Jones, 1996). The threshold of gray-scale image was obtained by using Otsu's method (Otsu, 1979). Due to the morphological opening operation, the local maxima were larger than 2 pixels in diameter. In the border clearance operation, the objects lying on the image border are removed. In the reconstruction operation, the black-and-white image after thresholding was used as the mask image and the local maxima image was used as the marker. The reconstruction results consist of bright objects, which correspond to particles within the image border. The subsequent labelling operation assigned each object an integer and the total number of integers corresponded to the number of particles on the image. Image processing operations in Figure 19 were carried out using the built-in functions in the Matlab image processing toolbox.

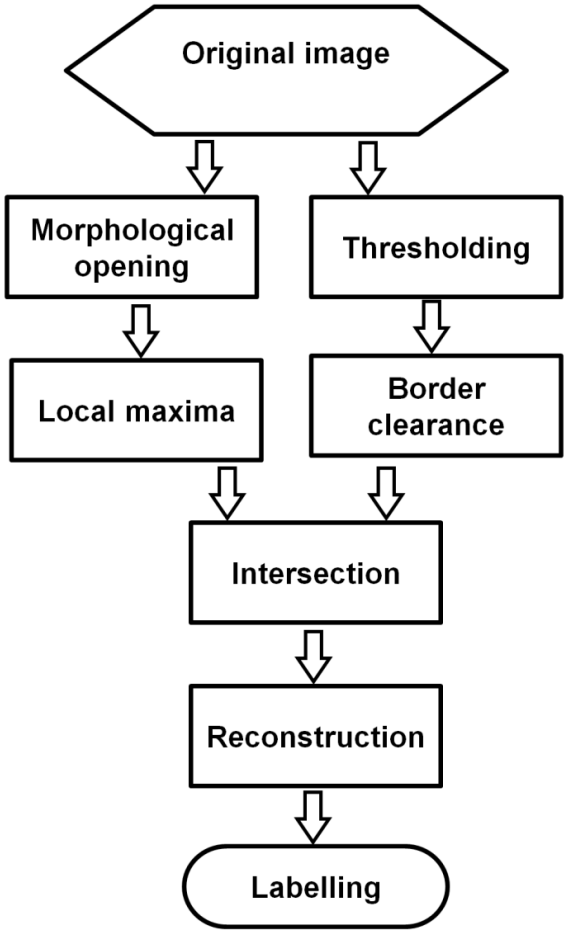

Figure 19. Flow chart depicting different steps in obtaining the number of particles on the image

3.D.2.4. Air velocity measurement

A Pitot tube (160-12, Dwyer Instruments, Australia) linked to a manometer (DP-8705, TSI, USA) was used to measure air velocities in the partition column. Air velocity was measured at 0, 0.5, 1.5 cm away from the centre of the partition column respectively (Figure 20). The AAIs were kept the same as in the high speed video imaging experiments and the partition gap was kept at 10 mm. Twenty measurements were taken and averaged for each set of process conditions.

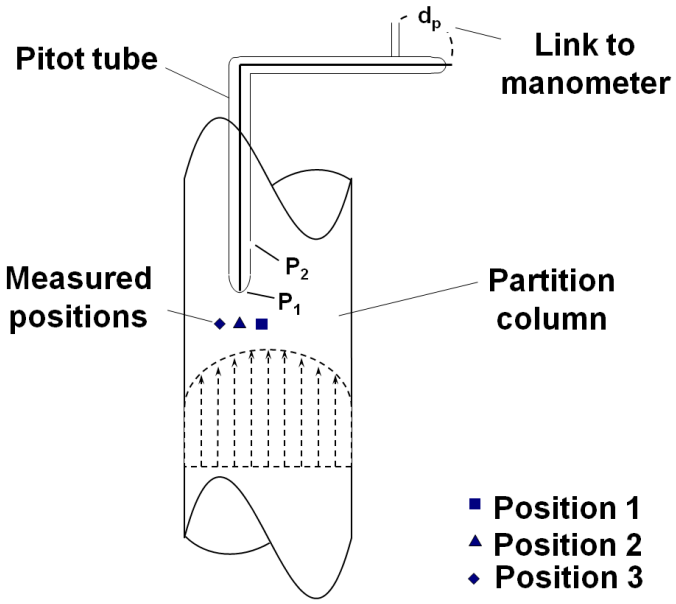

Figure 20. Schematic diagram of air velocity measurement within the partition column of the Precision coater

3.D.2.5. Single particle terminal velocity calculation

The drag force (F_D) of a spherical particle moving in air stream can be expressed as (Dallavalle, 1948; Young *et al.*, 2004):

$$F_D = C_D \frac{\pi d_p^2}{4} \frac{\rho_f v_s^2}{2} \tag{24}$$

where

$$C_D = \frac{24}{Re}[1 + Re^{0.687}] + \frac{0.42}{1+4.25Re^{-1.16}} \tag{25}$$

where

$$Re = \frac{\rho_f D_e v_s}{\mu_f} \tag{26}$$

where C_D is the drag coefficient of a single particle, d_p is the particle diameter, ρ_f is fluid density, v_s is the relative velocity between particle and fluid, Re is the Reynolds number, D_e is the diameter of partition column, μ_f is the kinematic viscosity of fluid.

The terminal velocity of a single particle is the minimal air velocity to balance the gravitational force to suspend a single particle. Hence, terminal velocity of a single particle equals the minimal v_s balancing gravitational force. The terminal velocity was calculated by solving the following equation for v_s:

$$C_D \frac{\pi d_p^2}{4} \frac{\rho_f v_s^2}{2} = mg \quad (27)$$

where mg is the gravitational force acting on a single particle.

The boundary layer thickness of the air stream within the partition column (δ_b) can be estimated using the following empirical equation (Zhang *et al.*, 1995):

$$\delta_b = 0.05 D_e^{0.74} \quad (28)$$

where D_e is the diameter of the partition column.

3.D.2.6. Assessment of the extent of spray drying effect during coating

Sugar pellets of three size fractions were coated to 5% weight gain level using HPMC according to the process conditions listed in Table 2. Triplicate batches were coated for each of the three particle size fractions. A load of 1 kg was used and the coated pellets were carefully collected and weighted after coating. The extent of spray drying effect (κ), i.e. percentage of coating material lost during the coating process, is defined as:

$$\kappa = \frac{m_f}{m_i + m_c} \quad (29)$$

where m_f is the final particle weight after coating, m_i is the initial particle weight before coating, and m_c is the weight of dry coat material applied to the particles.

Table 2. Process conditions for determining the extent of spray drying effect

Process parameters	Values
Air flow rate	90 m^3/h
Atomizing air pressure	2.0 bar
Air accelerator insert diameter	24 mm
Partition gap	10 mm
Particle size fraction	355-425, 500-600 and 710-850 µm
Spray rate	6.3 g/min

3.D.3. Development of visiometric process analyzer for particle mass flow rate measurement in the fountain region

A load of 1 kg HPMC base-coated pellets were loaded into the product chamber of the Precision coater. The downward particle movement within a 1.5 cm by 1.5 cm area between the product chamber and partition column was captured using a high speed video camera (Figure 21). The high speed camera was programmed and controlled using Matlab such that the camera took 50 video clips in a 2 Hz pulsed mode for each set of process conditions. Each video clip consists of 50 frames of images, which were taken at a recording speed of 4000 fps. The image size was 248 pixels by 248 pixels.

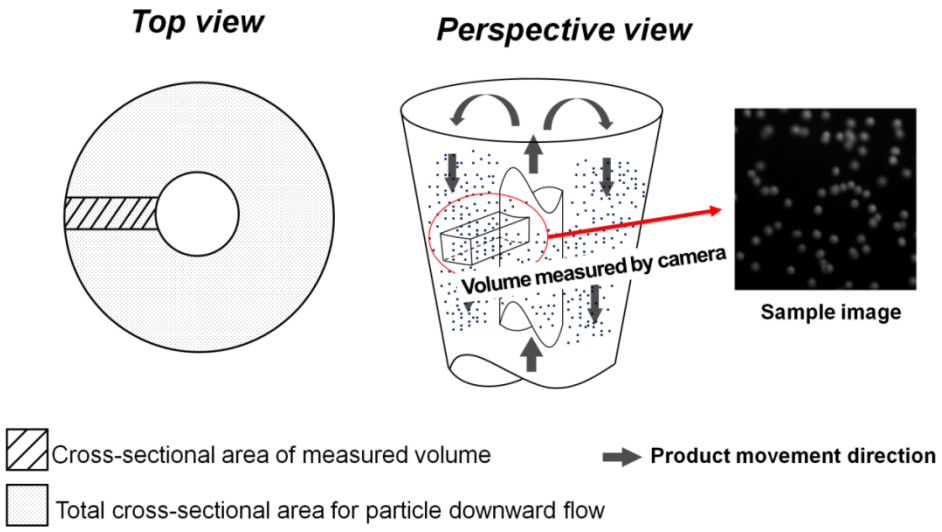

Figure 21. Schematic diagram showing the volume captured by the high speed camera for MFR measurement

In order to obtain particle velocity information, the MQD method was selected to conduct PIV analysis and sub-image was set as 64 pixels by 64 pixels with an overlapping ratio of 0.5. In order to count the number of particles, N_p, in the high speed image, the morphological image processing method developed in section **3.D.2.3.** was employed.

With the information of particle number and velocity information, the particle *MFR* was calculated using the following equation:

$$MFR = \frac{\bar{v} \times N \times V_p \times \rho}{L} \times \frac{S_t}{S_m} \quad (30)$$

where $\bar{v}$ is the average velocity obtained from PIV results, N_p is the number of particle on the image, which was obtained using morphological image processing, V_p and ρ are the mean volume and density of particles respectively, L is the height of the captured area along the vertical direction, S_t and S_m are the total and measured cross-sectional area respectively (Figure 20).

In order to investigate the roles of AAI diameter and partition gap on particle MFR, combinations of process conditions were employed and listed in Table 3.

Table 3. Process parameters for MFR measurement

Measurement	**Air flow rate (m^3/h)**	**Atomizing air pressure (bar)**	**Partition gap (mm)**	**AAI diameter (mm)**
A*	80, 90, 100, 110, 120	2.0	5, 10, 15, 20, 25	24
B*	90	1.0, 1.5, 2.0, 2.5, 3.0	10	20, 24, 30, 40

A* process parameters for mapping the influence of air flow rate and partition gap on particle MFR
B* process parameters for mapping the influence of atomizing air pressure and AAI diameter on particle MFR

3.D.4. Influence of annular bed flow patterns on coat uniformity

3.D.4.1. Production of seed pellets for high speed video imaging

Sugar pellets (710-850 μm size fraction) were used as the model particles. Red-colour seed particles were produced by coating sugar pellets to 2 % weight gain using 10 % w/w red pigmented aqueous suspension (Opadry II, Colorcon, USA). White-coloured seed particles were produced by coating sugar pellets to 2 % weight gain using 10 % w/w HPMC solution. A binary mix of white (0.5 kg) and red (1.5 kg) seed particles were used for subsequent high speed video imaging.

3.D.4.2. Development of visiometric process analyzer for annular bed detection

A load of 2 kg binary mix seed particles were introduced into the transparent acrylic product chamber of the Precison coater. The process parameters employed are listed in Table 4. AAIs of 20 mm (AAI-20), 24 mm (AAI-24) and 30 mm (AAI-30) diameters were selected for use to modulate air flow though the annular bed. Image recording of the annular bed was carried out using a high speed video camera. Recording speed used was 200 fps. Image size was set at 1024 pixels by 1280 pixels and a total number of 1000 frames was captured for each AAI used.

Table 4. Process conditions for high speed video imaging and colour coating

Process Parameters	Settings
Air flow rate	100 m^3/h
Inlet air temperature	70°C
Atomizing air pressure	2.0 bar
Partition gap	10 mm

MQD method was employed using Matlab to perform PIV analysis. Post-processing of PIV results included generating streamlines for a clear picture of flow orientations using Matlab. The streamlines $s(x, y)$ are defined as curves that satisfy $d_x/v_x = d_y/v_y$, where v_x and v_y are the detected velocities along *X* and *Y* directions; d_x and d_y are the curve derivatives along *X* and *Y* directions, respectively (Nakayama and Boucher, 1999). Streamlines are curves that are instantaneously parallel to the velocity vectors produced by PIV.

3.D.4.3. Measurement of particle recirculation probability within the partition column

As particle recirculation within the partition column was considered as a major factor affecting coat uniformity and the influences of AAIs on particle recirculation probability is not known, the particle recirculation probabilities of the three AAIs had to be checked before correlating annular bed flow pattern with coat uniformity. Fifty video clips of particle movement within the partition column were taken at a recording speed of 4000 fps. The recirculation probabilities were derived from video clips using the visiometric process analyzer developed in section **D.1.** earlier in this chapter. One-way ANOVA was then performed on the recirculation probabilities of the three AAI settings using Matlab.

3.D.4.4. Characterization of coating performance using colour coating and tristimulus colourimetry

3.D.4.4.1. Colour coating

Colour coating and subsequent tristimulus colourimetry of in-process samples were used to assess coating performance under different annular bed flow

patterns. Pellets were base-coated to 2 % weight gain using 10 % w/w HPMC in the Precision coater. A load of 2 kg base-coated particles was further colour-coated to 2 % weight gain using a 10 % w/w Opadry II. Process parameters used were the same as those employed during the high speed video imaging and spray rate was 10 g/min. Five in-process samples were taken for each 0.4 % weight gain and triplicate batches were colour-coated for each AAI setup.

3.D.4.4.2. Tristimulus colourimetry and statistical analysis of colour variance of in-process samples

Tristimulus colourimetry has been used to judge the appearance of colour-coated tablets (Wirth, 1991; Cole, 1995) as well as to estimate the coat uniformity of colour-coated pellets (Chan *et al.*, 2001). For the purpose of coat uniformity determination, the colour intensity of spots on the particle surface is quantified in defined colour spaces. The colour difference (*dE*) between colour-coated and white base-coated particles indicates the colour intensity change on the particle surfaces, thus reflecting the amount of colour pigment deposited on the particle surfaces. Hence, the variance of *dE* corresponds to the colour variance of the sampled colour-coated particles, and may be used as an inverse indicator of particle coat uniformity. For example, *F-test* has been used to compare the *dE* variances of two sets of sampled colour-coated particles for the purpose of comparing coat uniformity of particles coated using different types of coaters (Heng *et al.*, 2006). Relative colour variation (*RCV*), which is defined as the ratio of the standard deviation of *dE* to the mean of *dE*, expresses colour variation relative to the magnitude of *dE* measurements. Hence, as used in the literature, *RCV* was preferably

chosen for plotting the changes in relative colour variation with increased weight gains (Chan *et al.*, 2001).

Mathematically, under Commission Internationale de l'Eclairage (CIE) 1976 (L*, a*, b*) colour space, *dE* between white (L_u, a_u, b_u) and colour-coated particles (L_c, a_c, b_c) is calculated using Euclidean distance:

$$dE = \sqrt{(L_u - L_c)^2 + (a_u - a_c)^2 + (b_u - b_c)^2} \quad (31)$$

The mean colour difference of *n* measured particles, $\overline{dE}$, is expressed as:

$$\overline{dE} = \frac{1}{n}\sum_{i=1}^{n} dE_i \quad (32)$$

where dE_i is the colour difference of the i^{th} measured particle.

RCV of *n* measured particles is expressed as:

$$RCV = \frac{\sqrt{\frac{\sum_{i=1}^{n}(dE_i - \overline{dE})^2}{n-1}}}{\overline{dE}} \times 100\% \quad (33)$$

A tristimulus colourimeter (Chroma Meter CR-241, Minolta, Japan) with CIE standard illumination D_{65} was used to measure the colour intensity of colour-coated particles. For each sample, 200 particles were measured by determining the colour intensity of a 0.3 mm diameter spot on the surface of each particle. $\overline{dE}$ was calculated after pooling *dE* measurements from triplicate batches (200 measurements for each sample per batch; hence, 600 measurements in total for each data point). The *RCV* of each batch was calculated separately. Consequently, for each weight gain, three *RCV* values were obtained from the triplicate batches for determination of mean *RCV* and inter-batch standard deviation of *RCV*. $\overline{dE}$ and mean *RCV* plots were used to show the trends of

inter-particle mean colour difference and inter-batch relative colour variation respectively with increased weight gains.

Two-sample *F-test* on variance using Matlab was performed to compare colour variances of sample particles coated under different AAI settings. *F-test* rather than *t-test* was chosen in order to test the variance of *dE*. The null hypothesis of a two-sample *F-test* is that the two samples come from normal distribution with the same variance. *dE* values pooled from triplicate batches (600 *dE* values in total) were used in *F-test*, thus taking into account both inter-batch and inter-particle colour variance.

CHAPTER 4. RESULTS AND DISCUSSION

CHAPTER 4. RESULTS AND DISCUSSION

In the production of multiparticulate dosage forms, the spheronization step in extrusion-spheronization has not been well studied although it is responsible for determining the mean size as well as the size distribution. It is of interest to elucidate the kinetics of particle growth as well as the feasibility of using a visiometric approach to monitor the particle growth. In bottom spray fluid bed coating, particle motion within the upbed region, fountain region and annular bed region need to be quantified. Moreover, the mechanism of particle recirculation within the partition column and the influence of annular bed flow patterns on coat uniformity can be better understood with the developed visiometric process analyzer.

4.A. Particle growth kinetics in the spheronization process

The first objective in the investigation on spheronization was to verify and determine particle growth kinetics. High speed video imaging coupled with Ferret diameter measurement were used as the method for particle size determination. The verification of this particle sizing method and an improvement of the model for particle growth kinetics were discussed below.

4.A.1. Verification of Ferret diameter measurement technique for particle size distribution determination

High speed video imaging coupled with Ferret diameter measurement of particle size were verified by synchronized in-process sampling and subsequent microscopic measurement of Ferret mean diameter. The microscopic measurement of the Ferret mean diameter and the Ferret diameter

determination of particles on high speed video images were shown in Figures 22A and 22B respectively.

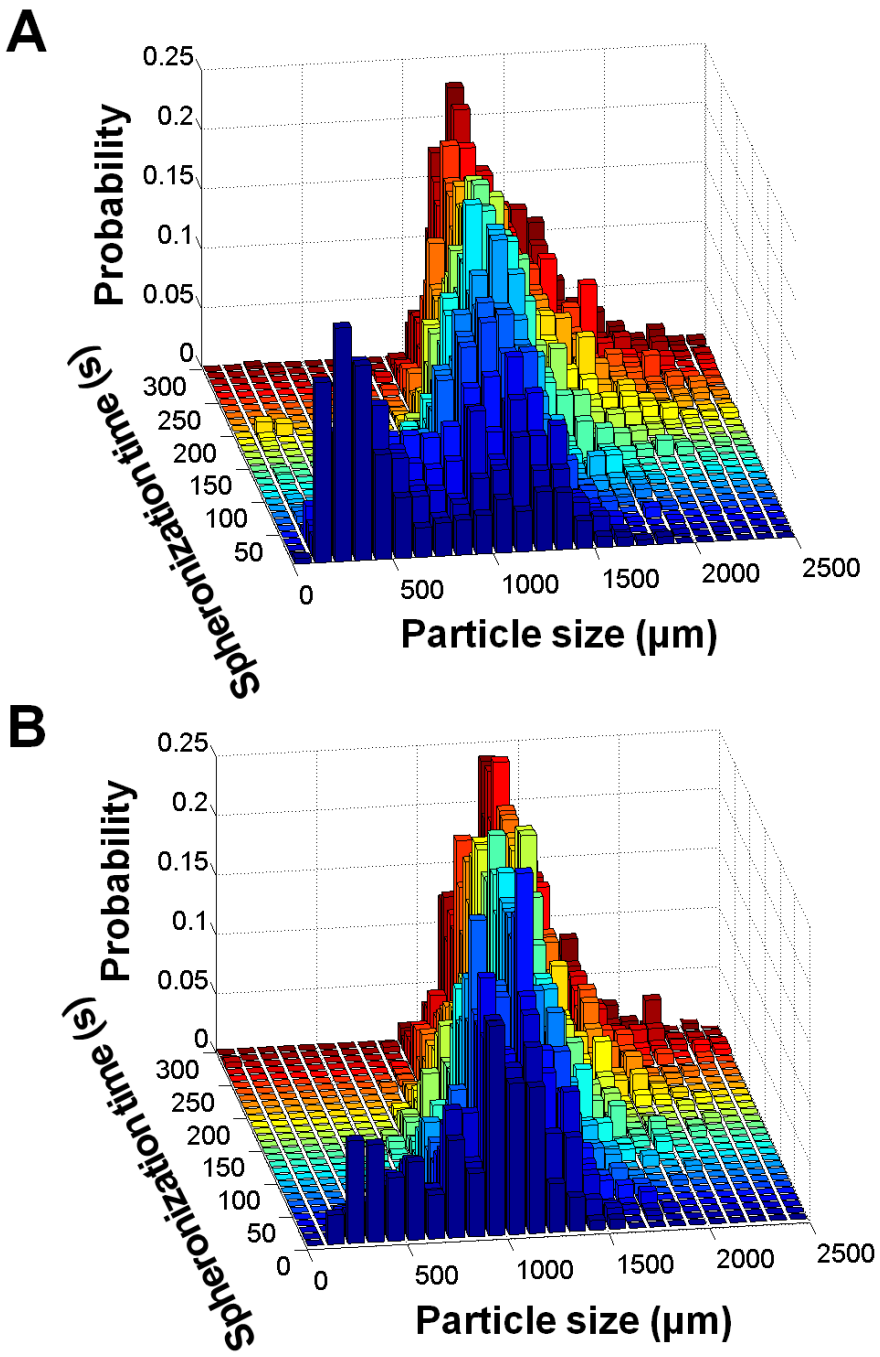

Figure 22. Particle size distributions measured using (A) optical microscope and Ferret mean diameter and (B) high speed imaging and Ferret diameter determination

The overall trends of the two measurement techniques were similar and the *RMSE* between the two measurement techniques was 0.0291. However, compared with static microscopic measurements of the Ferret mean diameter, high speed imaging coupled with Ferret diameter determination was less discriminating in determining particle size distribution when particle sizes were below 500 μm (Figure 22B). This may be explained as follows; for a fixed volume of particles, to determine size distribution, by in-process sampling and subsequent microscopic measurement, the particles were examined as a single layer under the optical microscope, thus ensuring that each and every particle had the same opportunity to be measured. However, with high speed images of in-process particles, the number of fine particles tended to be underestimated as finer particles may be shielded by the larger particles, especially when particle sizes were not uniform as in the presence of a bimodal size distribution. Nevertheless, for particle sizing of in-process samples, high speed imaging coupled with Ferret diameter measurement was still employed for monitoring the changes in particle size during the spheronization process due to the following reasons. Firstly, for particles that were larger than 500 μm, high speed imaging coupled with Ferret diameter measurement gave a relatively accurate measure and for most process conditions employed in this investigation, the mean particle sizes were generally much larger than 500 μm. Secondly, one of the objectives of this investigation was to compare the influences of process conditions on the particle growth kinetics. Hence, the information from high speed imaging and Ferret diameter measurement can be reliably used.

4.A.2. Refined model for particle growth kinetics

There are currently three theories on particle growth kinetics. Rowe*'s* theory was based on the formation of "dumb-bells" and subsequent deformation of "dumb-bells" into pellets. By using plasticine, Baert *et al.* proposed that pellets were formed from the breakage of "dumb-bells". However, according to the remodelling theory proposed by Liew *et al*., the extrudates were broken down into large particles and fines, and particles grew by layering of fines onto the larger particles.

In order to verify the theories above, changes in particle size distribution during the spheronization process with respect to different water concentrations and spheronizer plate peripheral speed were determined (Figure 23). In the initial stage of spheronization (5-15 s), bimodal size distributions were present for most of the runs under various spheronization conditions. It was observed that the bimodal distributions were subsequently transformed into unimodal size distributions by elimination of the mode in the smaller size range. This finding suggests that extrudates break down into coarse particles and fines and the particles grow by layering of fines onto coarse particles. In Rowe's theory, the "dumb-bells" were deformed into pellets, thus suggesting a limited change in particle size distributions. However, apparent changes in the particle size distributions were observed during spheronization process. In Baert *et al.*'s theory, the breakage of "dumb-bells" into pellets should result in a monotonous decrease in particle size. However, particle sizes were found to increase with spheronization time. Nevertheless, Liew *et al.*'s remodelling theory was found to be strongly supported by the observed transformation in particle size distribution, i.e. from uniform extrudates to bimodal and then

from bimodal to unimodal distributions, which corresponded well with the breakage of extrudates and subsequent remodelling into larger particles.

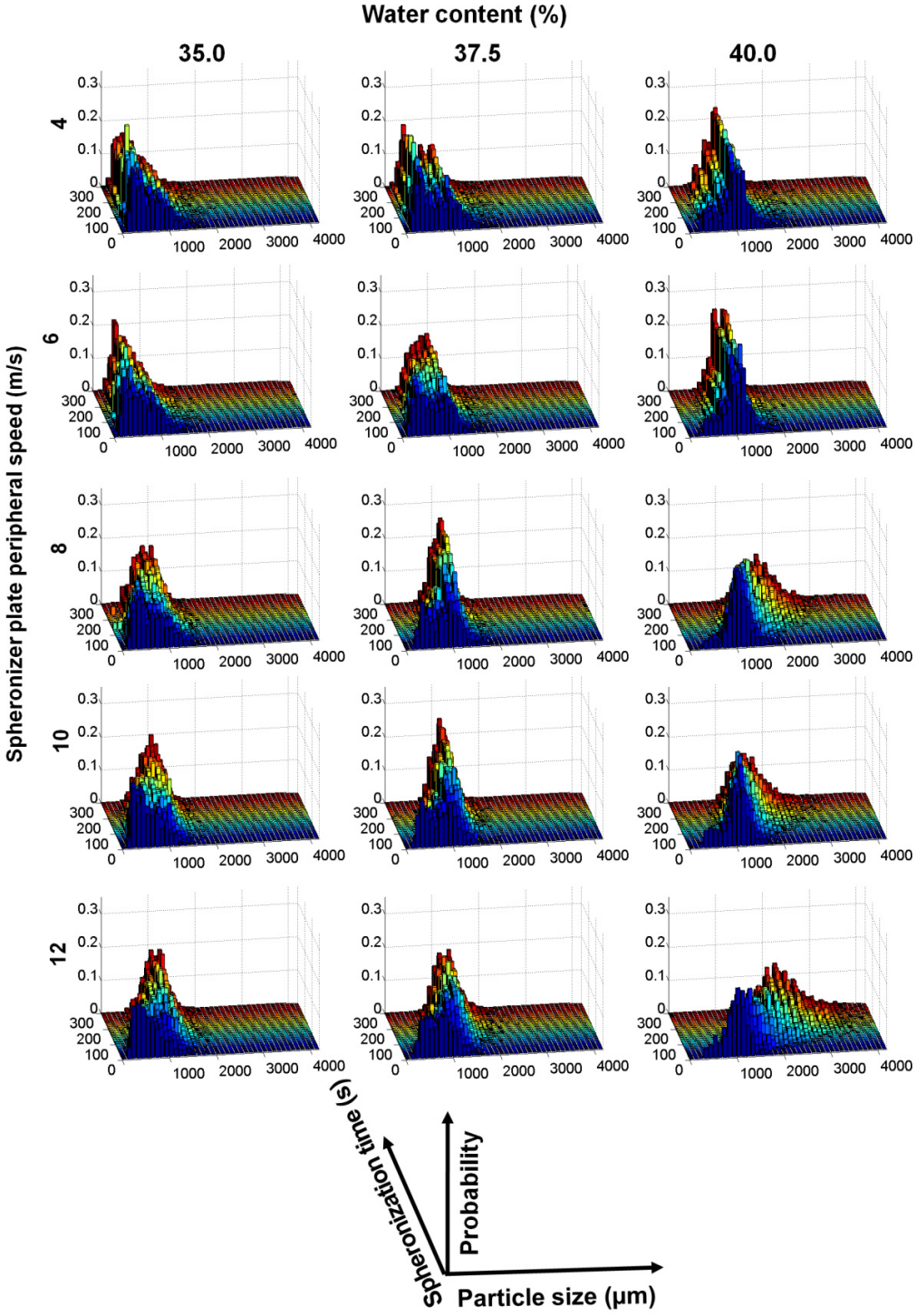

Figure 23. Changes in particle size distributions during spheronization

Moreover, it was observed that the amount of fine particles was greater under higher spheronizer plate peripheral speed and lower water content conditions. This could be attributed to the lower plasticity of extrudates caused by lower water content and higher kinetic energy transferred from the frictional base plate rotating at a high speed, resulting in larger amounts of fines in the initial stage.

In conditions with sufficiently high spheronizer plate peripheral speed and extrudates of adequate plasticity, the mean particle size may significantly exceed the extruder screen diameter (1 mm). However, the excessive particle growth was not adequately considered by the current remodelling theory, which assumed that particle growth stagnated after layering of all the fines on larger particles. Hence, the current remodelling theory has to be refined to better reflect the particle growth kinetics during spheronization.

The current remodelling theory was refined by the present study to better reflect particle growth kinetics in the spheronization process. Particle growth kinetics was divided into three phases (Figure 24A). In phase I, i.e. the breakage phase, the extrudates were broken down into coarse particles and fine particles. The ratio of coarse particles and fines was influenced by the spheronizer plate peripheral speed and extrudate plasticity. Higher spheronizer plate peripheral speed and lower extrudate plasticity yielded more fines and vice versa. Evidence of the nature of the broken down extrudates was demonstrated by the bimodal particle size distributions seen in the first 20 s of the spheronization process (Figure 23). In phase II, i.e. the layering phase, coarse particles grew by layering of fine particles onto their surfaces.

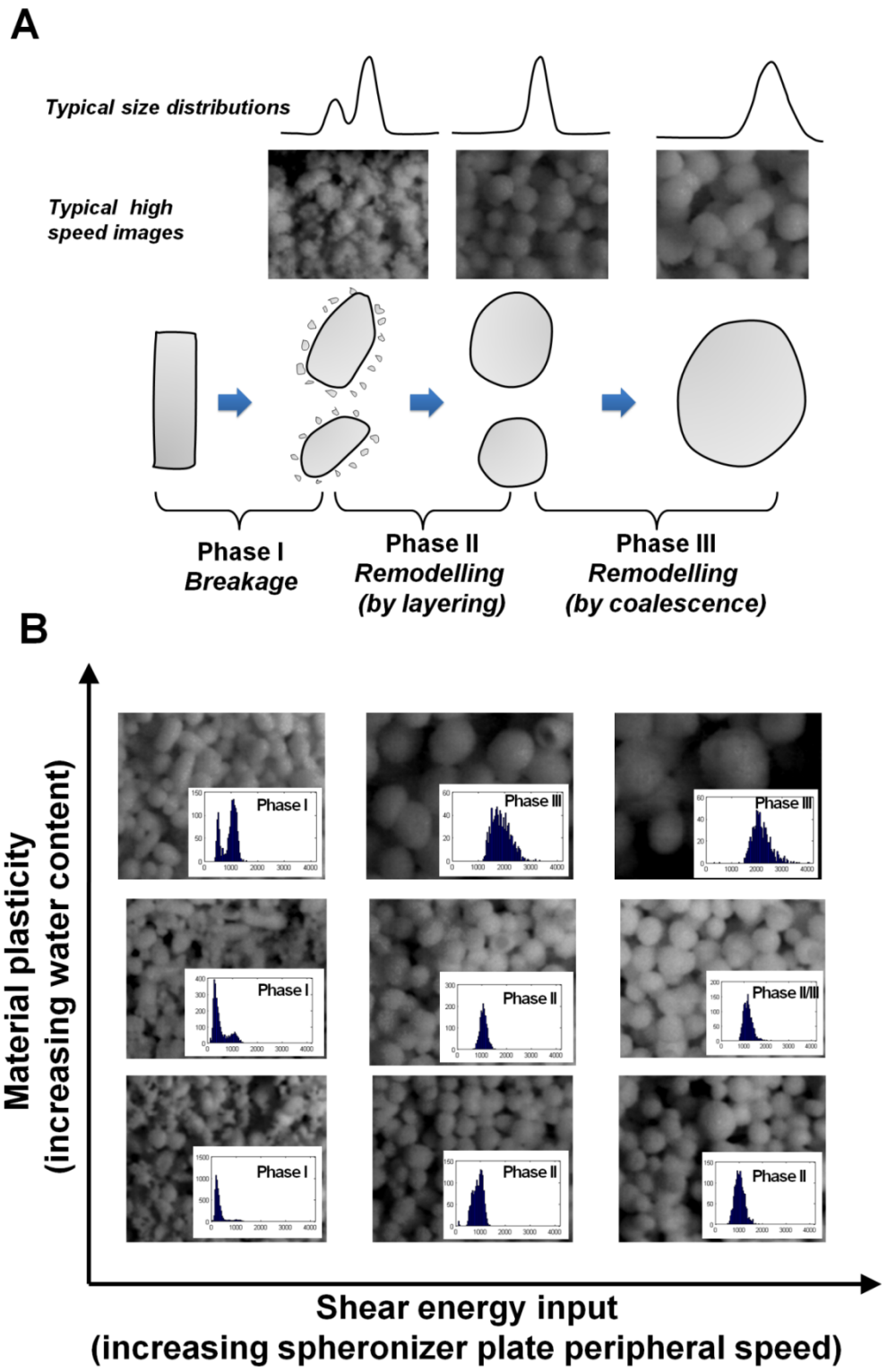

Figure 24. Schematic diagrams of (A) refined particle growth kinetics and (B) the influences of shear energy input and material plasticity on particle growth kinetics

As the size of coarse particles produced from phase I was approximately the diameter of the extruder screen, the mean particle size after phase II may also be comparable to the screen diameter. Under conditions of sufficient spheronization speed, e.g. $V_{peri} \geq 8$ m/s, and extrudate plasticity, e.g. $W_{content} \geq 37.5\%$, it is clearly shown in Figure 22 that the bimodal distributions were transformed into unimodal distributions. The regression of the smaller size mode and the gradual increase in the large size mode strongly supported the occurrence of particle layering. However, for low spheronizer plate peripheral speed conditions, e.g. $V_{peri} \leq 6$ m/s, and low extrudate plasticity conditions, e.g. $W_{content} < 37.5\%$, phase II particle growth may not occur and the particle size distributions remained unchanged with time. This may be due to insufficient energy transferred from the frictional base plate. Given adequate plasticity, e.g. $W_{content} > 37.5\%$, spheronization speed, e.g. $V_{peri} > 10$ m/s, and sufficient spheronization time, phase III particle growth, i.e. the coalescence growth phase, may occur. In phase III, coalescence due to inelastic collision was the main mechanism for particle growth. Significant widening of the particle size distribution was observed and a rather quick increase in particle size was the major characteristics of phase III growth.

A schematic representation of the influences of material plasticity and shear energy input on pellets produced is shown in Figure 24B, as well as their size distributions. Combinations of three water contents, i.e. 35.0 %, 37.5 % and 40.0 %, and three spheronizer plate peripheral speeds, i.e. 4 m/s, 8 m/s and 12 m/s, were plotted respectively. It was clearly shown that the extent and speed of particle growth was a function of shear energy input and material plasticity.

Generally, higher shear energy and higher material plasticity are required for particles to grow into the more advanced growth phases. Moreover, combining particle growth kinetics shown in Figure 23, it was obvious that higher shear energy and higher material plasticity had also promoted faster particle growth. Hence, it is important to timely reduce shear energy input below the minimal level as soon as phase II growth is completed. The turned down spheronizer plate peripheral speed may then continue to promote the rounding of particles into spheroids while avoiding excessive particle growth.

4.B. Relationship between particle motion in the near plate region and particle growth kinetics

The second objective of investigation on the spheronization process was to investigate the relationship between particle motion in the near plate region and particle growth kinetics. PIV analysis was performed on high speed images of the particles in the near plate region. The dimensionless surface plots of total mean speed and total granular temperature were then used to visualize and investigate the relationship.

4.B.1. "Dual kinetic zones" particle flow structure in the near plate region

Gravitational force, interparticulate frictional forces, centripetal force, particle-particle and particle-plate impact forces, pressure and normal force are the forces that are likely to act on a particle in the spheronization process. However, due to the complex particle-particle and particle-plate interactions, the particle motion in the near plate region, the periphery region just above the frictional base plate, is still unclear.

Sample high speed images of particle movement in the near plate region were mapped by the superimposition of velocity vectors detected from PIV analysis (Figure 25). This clearly helped to depict conditions of particle motion and voidage in the near plate region. Two distinct kinetic zones, fluidization zone and frictional motion zone, could be identified. Fluidization zone was a thin kinetic zone located just above the frictional base plate, and frictional motion zone was the bulk zone above the fluidization zone. The fluidization zone is usually of a thickness of a few times that of the mean particle diameter. Under the fast shear conditions, particles in the fluidization zone were found to exist in a high voidage state and to move at much higher speeds compared to particles in the frictional motion zone. For the first time, the high speed video images clearly showed that a "dual kinetic zones" particle flow structure exist in the near plate region during spheronization. The high speed motion and large voidage state of the base particles may be inferred to be due to intensive particle-plate or particle-particle collisions. Comparatively, in the frictional motion zone, particles were found to pack more closely together and reflected their movement at lower but uniform velocities. This was brought about as the energy transferred from the frictional base plate was rapidly dissipated by inelastic collisions in the fluidization zone and hence, for particles farther from the plate, solids flow was dominated largely by the frictional forces between particles.

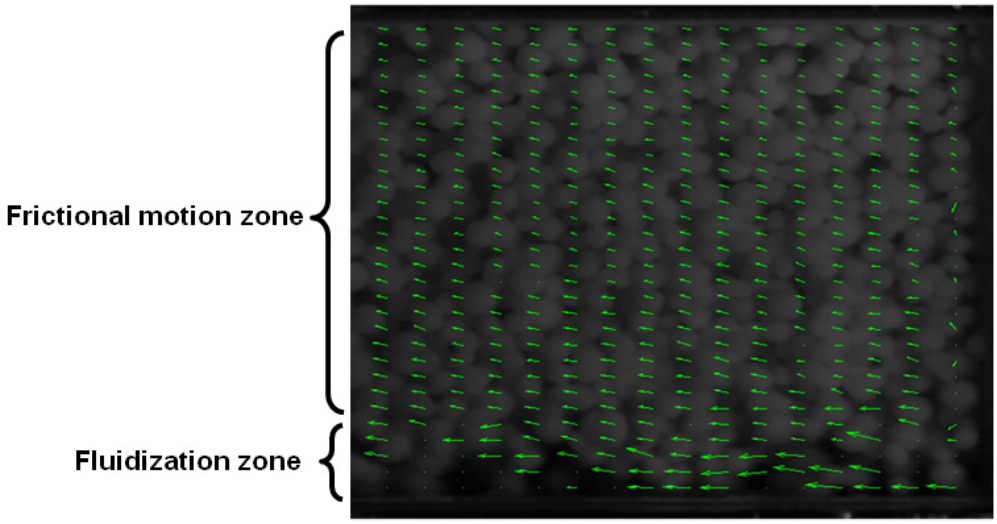

Figure 25. Sample high speed image of particle movement in the near plate region showing the "dual kinetic zones" particle flow structure

4.B.2. Relationship between mean speed profile in the near plate region and particle growth kinetics

As mentioned in section **3.C.3.3.**, in order to investigate the relationship between the mean speed profile in the near plate region and particle growth kinetics, dimensionless surface plots were employed. In the dimensionless surface plot, the mean particle size at time t, mpz_t, was used as the base for expressing the vertical distance from the locations of mean speed to the frictional base plate. In the dimensionless plots in this investigation, the changes in mean particle sizes were reflected by the degree of compression along the distance axis; the higher the degree of compression along the distance axis, the smaller the mean particle size.

Two examples below are provided to explain the meaning of the dimensionless surface plots. For example, for mean speed of particles 10 mm above the frictional base plate, the dimensionless distance would be 10 or 5 if

the mean particle sizes were 1 mm or 2 mm respectively. Similarly, a second example is to consider the particles on the top of the images, i.e. 20 mm away from the frictional bases plate, their dimensionless distance to the frictional base plate would be 20 if the mean particle size was 1 mm. Sample dimensionless plots of particle mean speed and granular temperature are shown in Figure 26. The locations of the kinetic zones and initial drop in mean speed and initial surge in granular temperature were labelled in Figure 26A and 26B, respectively. The dimensionless distance corresponding to the end of the initial drop in mean speed and initial granular temperature surge were marked in Figure 26C and 26D respectively.

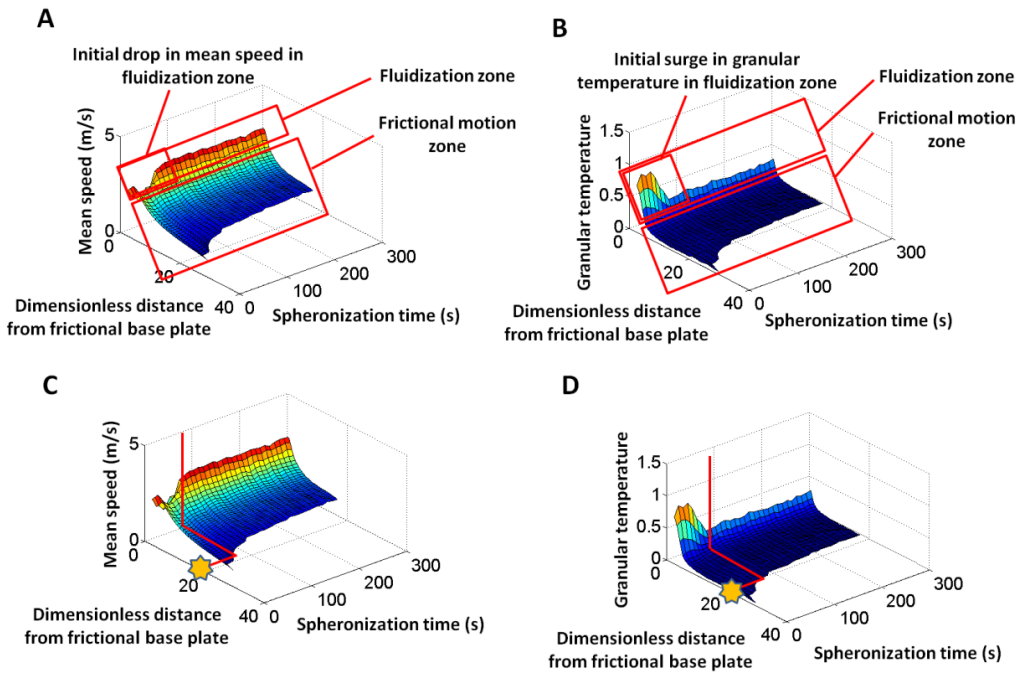

Figure 26. Sample dimensionless plots of (A) particle mean speed and (B) granular temperature showing the kinetic zones, and of the dimensionless distances corresponding to the end of (C) initial drop in mean speed and (D) the initial surge in granular temperature

The mean speeds obtained by averaging along the horizontal direction were plotted with respect to spheronization time and dimensionless distance from the frictional base plate (Figure 27). It was observed that the mean speed decayed rapidly with an increase in dimensionless distance from the frictional base plate. This finding was in accordance with the observation from high speed video images and the proposed "dual kinetic zones" particle flow structure. Again, this may be explained by the rapid energy loss during inelastic collisions between the particles in the fluidization zone. Moreover, for spheronizer plate peripheral speeds higher than 8 m/s, it was interesting to note that for mean speed profile in the fluidization zone, there was a short period during which a drop in mean speed was observed and the end time of the low speed period corresponded to the time when mean particle size of 1 mm, a maximum dimensionless distance of 20 as shown on Figure 27.

It is important to note that 1 mm mean particle diameter was the diameter of extruder screen and the endpoint of the spheronization process. The short speed decrease period in the initial stage may be attributed to the fines generated in the breakage phase (phase I). Fines sheared by the frictional base plate may have similar speeds but had considerably smaller momentum compared to sheared coarse particles. The smaller momentum carried by the fines produced much slower resultant speed after their collisions with the slower-moving coarser particles in the upper layer, thus resulting in the significant speed decrease in the initial stage.

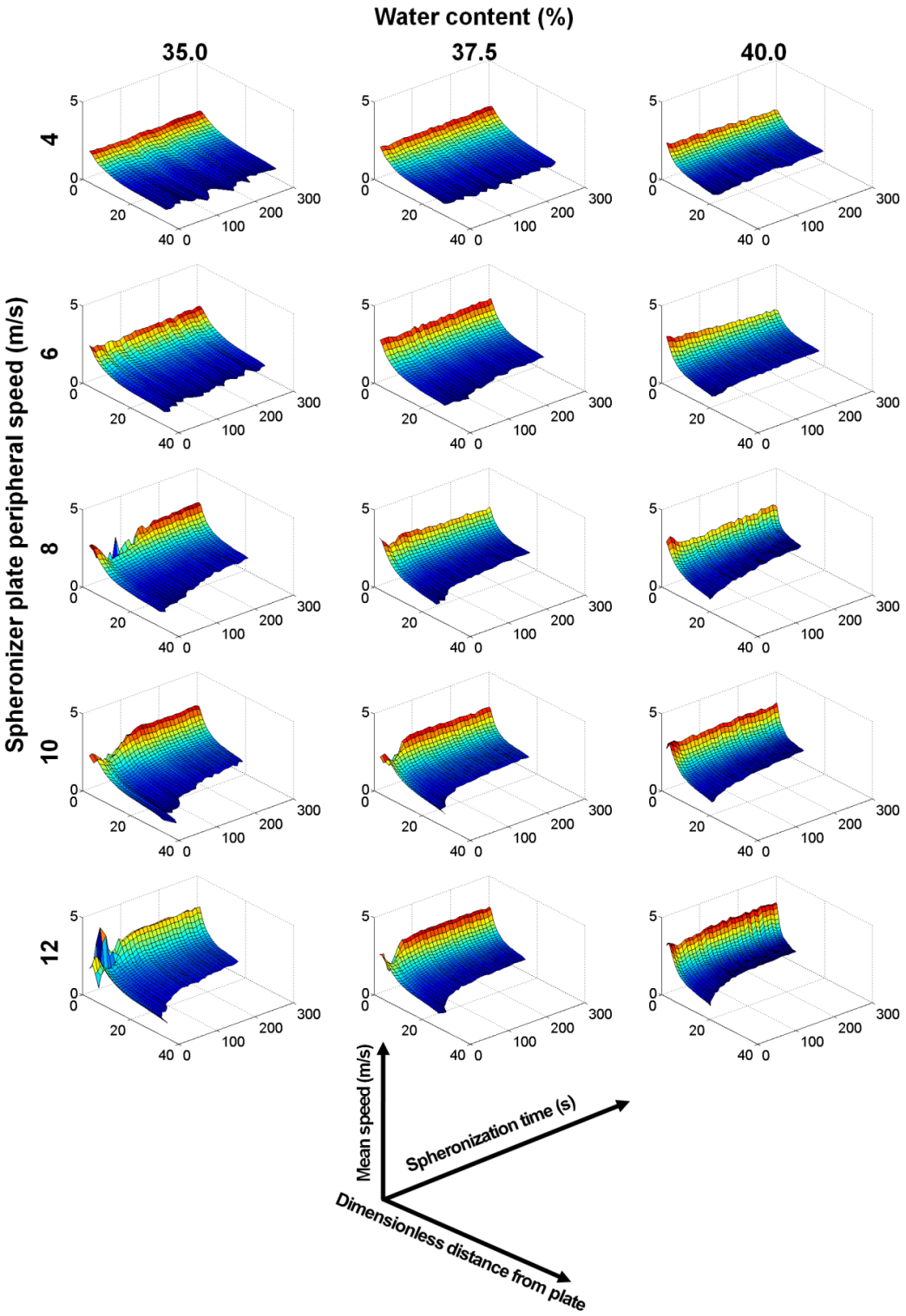

Figure 27. Changes in the mean speed profile in the near plate region with respect to spheronization time and dimensionless distance from the frictional base plate

With the deposition of the fines and their exhaustion, the fluidization zone was dominated mainly by the coarse-coarse particle collisions, which transfer shear energy more effectively, thus causing an increased speed in the later phase of spheronization. Hence, the end time of short period of speed decrease corresponded to the completion of phase II layering growth. This is supported by the coincidence of the end time of speed decrease and the time point when the mean particle size was approximately the diameter of the extruder screen (1 mm).

4.B.3. Relationship between mean granular temperature profile and particle growth kinetics in the near plate region

Similarly, changes in mean granular temperature profile were also plotted with respect to spheronization time and dimensionless distance from the frictional base plate bottom (Figure 28). Compared to the mean speed profile plot in Figure 26, the mean granular temperature profile focused more on the fluctuating energy rather than the mean energy. For instance, particles moving at distinctively different speeds would have higher granular temperature than particles with uniform speeds regardless of the actual speed values. Granular temperature could also be viewed as an index of speed heterogeneity. As expected, mean granular temperature was more informative than mean speed in reflecting the particle growth kinetics as high granular temperature in the fluidization zone generally corresponded to a rapid increase in mean particle size.

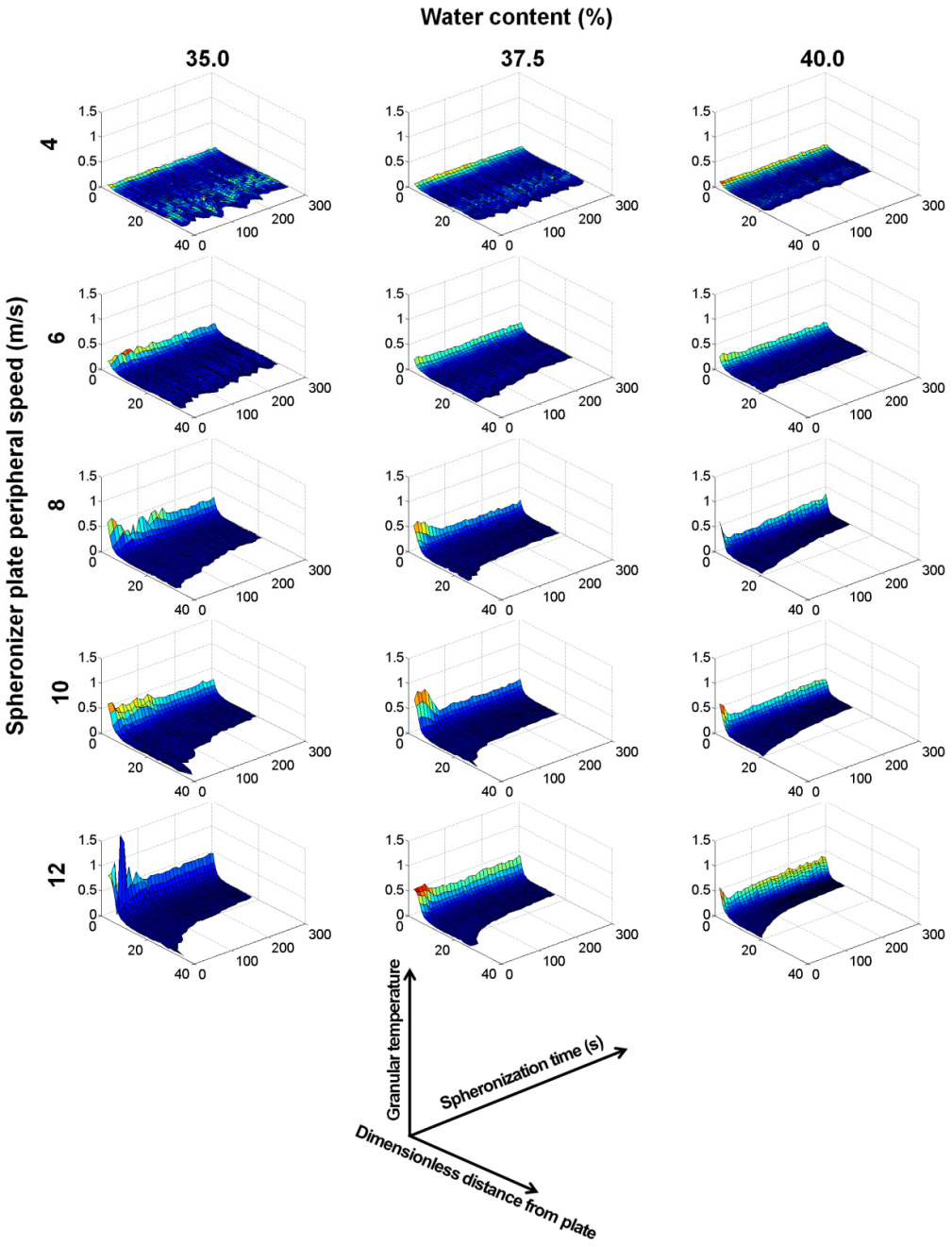

Figure 28. Changes in mean granular temperature profile in the near plate region with respect to spheronization time and dimensionless distance from the bottom of frictional base plate

Moreover, for spheronizer plate peripheral speed higher than 6 m/s, the mean granular temperature in the fluidization zone was found to be high in the initial stage and then decreased in the later stage. The initial surge in mean granular temperature may be explained by the layering of fines onto the coarse particles in phase II particle growth. Both fines and coarse particles were in direct contact with the frictional base plate and were strongly influenced by the shear forces provided by the frictional base plate. Coarse particles possessed higher momentum than fine particles. The differences in momentum carried by the particles were then transferred into broad distributions of speeds after their collisions with particles located in the adjacent layer that was not in direct contact with the frictional base plate. It was also observed that it took a longer time for less plastic extrudates to complete phase II growth. This was expected as it required higher energy to make less plastic particles to deform. Moreover, the mean granular temperature of less plastic particles was generally found to be higher under the same spheronizer plate peripheral speed. This may be due to the nature of less plastic particles, thus making the collisions more elastic, conserving more energy and resulting in a broader speed distribution. This point would be discussed in greater detail under section **4.B.4.**

Moreover, it was interesting to note that for the process conditions experienced during the initial surge in mean granular temperature, the end of mean granular temperature surge corresponded approximately to the time point when mean particle diameter was close to 1 mm, the aperture size of the extruder screen. The initial surge in mean granular temperature may be explained by the occurrence of phase II layering of fines, which involved

collisions between coarse and fine particles. Hence, like mean speed profile in the fluidization zone, mean granular temperature may also be a useful parameter for monitoring the spheronization process and for detecting the endpoint of phase II particle growth.

4.B.4. Particle speed distribution within the fluidization zone

Three rows of vectors nearest to the frictional bases plate were used for investigating the particle speed distribution within the fluidization zone. The speed distribution in the fluidization zone is shown in Figure 29. It was found that particle speed generally increased with increase in spheronizer plate peripheral speed. This may be attributed to the increased shear energy input with increased spheronizer plate peripheral speed. It was also observed that the spread of particle speed distribution increased with increase in spheronizer plate peripheral speed. This may be explained by more intense particle-particle and particle-plate collisions induced by higher shear energy input, resulting in a wider particle speed distribution in the fluidization zone. Moreover, it was interesting to note that for the process conditions involved in phase II particle layering, the particle speed distributions were bimodal in the initial stage of spheronization but were transformed into unimodal distributions with progression of the spheronization process. The bimodal speed distributions may be explained by the fines generated in the breakage phase.

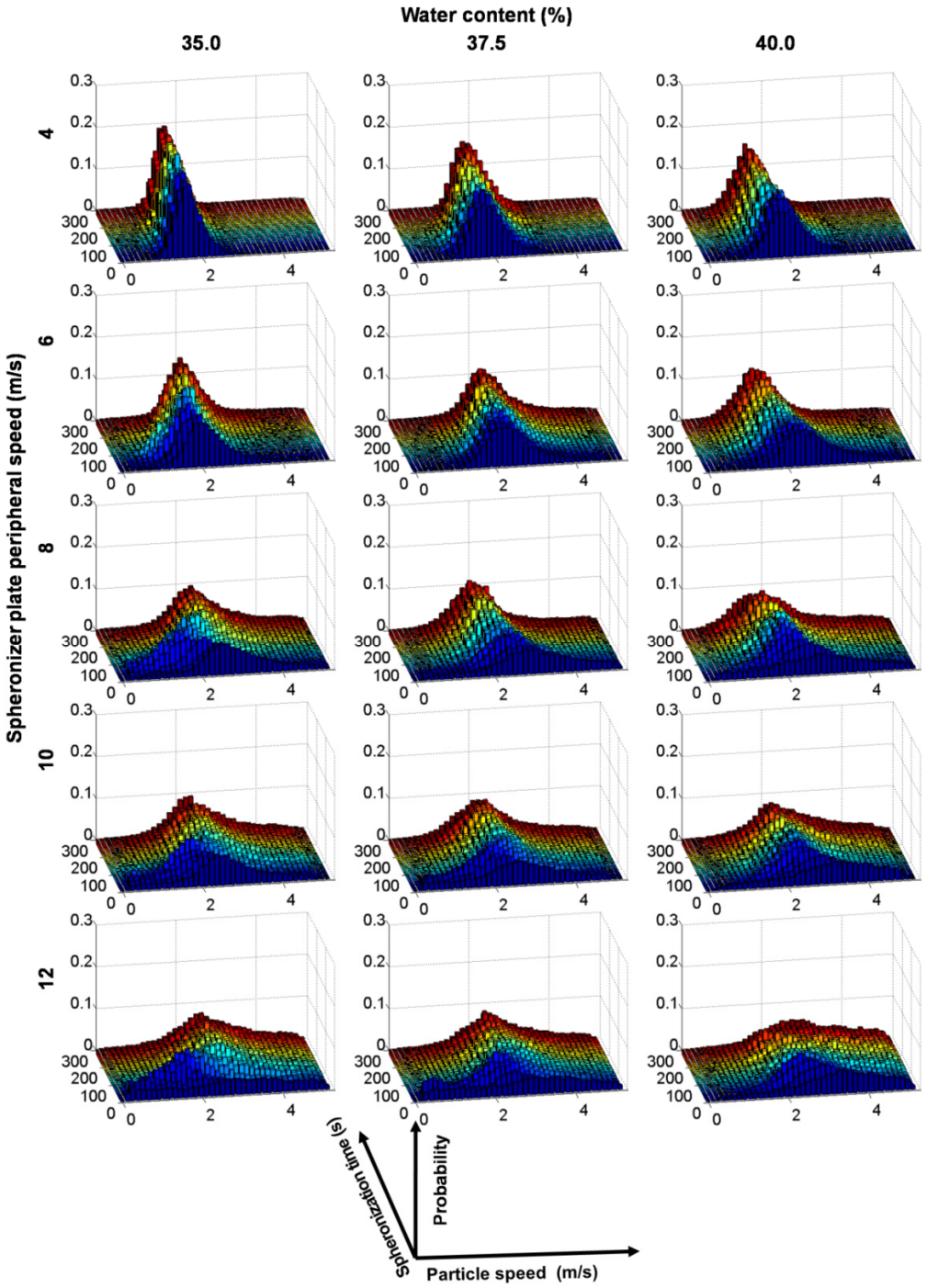

Figure 29. Particle speed distributions in the fluidization zone with spheronization time

In the spheronization process, shear energy was transferred from the rotating frictional base plate to particles by means of collisions between the plate and particles in the fluidization zone. In the case when fines were sheared, due to their small mass, less momentum was acquired after collision with the plate compared to coarse particles, thus resulting in a much lower velocity after the fines' collision with other particles above the fluidization zone (Figure 30A). On the contrary, coarse particles may acquire higher momentum after collision with the rotating frictional base plate, thus resulting in the higher speed in the fluidization zone after their collisions with other particles (Figure 30B). In phase I and phase II particle growth, particles in the fluidization zone comprised fines as well as coarse particles, thus resulting in a bimodal speed distribution in the fluidization zone. Similarly, the disappearance of the first mode in the speed distribution profile may be explained by the completion of phase II particle growth, which consumed fine particles by means of layering.

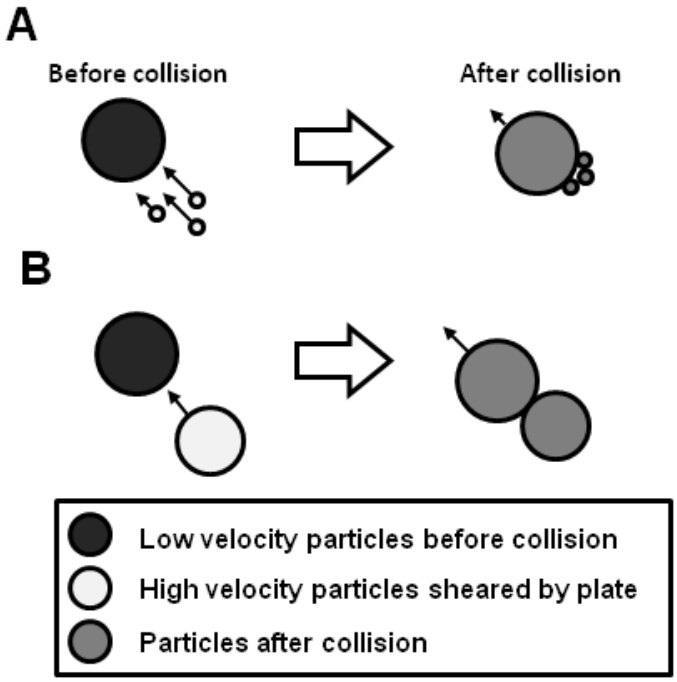

Figure 30. Schematic diagram of collisions between (A) coarse and fine particles and (B) coarse and coarse particles

The particle speed distributions of a typical spheronization condition (37.5% water content and 10 m/s spheronizer plate peripheral speed) were plotted in Figure 31. The speed distributions were shown as dots with the best fitted curves of Maxwell distribution and Gaussian distribution shown as dotted and solid lines, respectively. It could be clearly observed that the Maxwell distribution did not fit well with the experimental data of particle speed distribution compared to Gaussian distribution.

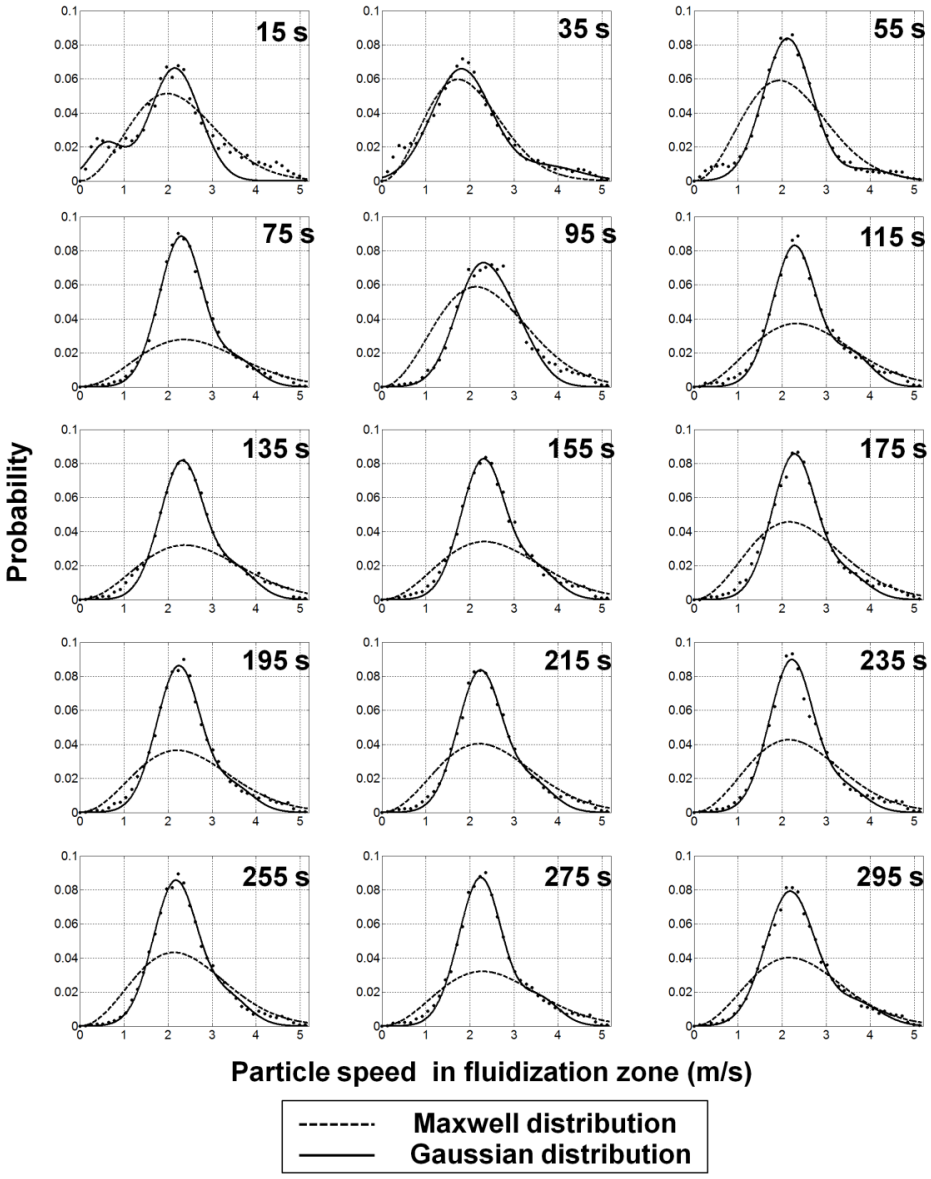

Figure 31. Changes in particle speed distributions during the spheronization process (dots) and the fitness to Maxwell (dotted lines) and Gaussian (solid lines) distributions, respectively

Given two particles with velocity of $\overrightarrow{v_1}$ and $\overrightarrow{v_2}$ respectively, the relative velocity between two particles is expressed as $\overrightarrow{v_{12}}$ and the unit vector passing the centres of the two particles ($\vec{e}$) can be expressed as follow:

$$\vec{e} \equiv \frac{\overrightarrow{r_{12}}}{|\overrightarrow{r_{12}}|} \tag{34}$$

where $\overrightarrow{r_{12}}$ is the vector joining the centres of the particles. The relative velocity can be decomposed into a normal component and a tangential component, which are $\overrightarrow{g_{12}}^n \equiv (\overrightarrow{v_{12}} \cdot \vec{e})\vec{e}$ and $\overrightarrow{g_{12}}^t \equiv \overrightarrow{v_{12}} - (\overrightarrow{v_{12}} \cdot \vec{e})\vec{e}$ respectively (Figure 32A).

Due to conservation of momentum, the velocity along $\overrightarrow{g_{12}}^t$ direction does not change and the particle velocity along $\overrightarrow{g_{12}}^n$ direction depends on elasticity of collision. For elastic collision, the two particles exchange velocity along $\overrightarrow{g_{12}}^n$ direction and remain unchanged in $\overrightarrow{g_{12}}^t$ direction (Figure 32B). However, for inelastic collision, the after-collision velocity in $\overrightarrow{g_{12}}^n$ direction decreases due to energy dissipation. Generally, more plastic materials can result in greater decrease in after-collision-velocity along the $\overrightarrow{g_{12}}^n$ direction, thus resulting in more similar after-collision velocities. Hence, the particle movement directions become even closer after a chain of collisions, causing a higher probability density in the centre of the plot.

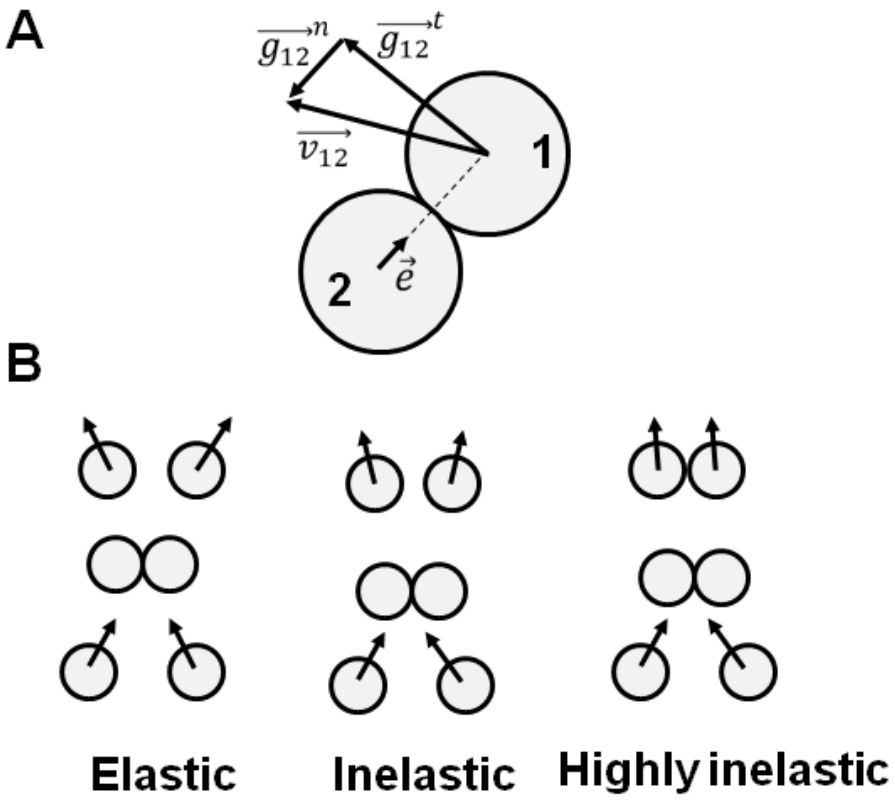

Figure 32. (A) Decomposition of relative velocity and (B) schematic diagram showing elastic, inelastic and highly inelastic collisions

4.C. Relationship between bed surface flow pattern and particle growth kinetics during spheronization

The purpose of this section was to investigate the relationship between bed surface flow pattern and particle growth kinetics. As PIV may detect velocity vectors that do not belong to the ring shaped in-process material, velocity vector filtering had to be performed first.

4.C.1. Effect of velocity vector filtering

Effects of the different steps of velocity vector filtering are shown in Figure 33. It is clearly shown that the in-process material could be detected by a threshold operation. However, the white part of the image after the threshold operation also included parts of the spheronizer wall and frictional base plate.

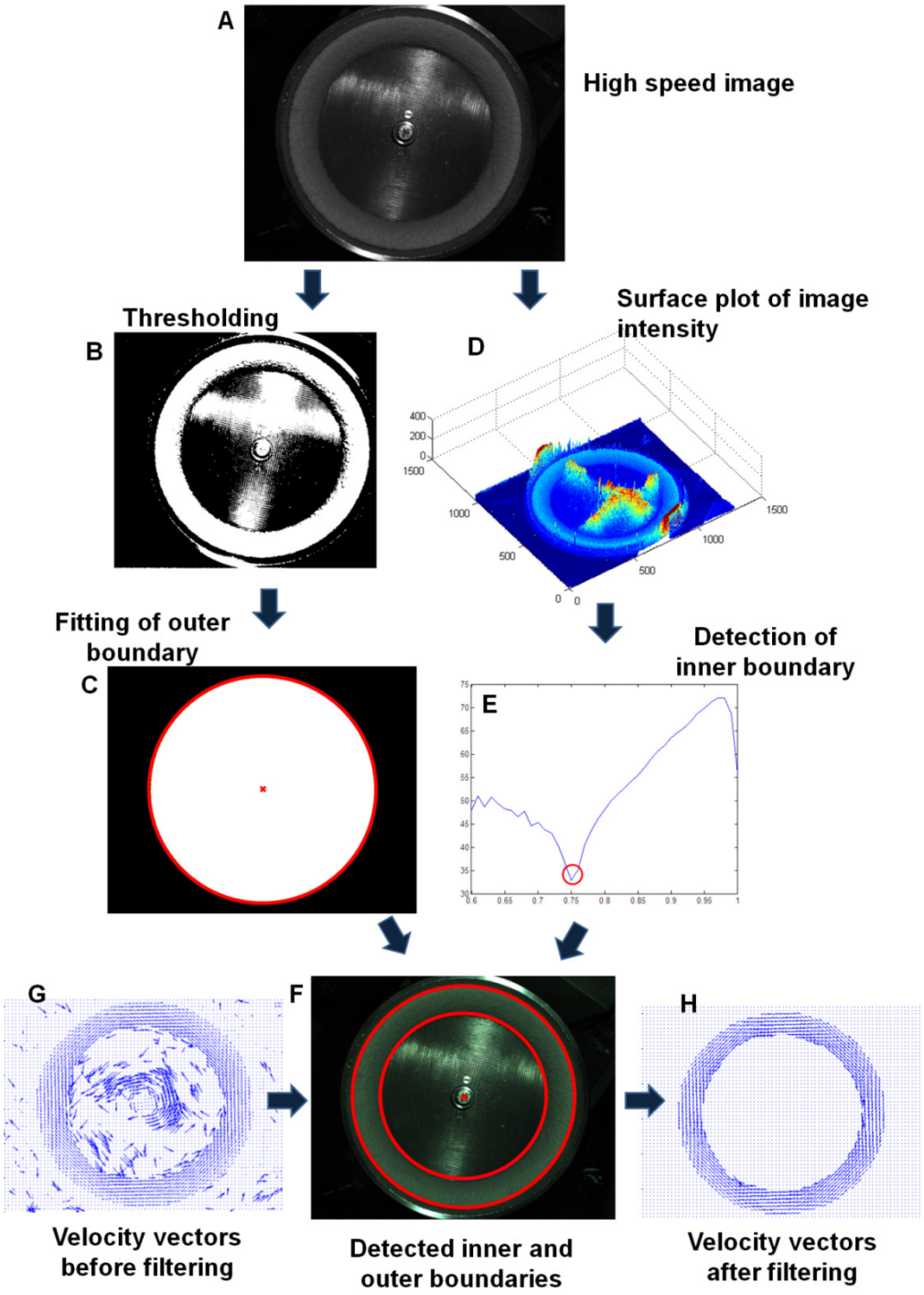

Figure 33. Sample results from the different steps of velocity vector filtering to detect the ring shaped spheronization bed surface

The spheronizer wall was removed by area opening of the binary image. The outer boundary of the major white object after the area opening and hole filling operations corresponded well to the outer line of the ring shaped bed surface, and the centre of the spheronizer was also detected with good accuracy (Figure 33B and 33C). In order to locate the inner boundary of the in-process material, mean gray-scale intensity of pixels with equal distances from the spheronizer centre were plotted against the distances from the spheronizer centre (Figure 33E). The distances were divided by the diameter of the frictional base plate for normalization purposes. As expected, the circle defined by the frictional base plate centre and the radius corresponding to the minimum mean gray-scale value fitted well with the inner boundary of the in-process material (Figure 33F). In the final step, the velocity vectors not located between the inner and outer boundaries were removed (Figure 33G and 33H). Generally, filtration of velocity vectors was effective in removing irrelevant vectors.

4.C.2. Relationship between bed surface mean speed and particle growth kinetics

The mean speed of in-process material on the bed surface was plotted against spheronization time (Figure 34). Firstly, it was interesting to note that the ranges for bed surface mean speeds were identical despite the large difference in spheronizer plate peripheral speeds. This may be because the kinetic energy within the fluidization zone dissipated rapidly by means of inelastic collisions as well as friction between particles in the frictional motion zone, thus bed surface mean speed was less affected by the spheronizer plate peripheral speed.

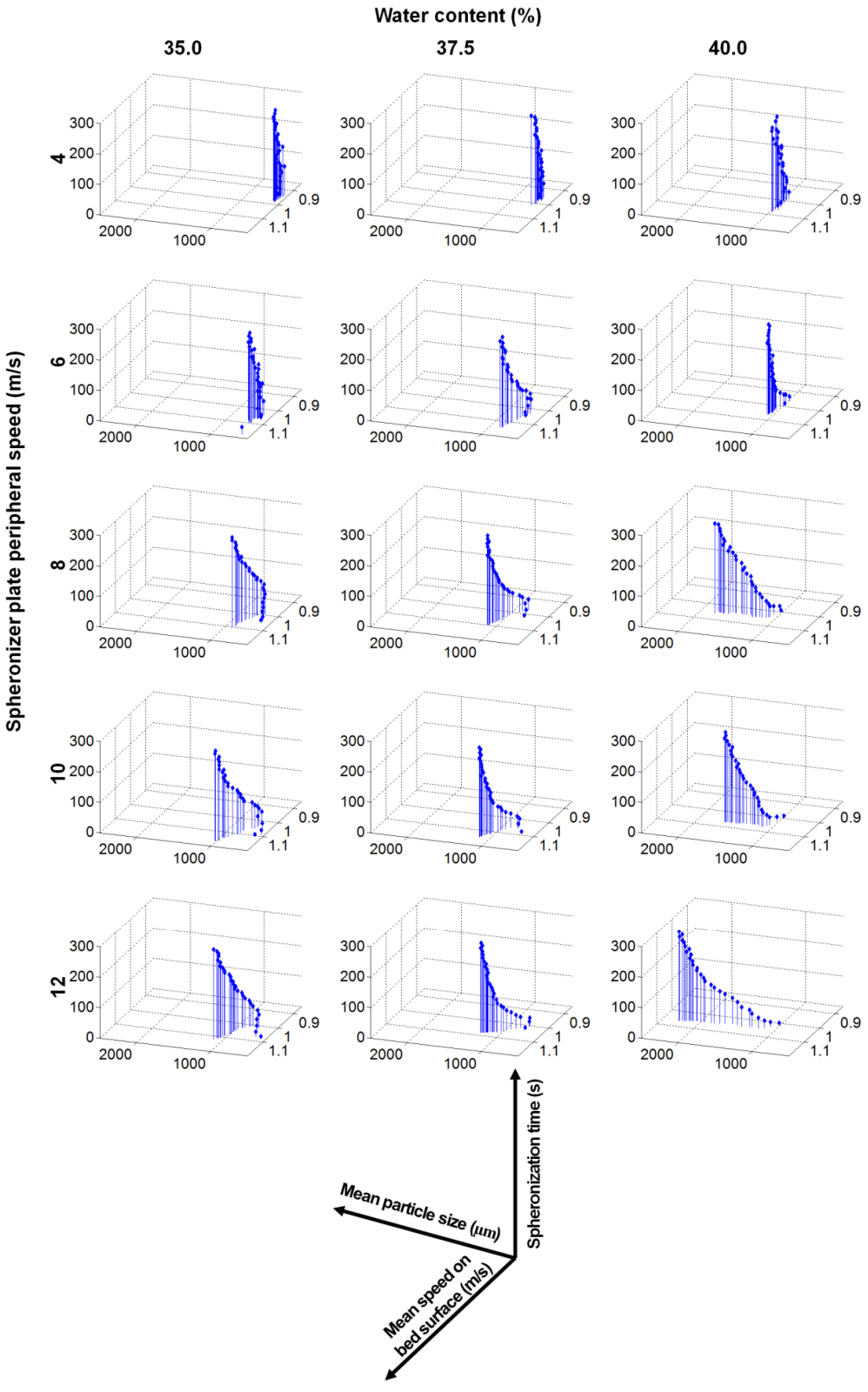

Figure 34. Changes in bed surface mean speed with respect to spheronization time and mean particle size

For conditions of 35.0 % and 37.5 % water contents and plate peripheral speeds higher than 6 m/s, the bed surface mean speed was found to decrease in the initial stage and rise in the later stage of the spheronization run. The drop in bed surface mean speed in the initial stage may be due to the fines generated in phase I. Compared to coarse particles, the fines cannot transfer momentum effectively to particles in the frictional motion zone due to their smaller mass, thus resulting in a drop in the bed surface mean speed in the initial spheronization stage. However, as the spheronization process progressed, the fines were gradually consumed by phase II layering. This led to the rise in bed surface mean speed. Close examination of the plots of those spheronization conditions ($W_{content} \leq 37.5\%$ and $V_{peri} > 6$m/s) revealed that the time point when bed surface mean speed rose back to the initial level approximately corresponded to the time point when particles grew into mean size of around 1 mm. This may be explained by the completion of the layering of fines onto the coarse particles, thus resulting in a more effective momentum transfer from the frictional base plate. For spheronization conditions of 40.0 % water content and spheronizer plate peripheral speed higher than 4 m/s, the bed surface mean speed was found to increase monotonically without a drop in speed during the initial stage. This may be because less fines was generated from phase I and faster particle growth occurred in phase II due to the high plasticity of the extrudates, resulting in a very short period for phase I and phase II particle growth. As the first section of the video section was captured 5 s after the start of the spheronization process, phase I and II particle growth may have already been completed. Hence, a monotonic increasing pattern of bed surface mean speed was observed.

4.C.3. Possibility of using of bed surface flow pattern for spheronization process monitoring

The bed surface flow pattern is reflective of the particle growth kinetics. However, several issues need to be addressed before use bed surface flow pattern can be used to monitor the spheronization process. Firstly, as PIV is computationally extensive with a large number of high speed image pairs to be processed for obtaining the bed surface flow pattern at each single time point, a high performance computer is required to yield timely measurement results. A parallel computing system may be employed as PIV analysis of multiple images pairs can be carried out simultaneously. Secondly, the camera calibration system is complex and rather impractical for use in product manufacturing. Hence, a self-calibration system would be a requirement to resolve this issue for implementation as a potential PAT tool.

It is also important to mention that although PIV is useful for investigating the flow pattern of the whole bed surface, it is not the only tool available for velocity measurement. Laser Doppler velocimetry may be another method to measure particle velocity on the bed surface. Compared with the PIV system, laser Doppler requires less computation but only point-wise velocity information may be obtained. Hence, multiple laser Doppler sensors may be used simultaneously for the purpose of ensuring 2D array measurement of bed surface speeds.

4.D. Development of visiometric process analyzer for quantifying particle recirculation within the partition column of the bottom spray fluid bed coater

The first objective for investigating bottom spray fluid bed coating was to develop a visiometric process analyzer to quantify the particle recirculation within the partition column, which is a major source of variability affecting coat uniformity. In order to achieve this, high speed video imaging and ensemble correlation PIV were employed for quantification purpose, and image tracking was used to verify the accuracy of ensemble correlation PIV.

4.D.1. Advantages of visiometric process analyzer for quantifying particle recirculation probability

Besides ensemble correlation PIV, PEPT, optical fiber and image tracking are some of the available methods that can be used to quantify particle movement within fluid bed coaters (He *et al.*, 1994; Saadevandi and Turton, 1998; Fitzpatrick *et al.*, 2003; Karlsson *et al.*, 2006; Palmer *et al.*, 2006; Bi and Pugsley, 2007). However, not all of these techniques have potential to be developed as a process analyzer that is non-invasive, sensitive and able to provide timely measurements. Compared to these existing methods, high speed video imaging coupled with ensemble correlation PIV is non-invasive and able to yield timely measurement. Hence, this technique for particle recirculation quantification can be developed as a process analyzer.

4.D.2. Samples of original and pre-processed high speed images

A sample high speed image is shown in Figure 35A. Figure 35B depicts the sample image after morphological image pre-processing. From Figure 35B, it

can be observed that most of the particles may be represented by a disk with radius equal to or slight larger than 2 pixels.

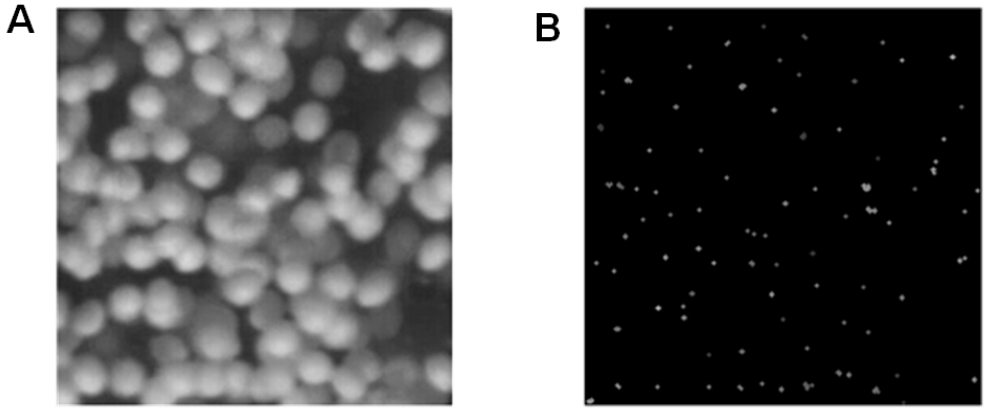

Figure 35. (A) Sample of original image from high speed video clips (recording speed: 4219 fps), (B) sample of pre-processed image (air flow rate: 90 m^3/h, atomizing air pressure: 1.5 bar)

4.D.3. Effect of ensemble correlation PIV

Different numbers of correlation planes were investigated to study the influence of number of correlation planes on the PDFs obtained. The ensemble correlation planes from a single image pair, 20, 100, and 500 image pairs were normalized and shown in Figure 36.

Correlation result obtained from a single image pair was noisy due to velocity differences as well as similarity in the appearance of the particles (Figure 36A). Thus, it was not possible to distinguish any characteristic peak. For the ensemble correlation result from 20 image pairs (Figure 36B), the main peak still did not stand out from the rest of the peaks. With ensemble of 100 image pairs (Figure 36C), noise was largely suppressed and a dominant peak was observed although there were still some relatively large baseline fluctuations. Correlation result from 500 image pairs (Figure 36D) was found to be sufficient for use to conduct further analysis as the noise was well suppressed.

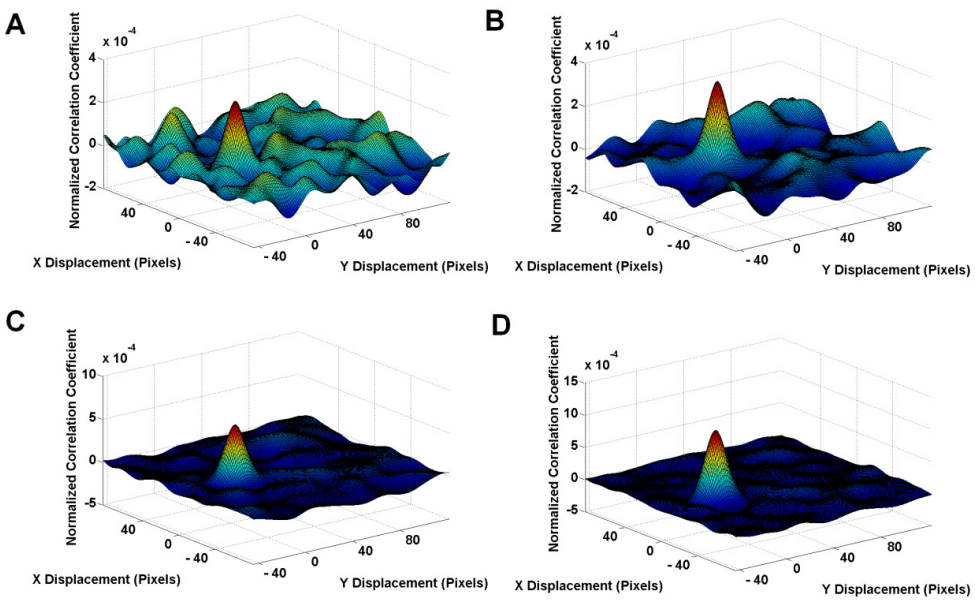

Figure 36. Correlation results from (A) a single pair of frames, (B) 20 image pairs, (C) 100 image pairs, and (D) 500 image pairs

4.D.4. Particle displacement probability density function verification by image tracking

The contour plots of particle displacement PDF obtained from ensemble correlation PIV results without image pre-processing, tracking results from 1000 randomly selected particles, and ensemble correlation PIV results after image pre-processing are shown in Figure 37A, Figure 37B and Figure 37C, respectively. The numerical marking of a point (*x, y, numerical mark*) on the plot indicates the relative probability of a randomly chosen particle displacing *x* pixels towards the *X* direction and *y* pixels towards the *Y* direction. While the shapes derived from contour plots of ensemble correlation PIV data without pre-processing (Figure 37A) and the verification data (Figure 37B) were identical, the scales of the verification data and ensemble correlation results without image pre-processing were found to be different. This difference may be due to the particles having a particle image diameter of approximately 20 pixels. During the operation of 2D cross-correlation, there would be a positive

correlation as long as particle displacement was less than one particle diameter in two adjacent frames, resulting in the difference between the verification data and the ensemble correlation results. However, due to the nature of cross-correlation, a larger particle displacement is always reflected by a high correlation value farther from the original position. Hence, for comparison purposes, i.e. coating performance between different coating conditions or coaters, ensemble correlation PIV without image pre-processing is still useful.

The contour plots from the verification data and ensemble correlation PIV result after pre-processing were close both in shape and displacement scale (*RMSE* = 0.0088). These findings further provided evidence that the difference between the ensemble correlation PIV results and the verification data was mainly due to the large particle image diameter. With image pre-processing, reduction in particle image diameter led to an increase in measurement accuracy. This was also in agreement with the notion of standard PIV that particle image diameter slightly larger than 2 pixels yielded better accuracy than other particle image diameters. Therefore, ensemble correlation PIV was adequate for comparison purposes but for absolute particle velocity distribution, high speed images are best pre-processed to adjust for differences in particle image diameter in order to improve measurement accuracy.

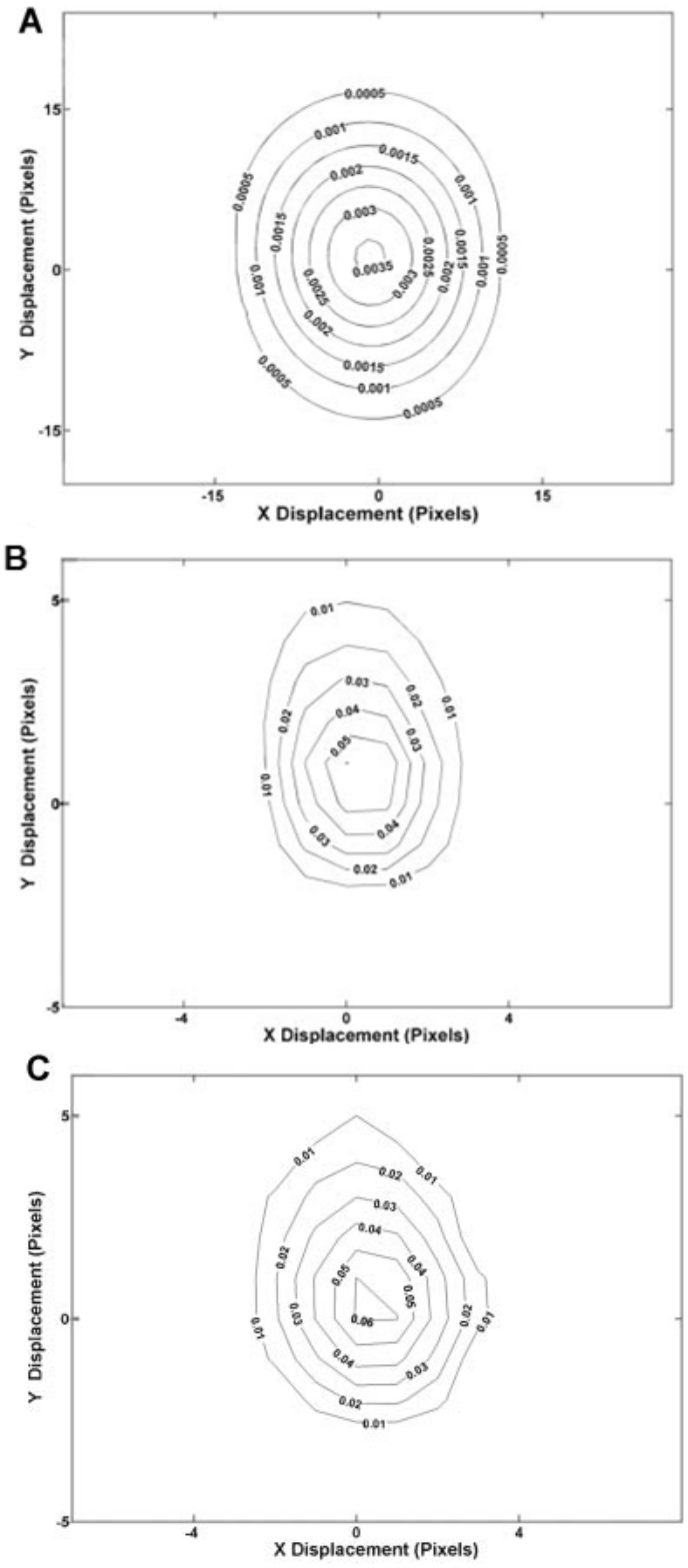

Figure 37. Contour plots of particle displacement PDF from (A) ensemble correlation PIV results without image pre-processing, (B) verification data after tracking of 1000 randomly selected particles and (C) ensemble correlation PIV result after image pre-processing

4.D.5. Use of particle displacement PDF data

As the recording speed is known, particle displacement PDF can be converted into particle velocity distribution, and then further resolved into particle velocity magnitude and orientation histograms. For the purpose of illustration and comparison, velocity magnitude and orientation histograms of air flow rates of 80 m^3/h and 100 m^3/h are plotted and shown in Figure 38.

The particle velocity magnitude histograms in Figure 38A provide information on probability of randomly chosen particles to move within certain speed ranges towards four main directions, i.e. upward-left, upward-right, downward-left and downward-right directions. In the particle velocity orientation histograms (Figure 38B), the radius of each circular sector represents the relative probability of particles moving toward the orientation range covered by the circular sector. Particle velocity magnitude histograms quantify how fast particles move in the four selected directions whilst particle velocity orientation histograms depict the overall orientation of particle movement.

In the particle velocity magnitude histograms, the downward bar depicts the probability of particles undergoing recirculation within the partition column. As discussed previously, such recirculation may contribute to poorer coat quality and even the propensity to agglomerate from the perspective of particle movement and drying efficiency.

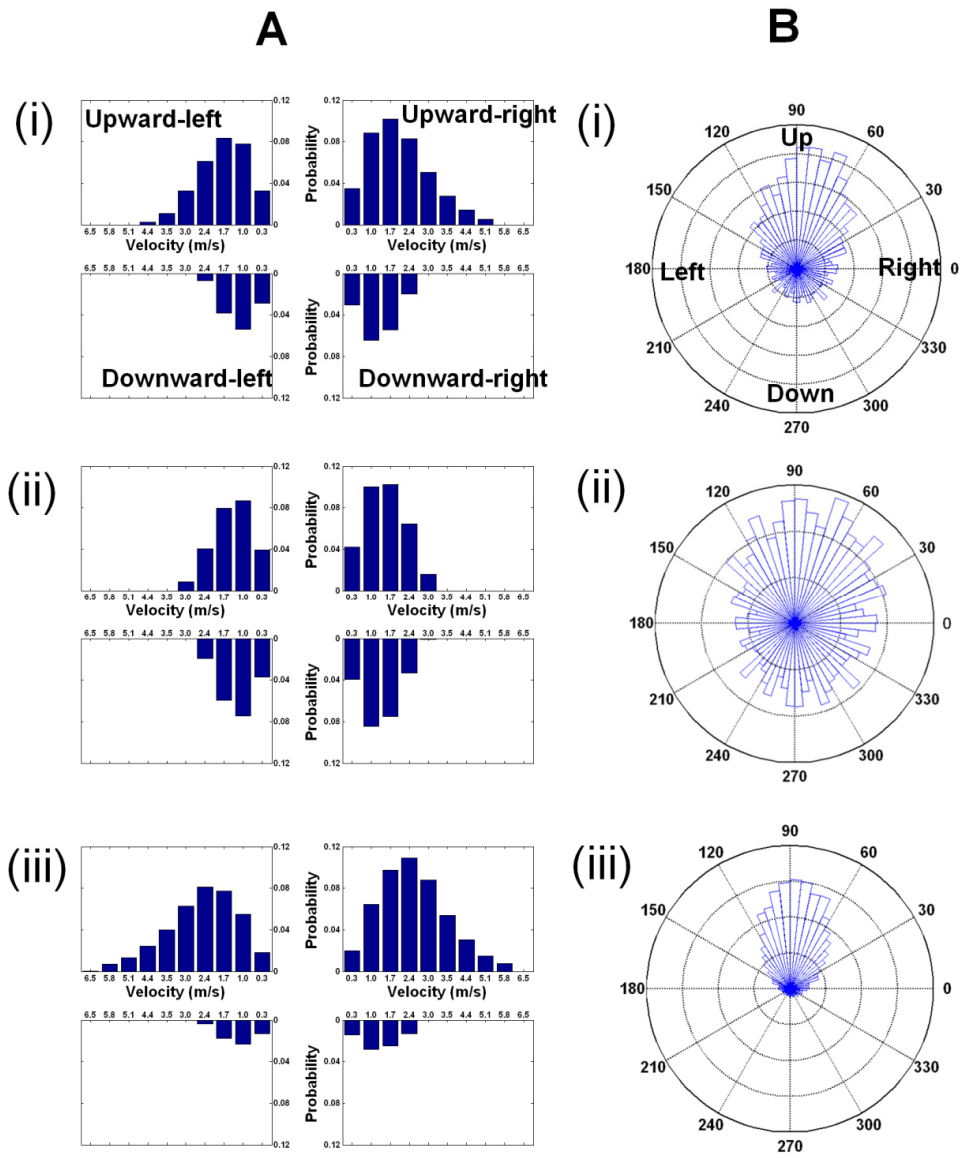

Figure 38. (A) Particle velocity magnitude histograms under atomizing air pressure of 1.5 bar and air flow rates of (i) 80 m^3/h, (ii) 90 m^3/h, (iii) 100 m^3/h; and (B) particle velocity orientation histograms under atomizing aire pressure of 1.5 bar and air flow rates of (i) 80 m^3/h, (ii) 90 m^3/h, (iii) 100 m^3/h

Particle recirculation probability from different combinations of coating parameters, such as, air flow rate, atomizing air pressure and partition gap, can be compared and combinations of coating parameters, under which particle recirculation probability is minimized, may be identified. For the bottom spray fluid bed coating process, monitoring particle recirculation by a quantitative manner enables prediction of the liability towards inferior coating conditions, and timely adjustments can be made to ensure positive coating conditions throughout the coating process. For example, as shown in Figure 38A, particle recirculation probability under air flow rate of 100 m^3/h (Figure 38A (iii)) was lower than that at 80m^3/h (Figure 38A (ii)) or 90 m^3/h (Figure 38A (i)). By comparison, it may be deduced that air flow rate of 100 m^3/h was more suitable for coating in terms of particle movement. Figure 38B shows a similar trend to that of Figure 38A with respect to the probability of particle joining recirculation, but reveals more information about the orientation of particle movement within the coater's partition column.

4.D.6. Integration of visiometric process analyzers with current feedback process analyzers

Currently, there are several types of feedback process analyzers available, e.g. NIR spectroscopy and Raman spectroscopy systems for assessing coat thickness on-line (Kirsch and Drennen, 1996; Andersson *et al.*, 1999; Andersson *et al.*, 2000; Romero-Torres *et al.*, 2006). It is plausible that both coat uniformity and coat thickness may be well-controlled by integrating the visiometric process analyzer with online coat thickness measurement systems. This approach would make the drug release profiles of coated particles less variable and more predictable as the drug release rate depends on not only coat

thickness but also the uniformity of the coat layer (Haddish-Berhane *et al.*, 2006).

Nevertheless, some modifications need to be made to overcome the limitations in the current system. For integration considerations, an imaging probe with pulse lighting or fiber optics can be used to replace the current camera and lens. As coating fluid is sprayed within the partition column, a retractable probe that is able to shoot, wash and dry automatically is advantageous. Moreover, with two or more cameras, 3D measurement of the particle movement profile within the partition column is feasible, from which the fluid dynamics of the system can be derived.

4.E. Mechanism of particle recirculation within the partition column of the bottom spray fluid bed coater

The second objective in bottom spray fluid bed coating was to investigate the mechanism of particle recirculation within the partition column using the visiometric process analyzer developed in section **4.D**. A voidage measurement method was first developed and verified. Air velocities within the partition column as well as the extent of spray drying effect were then measured to gain insights into the fluid dynamics within the partition column.

4.E.1. High speed images within the partition column

From high speed images of particle movement within the partition column (Figure 39), it could be clearly observed that the particle voidage and movement patterns for the three particle size fractions were distinctly different.

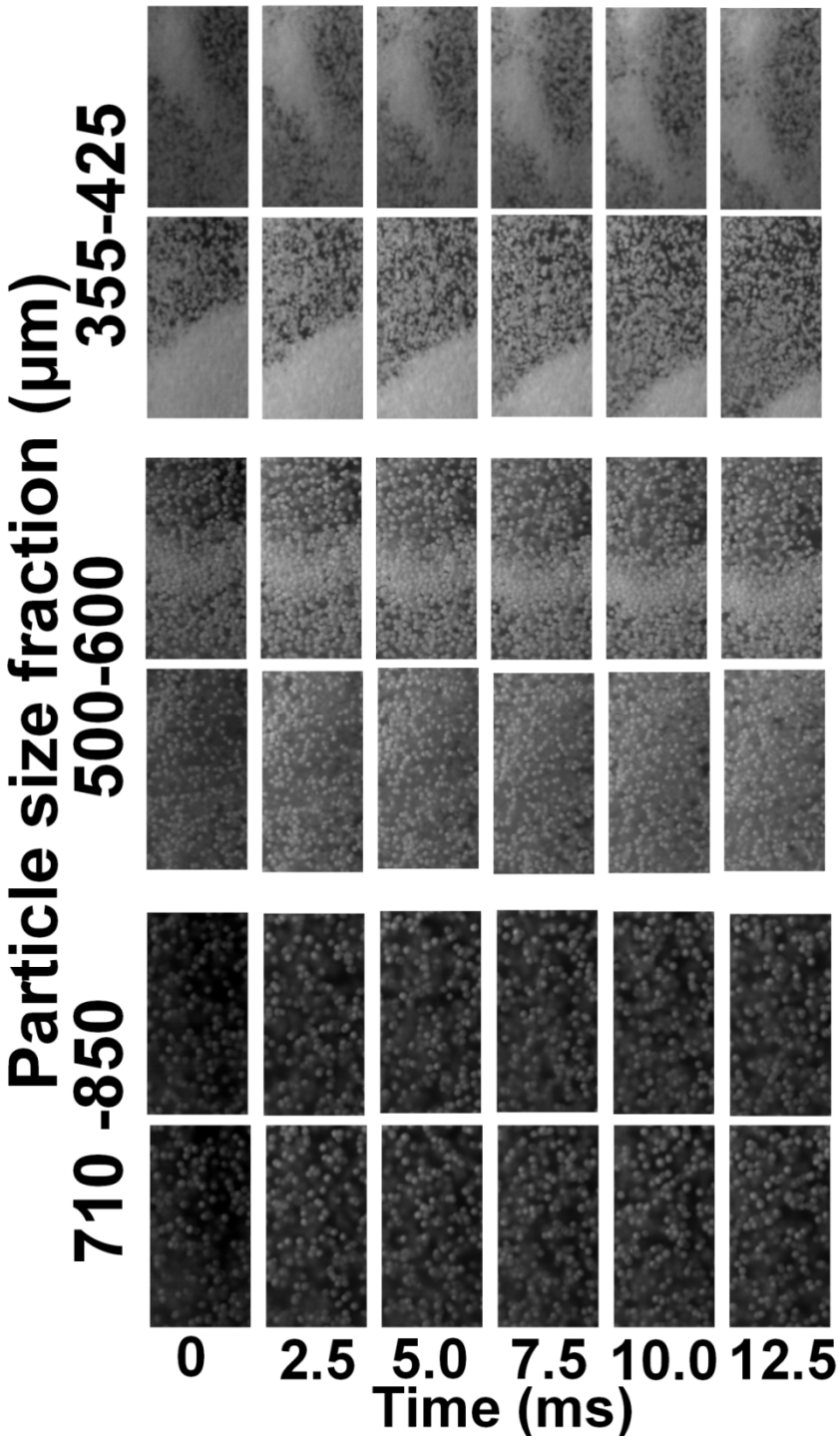

Figure 39. High speed images showing aggregate formation within the partition column

For the 710-850 μm size fraction, particles were observed to be dispersed uniformly, travelling upwards in a smooth manner. For the 500-600 μm size fraction, moderate size aggregates in the order of dozens of particles were observed. The aggregated particles moved downwards with relatively low speed. Moreover, the aggregates were found to form and break up quickly (within less than 1 s). For the 355-425 μm size fraction, larger aggregates formed and moved downwards at a higher velocity. The aggregates were denser and composed of more particles (in the order of hundreds of particles). Both ellipse- and streamer- shaped aggregates were found to exist within the partition column.

4.E.2. Effects and verification of particle number measurement

Figure 40 showed the sample results from each of the morphological image processing step. After gray-scale opening, intensity changes that were smaller than 2 pixels were suppressed (Figure 40B). Particles on the image were then detected using local maxima operation (Figure 40D). However, the local maxima that were not located on the particles were also detected. Any false positive particle detection was removed by intersecting the local maxima image with the border-cleared image (Figures 40D and 40E). The intersection was then reconstructed to link the broken parts from the same particles using a thresholding operation (Figure 40G). The number of labels corresponded to particle number (N_p) after the labelling operation (Figure 40H).

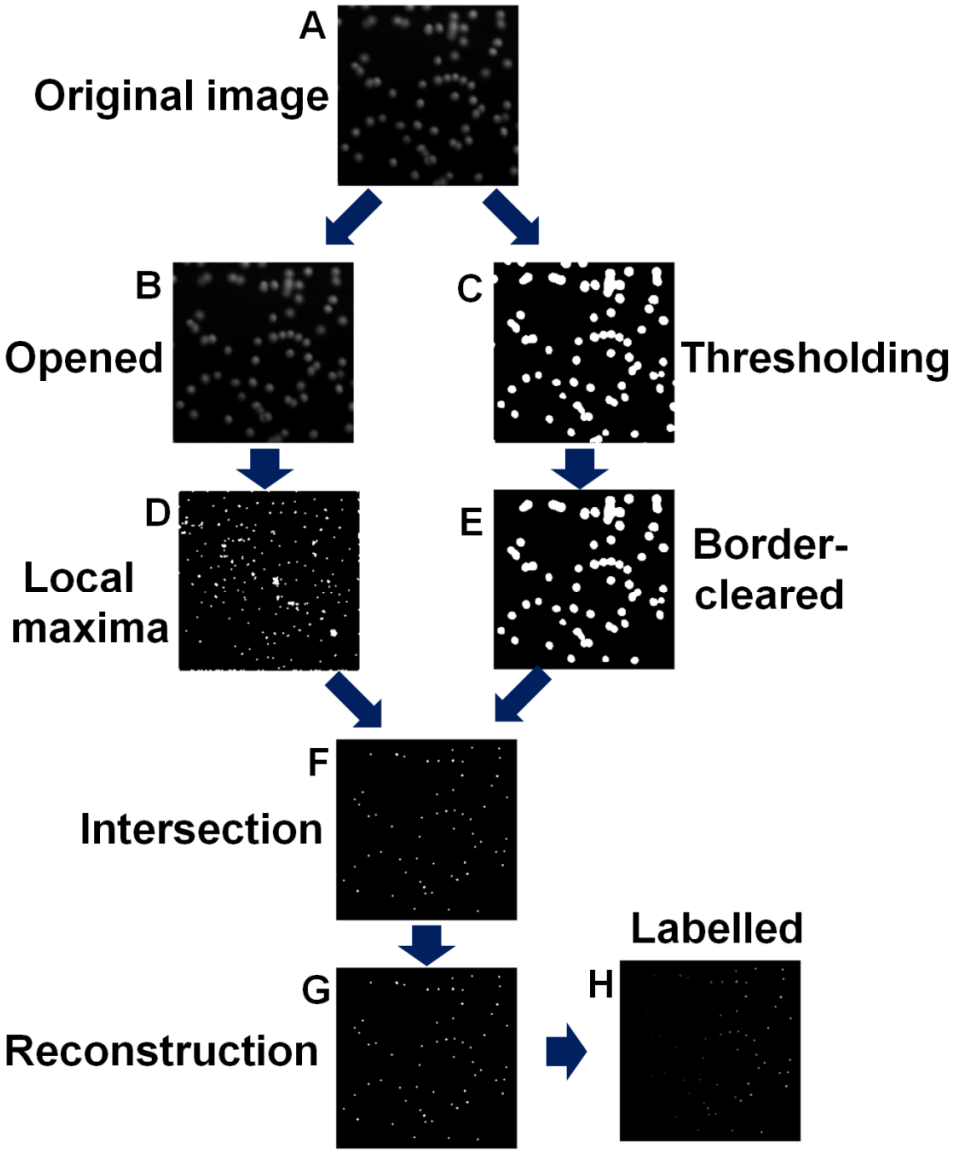

Figure 40. Flow chart with sample images depicting the different steps in morphological image processing for particle number measurement

The verification results and the proposed morphological image processing for counting of the particle number on the image are shown in Figure 41. The *RMSE* between the proposed method and the verification result was 1.8974. The *RMSE* for the particle counting results were less than 3% of the mean values, showing accuracy and robustness of the proposed method.

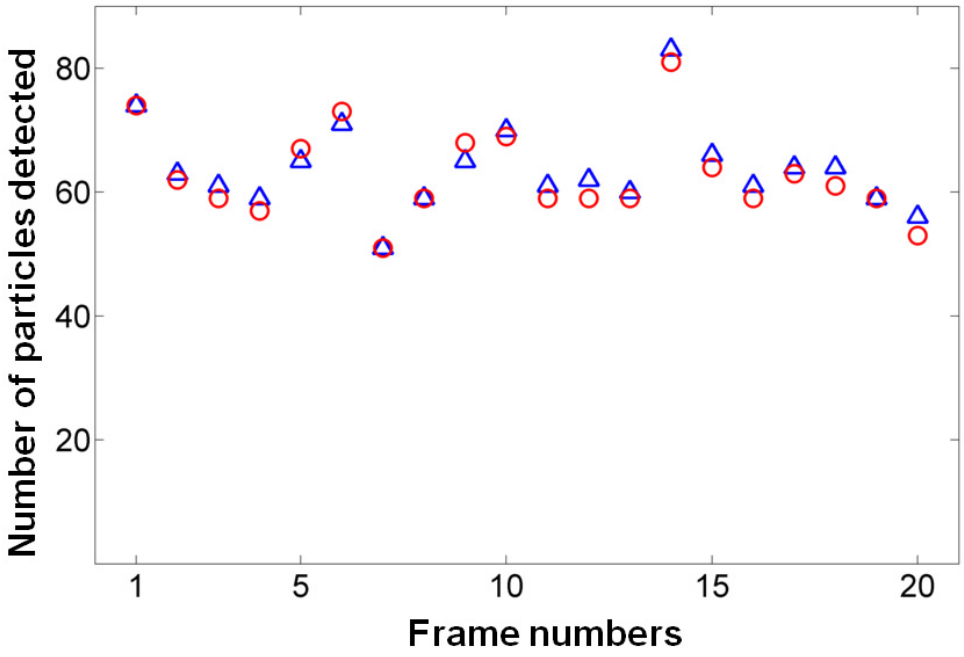

Figure 41. Verification (○) and morphological image processing results (Δ) for particle number detection

4.E.3. Recirculation probability and voidage measurement within the partition column

The particle recirculation probability and average voidage of the three particle size fractions are shown in Figure 42A and Figure 42B respectively. For the 710-850 μm size fraction, particle recirculation probability was found to increase with increase in the partition gap and AAI diameter. For the 500-600 μm size fraction, the trend was similar but the influences of partition gap and AAI became weaker. The overall recirculation probability was higher than that for the 710-850 μm particles. For the 355-425 μm size fraction, particle

recirculation was hardly influenced by the partition gap and AAI diameter and the recirculation probabilities were the highest among the three size fractions. The general trend of particle recirculation increasing with decreases in particle size confirmed the observation from high speed images. Moreover, for 710-850 µm and 500-600 µm size fractions, it was found that the average voidage increased with increased particle recirculation probability.

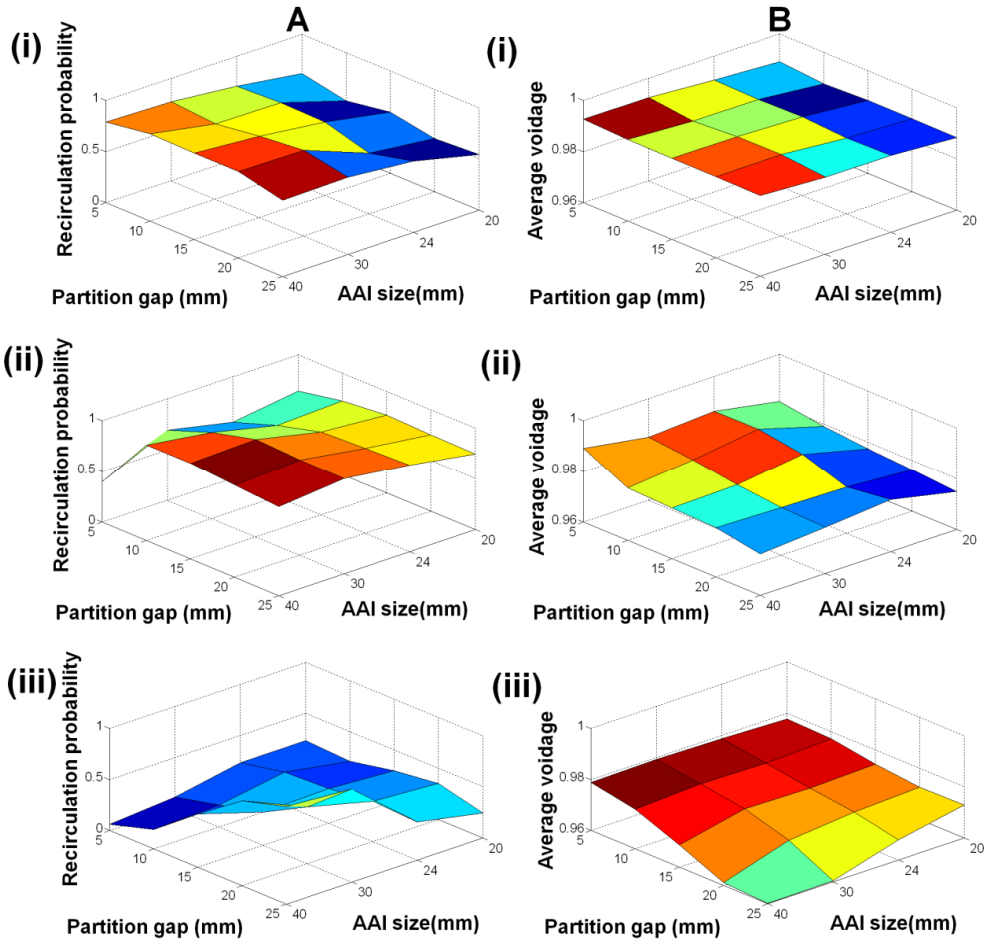

Figure 42. (A) Particle recirculation probability and (B) average voidage within the partition column for (i) 355-425 µm, (ii) 500-600 µm and (iii) 710-850 µm particles

Time series data of particle recirculation probability, voidage and vertical velocity component were plotted and shown in Figure 43. For the 710-850 µm particles, recirculation probability and voidage were found to be lower and

steady with time; the positive time series velocity plot indicated that particles were moving upwards in a smooth manner. For the 500-600 and 355-425 μm particles, recirculation probability and voidage were found to be unstable with larger fluctuations for smaller particles; both positive and negative velocities were found in the time series velocity plots, confirming the dynamic formation and breakage of aggregates for the smaller particles as shown in Figure 39.

4.E.4. Air velocity within partition column, single particle terminal velocity and boundary layer thickness

The air velocity within the partition column is shown in Figure 44. The estimated terminal velocities of 355-425 μm, 500-600 μm and 710-850 μm particles were 2.16 m/s, 2.93 m/s and 3.94 m/s, respectively. The average air velocity within the partition column (> 25 m/s) was found to be well above the terminal velocity of a single particle, implying that particle recirculation should not occur if only a single particle and the air stream are considered. By using equation 28 in page 76 the boundary layer was found to be 2.1 mm. Although it is true that less than ten particles may move downwards due to boundary layer development, the observed aggregates were composed of dozens or even hundreds of particles and a large number of downward moving aggregates were not located in the near wall region. This observation could not be attributed to boundary layer development. The results suggested that particle recirculation within the partition column may not be simply attributed to wall effect and low air velocity.

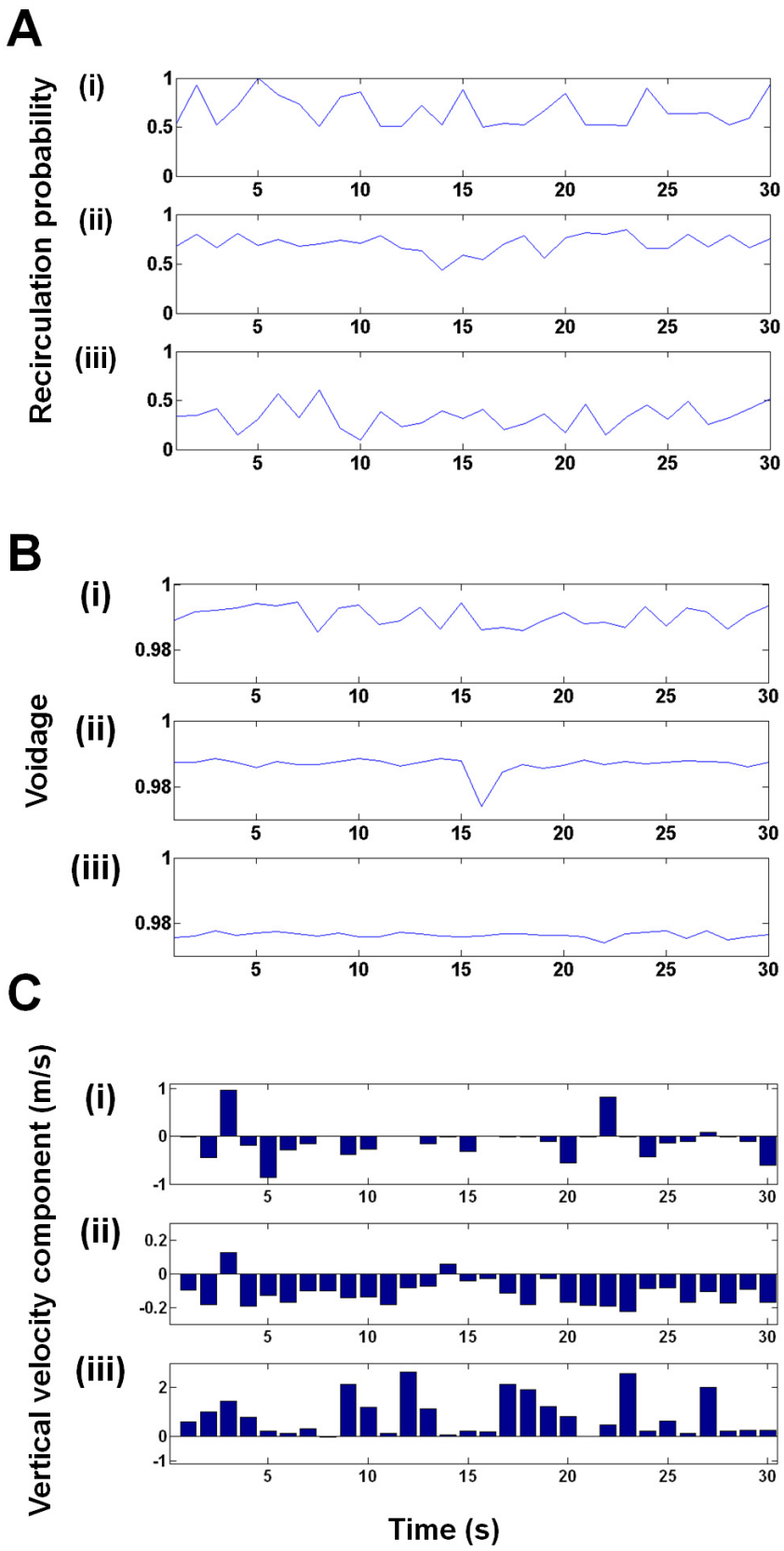

Figure 43. Time series (A) particle recirculation probability, (B) voidage and (C) vertical velocity component of (i) 355-425 µm, (ii) 500-600 µm and (iii) 710-850 µm particles, respectively

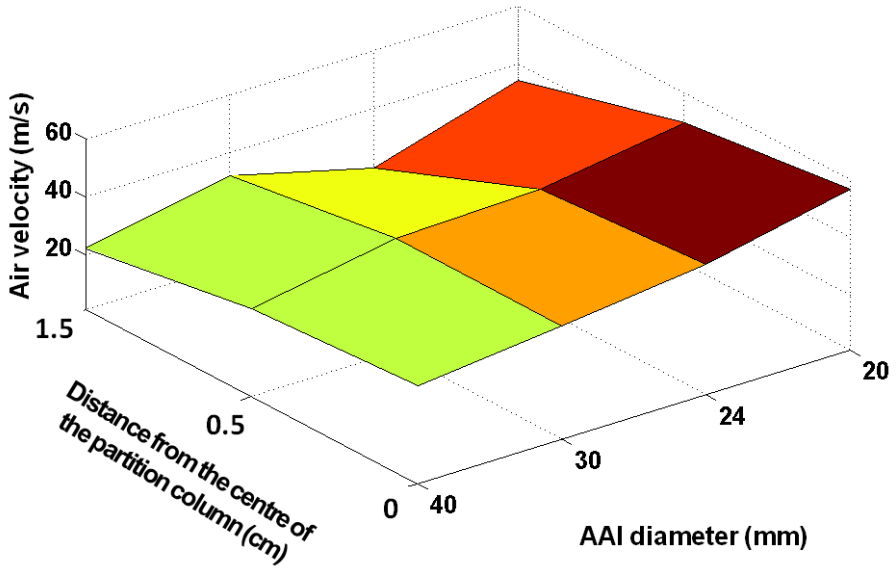

Figure 44. Air velocity measurement results within the partition column

4.E.5. Effects of meso-scale flow structure on drag force

From section **4.E.1.** to **4.E.4.**, it was found that low air velocity and wall effect were not the major causes of particle recirculation within the partition column; particle recirculation was observed to increase with a decrease in particle size. More importantly, high speed images showed that smaller particles joined particle recirculation in the form of clusters.

The particle recirculation phenomenon could be better explained by taking the influences of clusters (heterogeneous gas-solids dispersion) into consideration. Gravitational force and fluid drag force are the main forces acting on the particles within a gas-solids dispersion. The drag force has to exceed the gravitational force in order to convey each particle upwards. Taking the effect of multi-particles into consideration, the drag force acting on each particle depends greatly on the meso-scale structure of the particles, in particular,

whether the solids were dispersed homogeneously or heterogeneously within the air stream.

For homogeneous gas-solids flow, as particles occupy spaces within the air stream, the slip velocity, i.e. velocity difference between particles and air, increases under constant superficial air velocity. Hence, given a constant superficial air velocity or air flow rate, the higher the solids fraction, the greater the drag force each solid particle experiences. Under the framework of homogenous gas-solids flow, several equations for drag coefficient prediction have been proposed. For example, Wen & Yu proposed an empirical equation (Wen and Yu, 1966):

$$F_{deff} = F_{d0}(1 - \varepsilon_s)^{-2.7} \tag{35}$$

where F_{deff} is the effective drag force when multi-particle effect is considered, F_{d0} is the drag force of a single particle, ε_s is the solids volume fraction. Another more general drag force coefficient equation for homogenous system was proposed as follows (Di Felice, 1994):

$$F_{deff} = F_{d0}(1 - \varepsilon_s)^{-x} \tag{36}$$

where x is a function of particle shape, roughness, and Reynolds number respectively.

For heterogeneous gas-solids flow, which is observed for smaller particles, solid aggregates, i.e. clusters, appear within the gas-solids flow. For particles belonging to the clusters, drag reduction occurs mainly due to two reasons. Firstly, on a macroscopic level, as the voidage of a cluster is low, the air stream preferably flows through the high voidage regions rather than through

the clusters. With less air flow through the clusters, the slip velocity within the clusters is decreased as well. Sufficient slip velocity is critical for suspending spherical particles as 90% of the drag force is due to frictional force rather than pressure (Young *et al.*, 2004). Secondly, on a meso-scale level, the particles located on the cluster surfaces disturb and block the air stream from reaching the particles within the clusters. With little interaction with the air stream, the particles within the clusters suffer from drag reduction. This effect is especially important for the streamer-shaped clusters. Computational fluid dynamic simulation showed that the drag coefficient dropped drastically with cluster formation and drag force acting on a particle within a cluster was only 1 % - 10 % of the drag force in a single particle scenario (Yang *et al.*, 2003).

4.E.6. Origins of cluster formation and breakage

Aggregation is a natural tendency not only for gas-solids systems but also for liquid-solids suspensions. Hydrodynamic theory and energy minimization theory are the two major theories on cluster formation. According to the hydrodynamic theory, cluster formation was attributed to flow instability and wake interaction between particles (Grace and Tuot, 1979; Grace and Bi, 1997). Flow instability was mainly due to the air velocity and pressure fluctuations induced by turbulent flow within the partition column. Simulation showed that attractive force can develop when the alignment of particles is the same with air flow direction. Due to their low velocity and large wake, “mini” clusters were formed, and were able to easily capture single particles and grow rapidly. As for the energy minimization theory, the air stream seeks the path that minimize potential energy usage, i.e. the air stream always flow through particles along the path with minimal resistance (Li *et al.*, 1988). The air

stream's bypassing of the clusters can be viewed as the result of potential energy usage minimization of the gas-solids system. Cluster breakage may be due to two reasons. Firstly, breakage may be attributed to the cluster's collision with another particle or cluster with sufficient kinetic energy. Secondly, cluster breakage may also occur when the size of the cluster is comparable with that of the partition column diameter. This is because when the cluster diameter is comparable with the partition column diameter, a portion of air may flow into the clusters rather than bypassing them, increasing the drag force dramatically and breaking the cluster.

4.E.7. Comparison with circulating fluidized bed studies

Vertical pneumatic transport has been used to describe the gas-solids flow within the partition column of the bottom spray fluid bed coater (Christensen and Bertelsen, 1997). Vertical dilute pneumatic transport was also reported to be the main gas-solids flow pattern within the riser of the circulating fluid bed, which is a process widely used in chemical engineering (Grace and Bi, 1997) (Figure 45). Hence, it was claimed that the solids flow pattern within the riser of the circulating fluid was identical with that in the partition column of the bottom spray fluid bed coater (Christensen and Bertelsen, 1997). This analogy could be further supported by a comparison of their corresponding air velocity, particle size, particle density and column diameter parameters as listed in Table 5. Hence, it is reasonable to compare the physical characteristics of clusters found in this investigation with previously reported cluster parameters in circulating fluid bed systems. Cluster characteristics obtained in this investigation were listed together with those previously reported in circulating fluid bed studies (Table 6). The shape and diameter of clusters found in this

investigation were observed to be identical to those previously reported in circulating fluid bed studies. However, the sedimentation velocity was found to be lower. This could be due to the higher air velocity within the partition column of the bottom spray fluid bed coater. Overall, the findings lent further support to the cluster formation and drag reduction based theory for particle recirculation within the partition column of the bottom spray fluid bed coater.

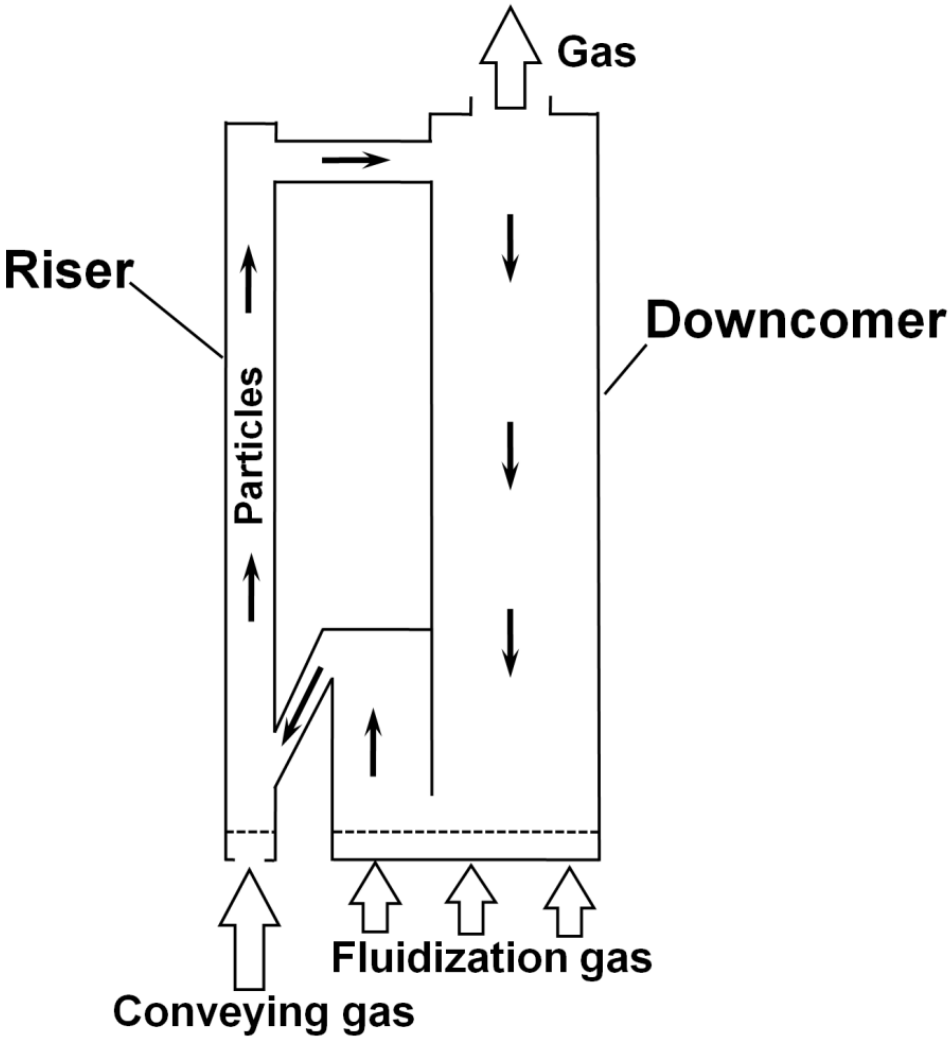

Figure 45. Schematic diagram of a typical circulating fluid bed

Table 5. Comparison between the riser of the circulating fluid bed and the partition column of the bottom spray fluid bed coater

Process parameters/particle characteristics	**Circulating fluid bed** (Horio, 1997)	**Bottom spray fluid bed coater**
Column/riser diameter	5-50 cm	5-15 cm
Air velocity	15-20 m/s	10-50 m/s
Particle diameter	50-500 μm	300-1500 μm
Particle density	Usually 1.00-1.80 g/cm^3	1.72 g/cm^3

Table 6.Comparison between characteristics of clusters found in this investigation and those from previous reports on the circulating fluid bed

Cluster parameters	**Circulating fluid bed** (Tian and Peng, 2004)	**Bottom spray fluid bed**
Cluster diameter	5-20 mm	15.5 ± 5.7 mm (355-425 μm size fraction)
		6.38 ± 4.1 mm (500-600 μm size fraction)
Cluster shape	Ellipse- and strip-shaped	Ellipse- and strip- shaped
Sedimentation velocity	0.5-2.0 m/s	0.14 ± 0.09 m/s (355-425 μm size fraction)
		0.12 ± 0.08 m/s (500-600 μm size fraction)

4.E.8. The extent of spray drying effect

The extent of the spray drying effect of particles with the three size fractions is shown in Figure 46. The 355-425 μm fraction was found to have the highest extent of spray drying effect, followed by the 500-600 μm particles and lastly by the 710-850 μm particles with least spray drying effect. It was observed that within the scope of this study, the more extensive the particle clustering, the higher the spray drying effect. This may be because with more extensive

cluster formation, more atomized droplets bypass the clusters without depositing on them. Moreover, these results also lent support to the voidage measurement findings that the average voidage observed during coating of smaller particles was higher than that observed during coating of large particles.

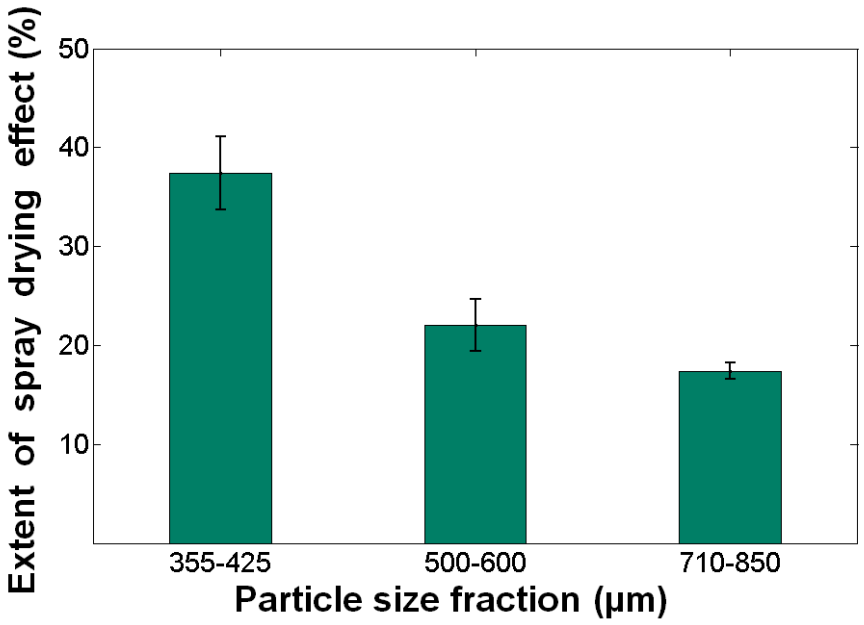

Figure 46. The extent of spray drying effect of particles with three different size fractions

4.E.9. Influences of cluster formation on coating process

Cluster formation had adverse effects on the bottom spray fluid bed coating process (Figure 47). Firstly, atomized coating fluid could only be deposited on the particles located on the surfaces of the clusters. As such, a non-uniform coat between particles may develop due to the particle shielding effect. Secondly, over-wet conditions may occur for the particles on the cluster surfaces. Thirdly, as particles aggregated together, their contact efficiency with the air stream is largely decreased, causing a decrease in the drying efficiency.

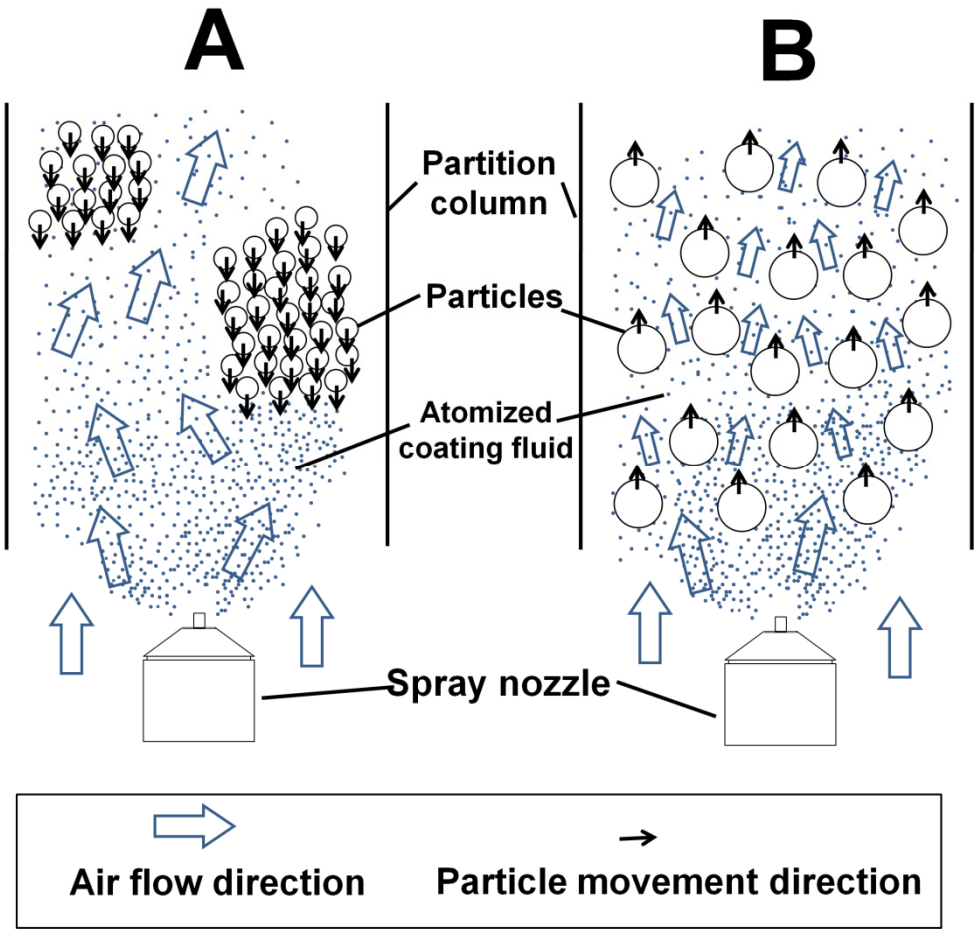

Figure 47. Schematic diagram showing particle movement and air flow (A) with clustering and (B) without clustering in the partition column of bottom spray fluid bed coater

It has been shown using high speed images that the clustering effect increased dramatically with decrease in particle size. Two main reasons account for this. Firstly, being smaller in diameter, smaller particles had lower inertia and their movements were more likely to be influenced by velocity and pressure fluctuations within the partition column. Secondly, smaller particles were able to form denser aggregates more easily than larger particles. Hence, relatively less air could flow through the denser aggregates, causing a larger extent of drag reduction and accelerating cluster growth (Figure 47). As smaller

particles caused an increase in clustering, more atomized coating fluid bypassed the solid clusters rather than deposit on the particle surfaces, resulting in a higher extent of spray drying effect. The influences of particle size on cluster formation and gas-solids contact efficiency were also supported by a previous study carried out on the circulating fluid bed (Dry and White, 1992).

4.E.10. Control of cluster formation within the partition column

Based on the cluster formation mechanism, two suggestions were proposed for controlling cluster formation within the partition column of the bottom spray fluid bed coater. Firstly, a lower partition gap may be employed during the coating process. This was based on the finding that higher solids content promote cluster formation and by lowering the partition gap, the solids flux rate into the partition column was reduced, thus creating a more dilute gas-solids flow and reducing the clustering effect.

The second possible solution was to induce swirling air flow into the partition column instead of using a direct upward air flow. This was based on the finding that attractive forces between particles developed when particle alignment was the same with air flow direction. Swirling air flow may be able to alleviate wake interaction and prevent the development of attractive forces between particles within the partition column. For the circulating fluid bed, a tangential secondary air injection had been reported to be installed in the bottom of the riser to generate swirling air flow and it was found that secondary air injections into the partition column were able to reduce cluster formation (Wang and Gibbs, 1991).

4.F. Development of a visiometric process analyzer for measuring particle mass flow rate in the fountain region

The third objective in the investigations on bottom spray fluid bed coating was to develop a visiometric process analyzer for measuring particle MFR in the fountain region. In order to achieve this objective, PIV and morphological image processing were used to determine particle velocity and particle number, respectively. Moreover, the developed process analyzer was also employed to investigate the influences of partition gap and AAIs on particle MFR as their roles could be better understood.

4.F.1. PIV and morphological image processing results

Sample high speed image for MFR measurement and the corresponding PIV result was shown in Figure 48A and Figure 48B, respectively. Most of the velocity vectors were detected to point downwards with similar velocity magnitude. Particle number was determined using the method developed in section **4.E.2**. With information on particle number and detected velocity, the particle MFR can be estimated using equation 30 in page 78.

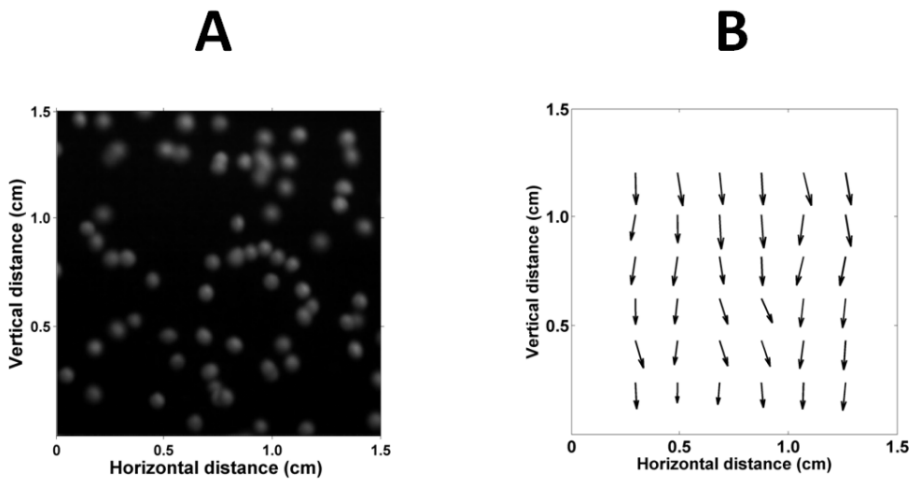

Figure 48. (A) Sample high speed image and (B) sample PIV results for MFR measurement

4.F.2.Comparative advantages of measuring downward moving particles

Measuring upward moving particles within the partition column is an alternative method for determining particle MFR. However, it is important to point out that measuring MFR within the partition column is not preferred due to a few reasons. Firstly, voidage within the partition column is much lower than that in the region between the product chamber and partition column. All the particles within the partition column cannot be fully captured by the camera due to shielding by particles located in the near wall region within the partition column. This may cause inaccurate particle velocity estimation as only a limited fraction of particles were observed on the image. Erroneous particle counting could also occur due to this reason. Secondly, the velocities of upward moving particles are much higher than those of falling particles at the periphery. Cameras must be operated at much higher recording speeds to freeze particle movement. In this case, timely data processing becomes complicated and computationally costly. Thirdly, the particle velocities within the partition column vary from downward moving particles joining recirculation to high speed upward moving particles in the centre of the partition column. This results in less accurate estimation of mean particle velocity. Lastly, not only is the interior of the partition column not easily captured, the coating process also makes it considerably 'dirtier' with many adhering spray droplets and fines due to attrition. Hence, less fouling conditions exist if images were captured from a view between the product chamber and the partition column.

4.F.3.Using visiometric process analyzer to investigate the role of partition gap and AAI

4.F.3.1. The dual role of partition gap

The effects of partition gap and air flow rate on particle MFR were plotted in Figure 49A. It was observed that particle MFR generally increased with higher partition gap and air flow rates with a flattening trend. This was because the height of the partition gap limited the rate of solids flux into the partition column. The levelling off trend may be attributed to intense turbulent air flow under high solids content conditions, which caused cluster formation and sedimentation/recirculation of particulates, thus limiting the particle MFR from increasing. Clustering and sedimentation under high solids content and turbulent air flow conditions are well known phenomena in circulating fluid bed systems (Horio, 1997). A similar flattening trend was also reported using the Wurster coater (Chan *et al.*, 2006). According to the bottom spray fluid bed coating models developed in several papers (Crites and Turton, 2005), a higher MFR usually results in a shorter mean particle cycle-time. This allows particles to undergo a greater number of coating cycles per unit time provided that the other conditions are kept constant, thus a more uniform coat layer can be expected.

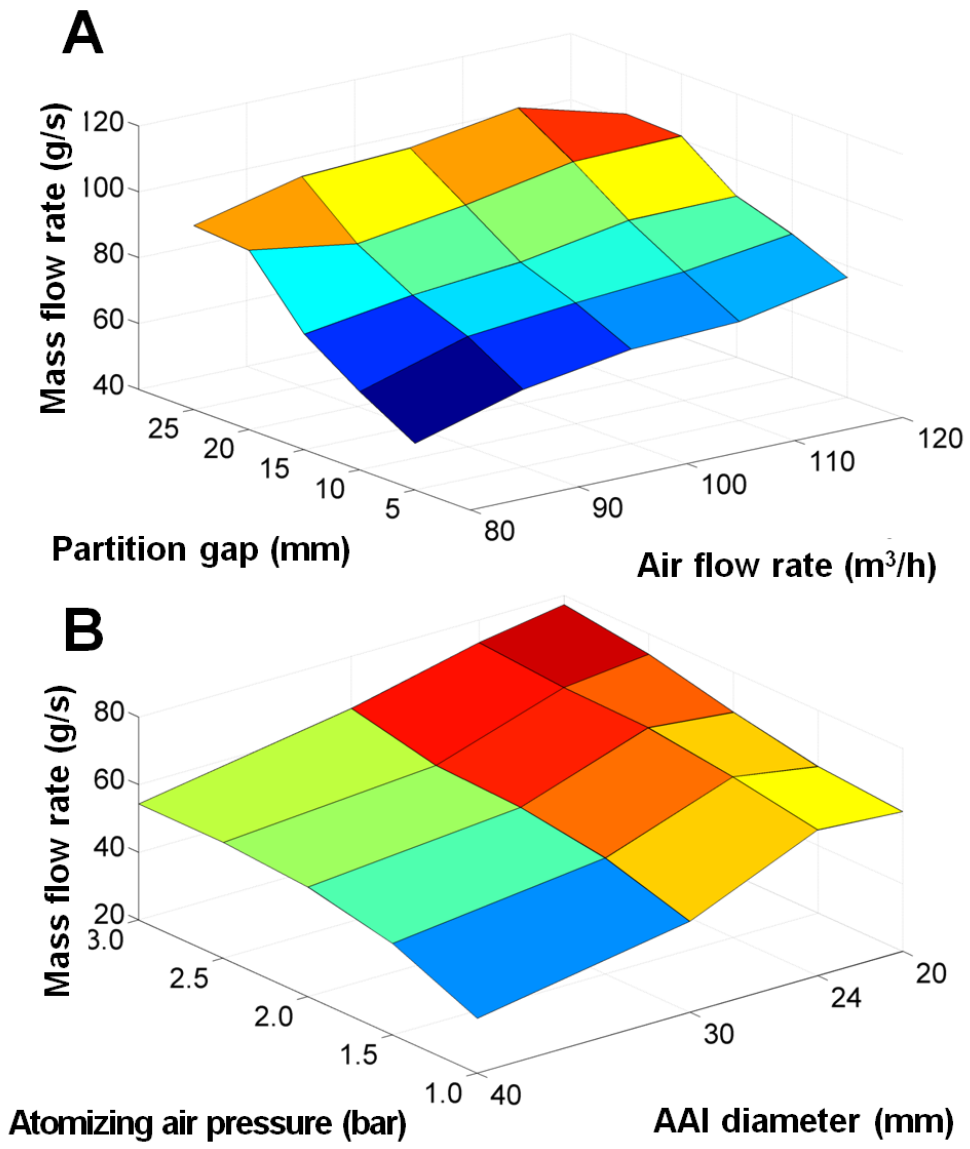

Figure 49. (A) Influences of partition gap and air flow rate on particle MFR; (B) influences of atomizing air pressure and AAI diameter on particle MFR

4.F.3.2. AAI diameter - the effectiveness of Venturi effect

It was also observed that particle MFR increased with higher atomizing air pressure, but decreased with larger AAI diameter (Figure 49B). The trends observed were in accordance with previous reports (Chan *et al.*, 2006). It was reported that the main mechanism of particle feeding in the Precision coating process is by the Venturi effect (Chan *et al.*, 2006). Venturi effect occurs when fluid passes through a smooth and narrow orifice with a fixed fluid flow rate

(Nakayama and Boucher, 1999). Due to the fixed fluid flow rate and smaller cross-sectional area near the AAI orifice, the fluid velocity increased to maintain air flow rate. According to the law of energy conservation, the fluid pressure dropped above the AAI orifice, bringing about a suction pressure at the bottom of the partition column. As demonstrated above, particle MFR increased with higher air flow rate, higher atomizing air pressure and smaller AAI size. This was because higher air flow rate and atomizing air pressure caused higher air velocity through the AAI orifice, inducing a lower pressure above the AAI orifice. Similarly, AAIs with smaller diameters caused higher air velocities at the orifice, hence inducing lower pressures at the base of the partition column, drawing more particles into the partition column. Hence, for coating of multi-particulates, AAIs with smaller diameters may be advantageous by contributing higher MFR. However, this trend may not hold for powder coating due to two reasons. Firstly, compared with free-flowing multi-particulates, powders are usually more cohesive and have relatively poor flowability. Thus, it may be difficult for the powder to flow easily into the partition column even with the help of a stronger Venturi effect. Hence, promoting powder flow by adopting larger diameter AAIs may be more effective than just relying on the Venturi effect alone. Secondly, arch formation is a well known phenomenon where powders flow through an orifice due to frictional force and particle elasticity (Duran, 1998; 2000; Cooper, 2001). Hence, AAIs with smaller diameters are more likely to promote arch formation as powders are exposed to frictional forces over a longer distance before being conveyed. As such, a combination of an AAI

with a larger diameter and a higher partition gap is suggested for powder coating or bottom spray granulation processes.

4.F.4. Uses and integration of online MFR measurement

As demonstrated, the proposed method for measuring particle MFR was accurate, non-invasive and useful for enumerating bottom spray fluid bed coating. With only a small transparent area (a 1.5 cm by 1.5 cm square in this investigation) on the product chamber needed for measuring particle MFR, a process monitoring camera could be easily integrated on an observation window in the bottom spray fluid bed coater for online MFR monitoring. Moreover, a relatively small image size ensures fast PIV and morphological image processing. As an example, it took less than 5 s to complete a MFR measurement using a desktop computer. Moreover, it is worthwhile to point out that the proposed method may need modification for use in large scale coaters. This is mainly because the distance between the product chamber and partition column is much longer and a lens with sufficient depth of field is required. In this situation, modifications to the proposed process analyzer may be needed to provide adequate illumination. Moreover, corrections for images distorted by lens distortion may also be used. Volume illumination using a laser light source with optics may be employed to provide an intense and spatially confined light beam. Camera calibration techniques can be used for large scale coating process monitoring to ensure measurement accuracy.

Real-time MFR measurements can also be used to control spray rate and prevent agglomeration in the spray zone. It is generally agreed that agglomeration arises when the particles are over-wetted and liquid bridges

form between particles. Under a fixed spray rate, with a higher MFR, the atomized coating fluid deposits on more particles and over-wetting conditions are less likely to arise. Hence, particle-fluid flow ratio (*PFFR*) was proposed for quantifying the balance status between particle MFR and coating fluid spray rate. *PFFR* is defined as:

$$PFFR = \frac{MFR}{SR} \tag{37}$$

where *MFR* is the particle mass flow rate and *SR* is the spray rate of the coating fluid. A minimum *PFFR* can be measured experimentally and the coating process may be controlled directly based on *PFFR* in order to facilitate coating speed. During coating process scale-up, process parameters can be tuned to keep the same *PFFR* as that of the pilot scale coater to avoid agglomeration.

4.G. The influence of annular bed flow pattern on coat uniformity

As the role of annular bed flow pattern on coat uniformity is still not clear, a visiometric process analyzer was developed to detect and classify the annular bed flow patterns. Colour coating and tristimulus colourimetry were used to examine coat uniformity of in-process samples. After ruling out the influences of particle recirculation within the partition column and particle MFR, the influence and significance of annular bed flow pattern on coat uniformity were discussed. The feasibility of using visiometric process analyzer to monitor annular bed flow pattern in large scale coating was further examined.

4.G.1. Annular bed flow patterns detected using visiometric process analyzer

A sample high speed image of the overall annular bed was given in Figure 50. White particles were evenly distributed in the annular bed and strongly contrasted from the red (dark) particles, thus serving well as seed particles for PIV.

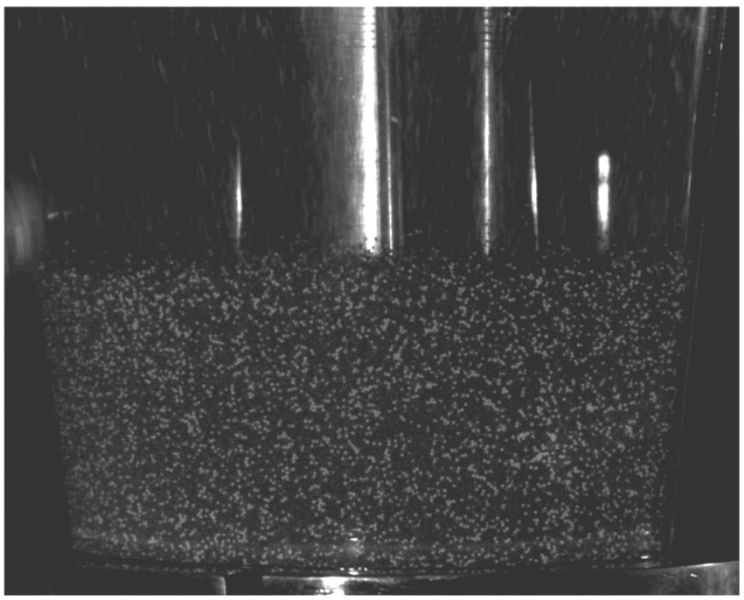

Figure 50. Sample high speed image of annular bed flow

It was clearly shown that the visiometric process analyzer has successfully detected annular bed flow patterns in the bottom spray fluid bed coater (Figure 51A). With AAI-20 (Figure 51A), the air flow rate passing through the annular region was higher than when the other two AAIs were used. Intense bubbling fluidization was observed. Bubbles arose from the bed bottom, moved upwards and burst through the bed surface, scattering some particles into the air. Particles around the bubbles were recorded to move at a higher velocity than the rest. It was also observed that particles were transported from the bottom upwards to the top of the bed in the wake of each bubble. This flow

pattern was termed “global fluidization” as the bubbles induced generalized particle movement and mixing in the annular bed. When AAI-24 was used (Figure 51A(ii)), the air flow rate passing through the annular bed was lower and bubbling fluidization was only observed in the lower region of the bed. The bubbles were smaller and dissipated upon reaching the middle of the bed. Hence, this flow pattern was named “localized fluidization”. In contrast, AAI-30 induced a uniform, downward, “plug flow” in the annular bed (Figure 51A(iii)); fluidization was not evident in this flow pattern.

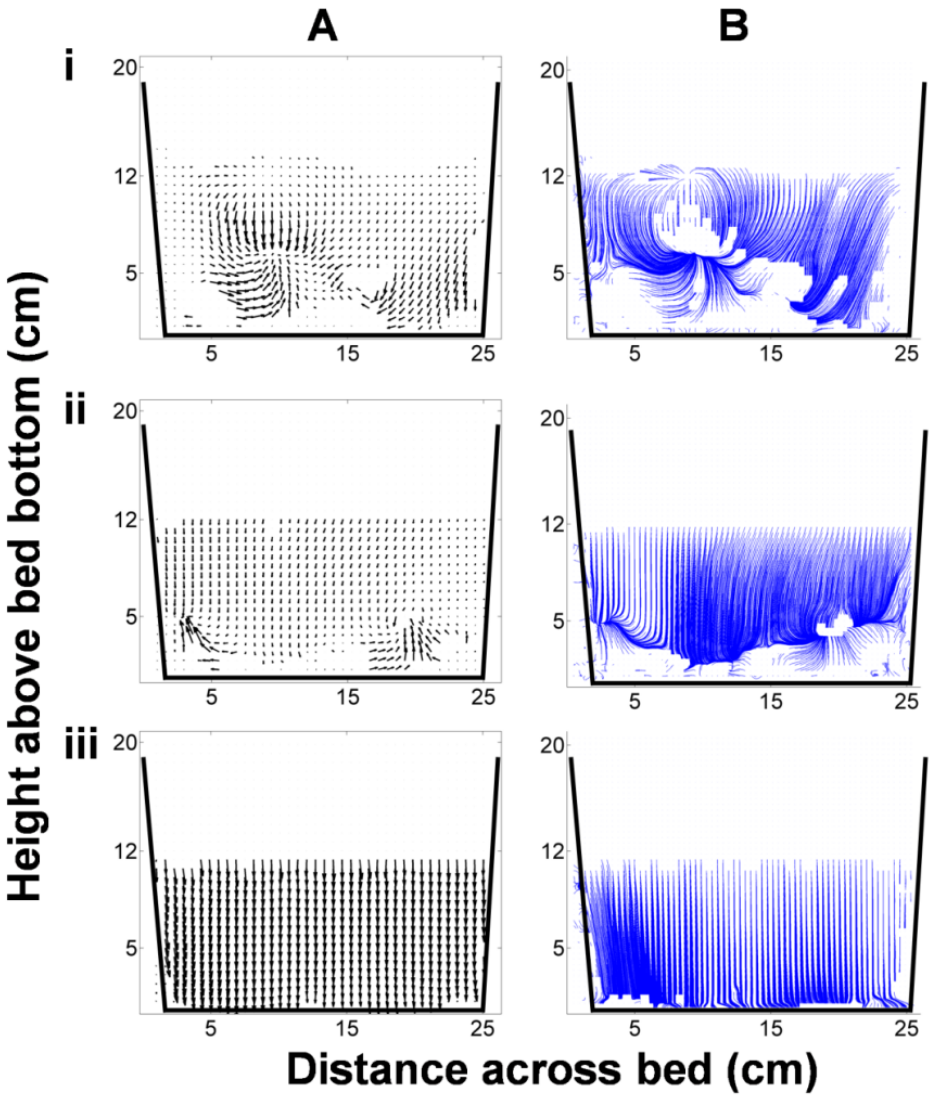

Figure 51. (A) Sample PIV results of annular bed flow using (i) AAI-20, (ii) AAI-24 and (iii) AAI-30; (B) sample streamlines from PIV results using (i) AAI-20, (ii) AAI-24 and (iii) AAI-30

4.G.2. Coat uniformity of in-process samples

$\overline{dE}$ of in-process samples were plotted in Figure 52A. $\overline{dE}$ rose with coat weight gain but at a gradually decreasing rate. The increasing $\overline{dE}$ were attributed to the increase in particle surface colour intensity with more and more red colour pigment being deposited on the particle surfaces. The levelling trend in the latter portion of the $\overline{dE}$ plot may be due to saturation of colour pigment on the particle surfaces.

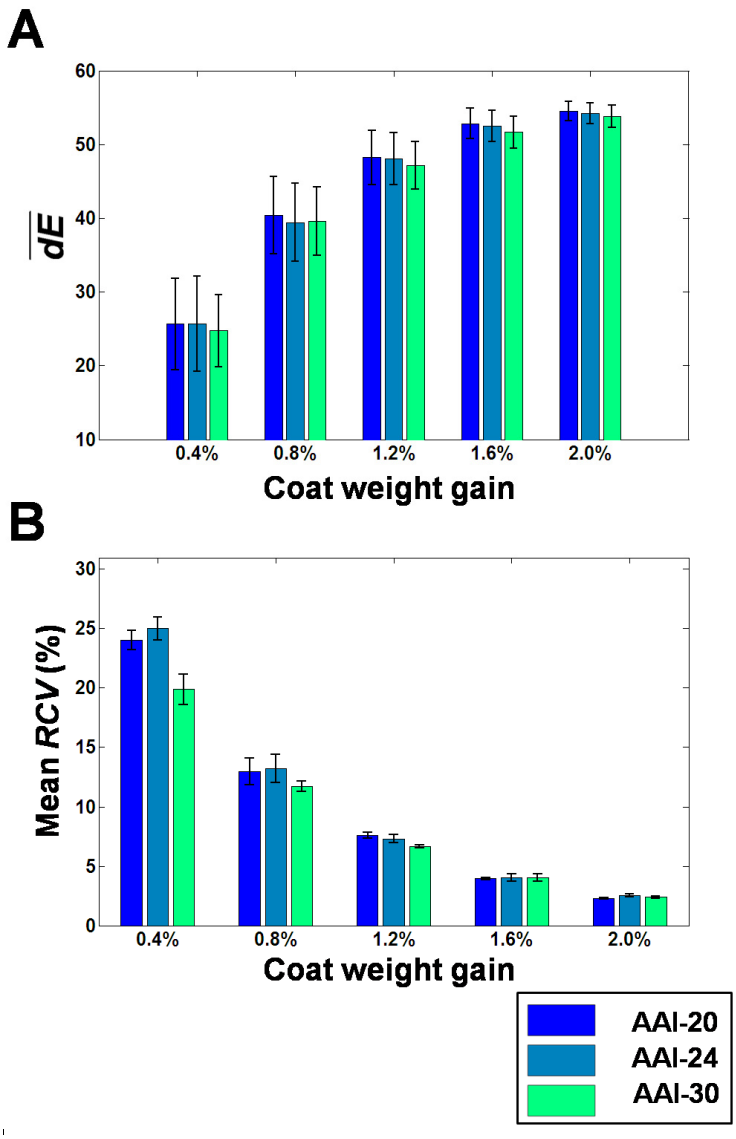

Figure 52. (A) Trends of mean colour difference ($\overline{dE}$) and (B) mean relative colour variation (*RCV*) of in-process samples obtained from AAI-20, AAI-24 and AAI-30

The *RCV* of in-process samples are shown in Figure 52B. As expected, an overall decreasing trend was observed for all three AAI settings with increased coverage of the particle surfaces by the colour pigment. Differences in *RCV* values of particles colour-coated at the three AAI settings also decreased with increase in coat weight gain and the differences may become negligible upon approaching complete coverage of the originally white particles by the colour pigment. The influence of AAI settings on particle coat uniformity would be less important at higher weight gains with sufficient improvement in the coverage of the colour coat.

F-test was used to compare the *dE* variances of colour-coated particles for statistical comparison of particle coat uniformity in terms of inter-particle colour variance. As shown in Table 7, the *F-test* results on comparison of *dE* variances for the three AAI settings were consistent for 0.4% -1.2% coat weight gains. For instance, samples under AAI-30 had significantly lower *dE* variances than those under AAI-20 and AAI-24 while *dE* variances for AAI-20 and AAI-24 were not statistically significant. In contrast, the *F-test* results for the last two coat weight gains were neither consistent with one another nor with those of the first three coat weight gains. As coating is a layering process, the *F-test* results should, in theory, be consistent for all weight gains. Nevertheless, it is also known that the sensitivity of tristimulus colourimetry decreased with saturation of the colour pigment on the particle surfaces (Chan *et al.*, 2001). The observed inconsistency in *F-test* results for the last two coat weight gains may be attributed to decreased discrimination sensitivity induced by colour saturation when coat weight gains were higher than 1.2%. Statistical

comparison of *dE* variances should thus be carried out on *dE* variances of colour-coated particles with lower coat weight gains (i.e. up to the first three coat weight gains) for the following reasons: firstly, the impact of AAI settings on particle coat uniformity is expected to be greater at low coat weight gains and/or during the early stages of the coating process, and secondly, *dE* variances employed for statistical comparison should be within the sensitive detection range of the tristimulus colourimeter.

Consequently, based on *F-test* results and *RCV* trend of the first three coat weight gains, the colour coats of particles coated at AAI-30 were found to have greater coat uniformity than those coated at AAI-20 and AAI-24, and the differences in *dE* variances were statistically significant. AAI-20 produced particles with higher degree of coat uniformity than those coated at AAI-24. Although the difference was not statistically significant, the trend in variance difference was consistently detected for the first two coat weight gains.

4.G.3. Influences of particle recirculation within partition column and particle mass flow rate on coat uniformity

Although particle recirculation within the partition column is considered a major variability source, one-way ANOVA did not show any statistically significant differences in particle recirculation probabilities of the three AAIs (p=0.4776). Hence, the differences in coat uniformity observed within the scope of this investigation could not be solely attributed to particle recirculation within the partition column.

Table 7. Two-sample *F-test* results for *dE* variance of in-process samples

Coat weight gains	***F-test* results ($df_1=df_2=599$,under χ^2-distribution)**	**Particles coated under**		**Particles coated under**		**Particles coated under**	
		AAI-20	**AAI-24**	**AAI-20**	**AAI-30**	**AAI-24**	**AAI-30**
0.4%	Variance of *dE*	38.5004	41.4601	38.5004	24.2068	41.4601	24.2068
	F	1.0768		1.5905		1.7127	
	p-value	0.3650		0.0000 *		0.0000 *	
0.8%	Variance of *dE*	27.4914	27.7351	27.4914	21.4154	27.7351	21.4154
	F	1.009		1.2837		1.2951	
	p-value	0.9140		0.0023 *		0.0016 *	
1.2%	Variance of *dE*	13.3606	12.4787	13.3606	10.5113	12.4787	10.5113
	F	1.0707		1.2711		1.187	
	p-value	0.4036		0.0034 *		0.0360 *	
1.6%	Variance of *dE*	4.3505	4.5537	4.3505	4.8100	4.5537	4.8100
	F	1.0467		1.1056		1.0563	
	p-value	0.5765		0.2194		0.5030	
2.0%	Variance of *dE*	1.6118	1.9761	1.6118	2.2882	1.9761	2.2882
	F	1.2261		1.4196		1.1579	
	p-value	0.0128 *		0.0000 *		0.0730	

"*"denotes significant statistical test result under significance level $\alpha = 0.05$.

For particle mass flow rate, AAI-20 was reported to induce the highest particle mass flow rate followed by AAI-24 and AAI-30 due to the Venturi effect (Chan *et al.*, 2006). According to the verified model developed by Turton *et al.*, higher mass flow rate within the partition column reduced cycle-time and particles underwent more coating cycles through the spray zone, thus achieving more rapid attainment of uniform coat layers (Crites and Turton, 2005). For example, AAI-20 resulted in higher mass flow rate within the partition column than the other two AAIs, and AAI-24 generated higher mass flow rates than AAI-30; hence, the most uniform coat layer was expected by using AAI-20 followed by AAI-24 and "least" uniform by AAI-30. However, in this investigation, AAI-30 was found to produce particles with the best coat uniformity followed by AAI-20 and AAI-24, which was contradictory to the coat uniformity results predicted by mass flow rate.

4.G.4. Influence of annular bed flow patterns on coat uniformity

The particle coat uniformity trend could be better explained if the influence of annular bed flow pattern was taken into consideration. For a clearer picture of annular bed material flow orientations, streamlines were calculated from the velocity vectors and illustrated in Figure 51B.

Bubbles induced generalized mixing when AAI-20 was used (Figure 51A(i)). Particles near the bubble head were pushed aside by the rising bubble. As a result, they moved downwards around the bubble and mixed with particles drawn in the wake of the bubble. With bubbles bursting through the annular bed surface, the particles on the bed surface were carried upwards into the air and subsequently fell back onto the annular bed. Moreover, it was observed

that bubble generation spots were generally random at the base of the bed. Streamlines (Figure 51B(i)) showed that generalized mixing was the main characteristic for this type of annular bed flow pattern. In this situation, particles from the bottom of the bed were brought upwards, against the general queue in the staging area for entry into the partition column for coating. This somewhat disrupted the orderliness of the coating process, resulting in a wider cycle-time distribution and hence, a less favourable effect on coat uniformity.

Localized bubbling fluidization occurred when AAI-24 was used. The larger insert diameter of AAI-24 caused a decrease in air flow rate through the annular bed. This caused a lower pressure drop through the bed. The pressure dropped below the critical bubbling fluidization pressure in the middle of the bed, confining the bubbling fluidization to the bottom half of the annular bed. Streamlines derived showed that only the bottom half of the bed underwent fluidization (Figure 51B(ii)). It was also observed that the bubbles were typically generated at the same vicinity, bringing some particles upwards to the middle of the bed. Upon dissipation of the bubbles, those particles that were lifted upwards by the bubbles moved downwards again as a result of gravity and circulation effects of particles entering the partition column. In the event that the particles encountered another developing bubble, their localized circulation path may yet be disrupted. As such, with localized fluidization, there was a tendency for a portion of particles to be confined to the bottom half of the annular bed, undergoing localized circulation but in effect isolated from the systematic coating cycles for extended time. The localized fluidization stagnated particle flow near the product chamber wall but caused

accelerated feeding in the near partition column region, resulting in a wider particle cycle-time distribution. Hence, this type of annular bed flow pattern may lead to relatively less uniform deposition of coat material onto particle surfaces. Under the conditions tested, this adverse effect of localized fluidization could have suppressed the constructive effect of higher particle mass flow rate, resulting in lower degree of coat uniformity for particles coated using AAI-24 than for the other AAIs.

Plug flow was observed when AAI-30 was used. This was associated with a further decrease in the air flow rate through the annular bed. Streamlines plotted showed uniform, downward particle movement without fluidization (Figure 51B(iii)). This flow pattern was due to gravity and the Venturi effect (Chan *et al.*, 2006), which drew particles into the upbed region via the partition column inlet. Under this flow pattern, freshly coated particles moved in pulsating rhythm smoothly and orderly via the staging annular bed for another coating cycle. This "queue system" ensured each particle underwent similar coating cycles and thus a narrow particle cycle-time distribution. The influence of the "queue system" exceeded the negative effects of lower particle mass flow rate, producing particles with better coat uniformity than the other two AAIs.

However, if air flow rate passing through the annular bed was further decreased or if there was insufficient load to maintain a uniform downward flow, motionless "dead" zones could occur at the bottom of the annular bed. "Dead" zones are highly undesirable as a large portion of particles would then

be isolated from systematic circulation without equal chances of entering the coating cycles. Hence, although plug flow can potentially confer superior coat uniformity, it is important to take precautions such that the operating process conditions are monitored to avoid conditions promoting "dead" zones at the bottom of the annular bed.

4.G.5. Significance of annular bed flow pattern

Three types of annular bed flow patterns were classified and their influences on coat uniformity assessed. As bottom spray fluid bed coating is a complex process, it was necessary to explore the extent of the annular bed flow pattern's impact on particle coating and the factors governing the extent. The coat variance induced by particle cycle-time distribution, which was mainly caused by the annular bed flow pattern in this study, can be estimated by the following equation (Cheng and Turton, 2000a):

$$Var_{coat} \approx \sqrt{\frac{Var(t)}{T_{coating} \times E(t)}} \tag{38}$$

where Var_{coat} is the coat variance due to cycle-time distribution, $Var(t)$ is the variance of particle cycle-time, $E(t)$ is mean particle cycle-time and $T_{coating}$ is coating time. According to Cheng and Turton (Cheng and Turton, 2000a; 2000b), the standard deviation of particle cycle-time, $Std(t)$, is proportional to $E(t)$, i.e. $Std(t) \approx 0.5E(t)$. Thus, the coat variance due to cycle-time distribution can be rewritten as:

$$Var_{coat} \approx \sqrt{\frac{0.5Std(t)}{T_{coating}}} \tag{39}$$

Consequently, the influence of annular bed flow pattern depends on standard deviation of particle cycle-time *Std(t)* and coating time $T_{coating}$.

In view of the analysis above, it is expected that the influence of annular bed flow pattern would decrease with longer coating time (more coating cycles). Doubling coating time would decrease annular bed induced coat variance by about 30% (Cheng and Turton, 2000a). Therefore, the influence of annular bed flow pattern may be more evident in the following cases. The first case is low coat weight gain coating processes. For instance, for the purpose of reducing porosity, preventing dust formation during handling, decorative coating and certain sustained release applications, the target coat thickness may be as thin as 5 μm (Lehmann, 1994). A coat layer of 5 μm is approximately equivalent to 1.1% weight gain for 1000 μm particles. Second, the influences of annular bed flow patterns also depend on the solids content of the coating fluids as well as spray rate. Annular bed flow patterns tend to have greater influence in the case of high solids content coating fluids and high spray rates. For instance, 10% w/w coating fluid was used in this study. However, coating fluids of 20% w/w or higher may be used for coating. Organic solvent-based coating fluids can be sprayed at much faster spray rates than aqueous based coating fluids (Fukumori, 1994). In such cases, annular bed flow patterns would tend to exert greater influences on coat uniformity. Third, annular bed flow pattern is expected to have greater impact in large scale coaters where the particles have larger spaces to move about in when driven by rising bubbles, thus larger *Std(t)* values would be expected for a bubbling annular bed. Although a longer coating time may be used to counteract the negative influence of a bubbling

annular bed, longer coating time and the use of more coating material would not be advantageous. Thus, for large scale bottom spray fluid bed coating, it is desirable to monitor annular bed flow pattern to ensure that conditions are suitable for the presence of plug flow.

The capability of coating particles with a wider size distribution is another advantage of plug flow. Due to agitation and drag force of fluidization air, particles with a wide size distribution may segregate in the annular bed. In the case of segregation, larger particles tended to be less affected and remained in the bed surface region while smaller particles were fluidized; therefore, larger particles are less likely to join the coating cycle, leading to non-uniform coat. If plug flow is present, the tendency for segregation can be avoided with the uniform, downward particle movement in the annular bed.

Moreover, plug flow may also be helpful in controlling the development of electrostatic charges as attrition is alleviated in the annular bed. For the purpose of summarizing the influences of different annular bed flow patterns on coat uniformity and to provide a general guidance on the coating process operation, a schematic qualitative representation of annular bed flow regimes versus their respective impact on coat uniformity was plotted (Figure 53).

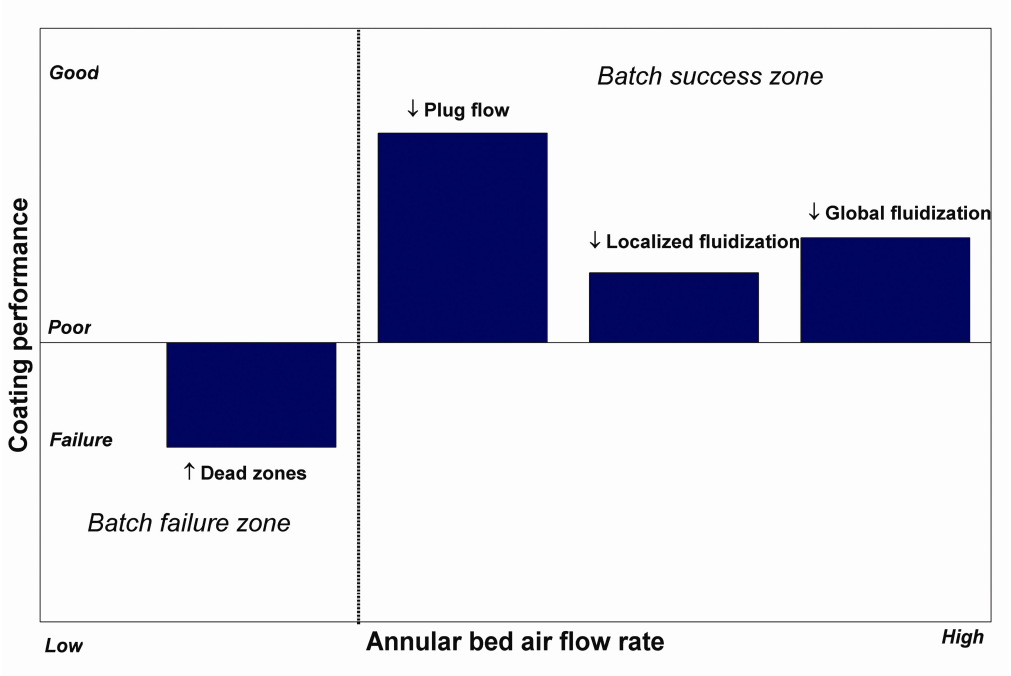

Figure 53. Schematic representation of annular bed flow regimes with their influences on coating performance

4.G.6. Feasibility of monitoring annular bed flow pattern in large scale coating process

As demonstrated, the overall annular bed flow patterns could be visualized by using a transparent acrylic product chamber, and coating parameters adjusted to induce the desired annular bed flow pattern accordingly. Nevertheless, it is not practical to capture whole annular bed flow in a large scale coater with a stainless steel product chamber. The observation window with a process monitoring camera would be the main mode to monitor annular bed flow pattern. With only a segment rather than the whole annular bed flow pattern visualized, it was necessary to investigate whether the overall flow pattern could be inferred from a limited local flow pattern detected through an observation window.

In this investigation, 10 cm by 10 cm window images were selected from the bottom of the original images, simulating images taken through an observation window in a large scale coater. The window images underwent the same image processing procedures as described earlier. The sample velocity vectors from the simulated observation window (Figure 54) showed considerable differences for the three different types of flow patterns. For global fluidization (Figure 54A), velocity fields underwent drastic changes both in amplitude and orientation. For localized fluidization (Figure 54B), besides considerable orientation changes in a minority of the velocity vectors, most of the velocity vectors were observed to point downwards with small variations in amplitude. For plug flow, all the velocity vectors varied only in amplitude, indicating pulsed downward particle movement in the annular bed (Figure 54C).

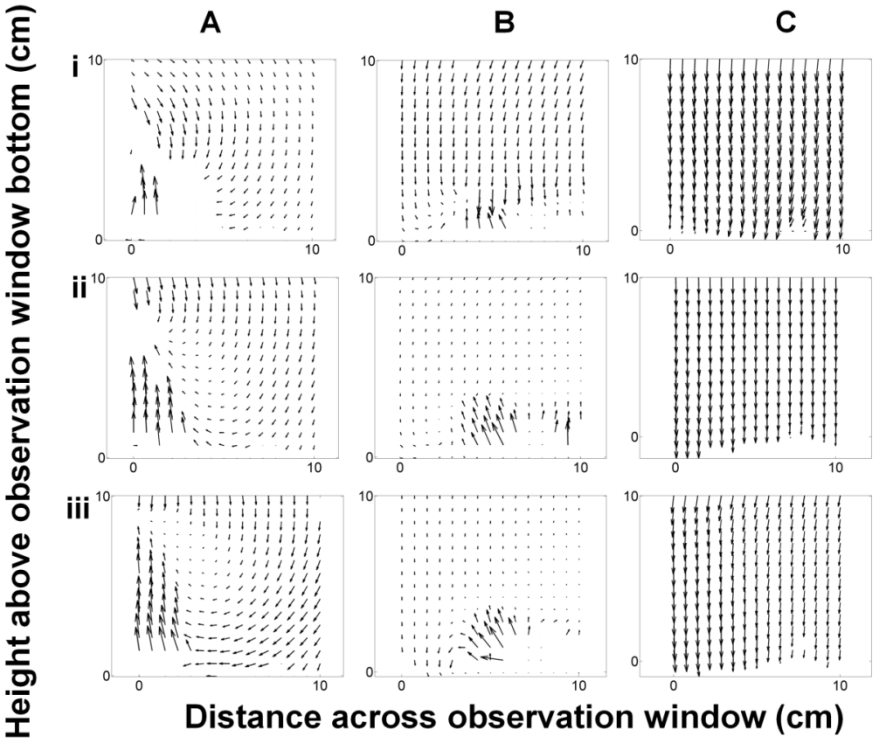

Figure 54. PIV results from 10 cm by 10 cm observation window of (A) global fluidization, (B) localized fluidization and (C) plug flow at time point of (i) 0 ms, (ii) 20 ms and (iii) 40 ms

In order to investigate how the characteristics of the different annular bed flow patterns could be further quantified, time series velocity vectors of three randomly chosen positions in the annular bed were employed as shown in Figure 55. The horizontal vector component was plotted against the vertical vector component. For global fluidization, points scattered randomly on the plane, suggesting a random nature in both orientation and magnitude of particle movement.

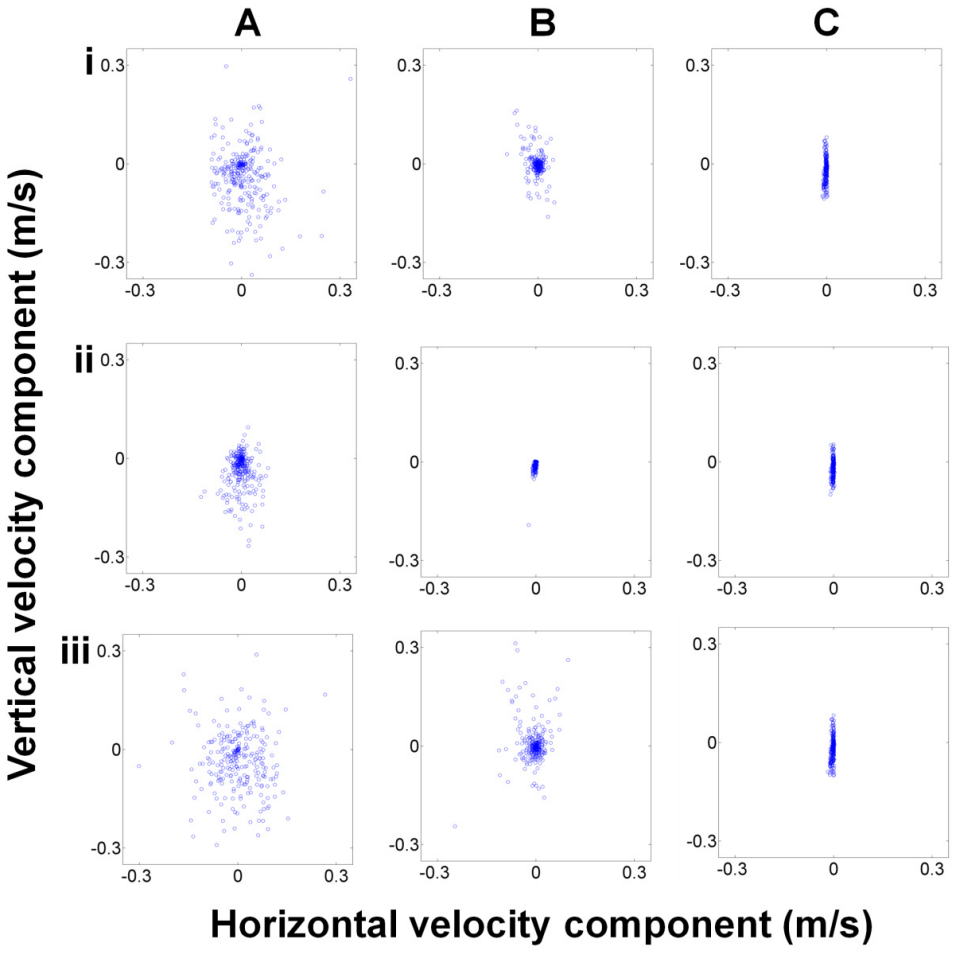

Figure 55. Scatter plot of time series velocity vectors from three randomly chosen locations (i, ii and iii) under (A) global fluidization, (B) localized fluidization and (C) plug flow

For localized fluidization, particle movement orientation was random but the magnitude of particle movement was lower than that in global fluidization. The vertical velocity components showed the tendency of some particles to stagnate (Figure 55B(ii)). This can be attributed to the dissipation of fluidization in the middle of the annular bed, inducing localized particle circulation in the lower annular bed. The localized particle circulation within the lower annular bed may block some particles from moving downwards, causing some particles to be motionless along the vertical direction for an extended time. This also further demonstrated the undesirable effect of localized fluidization. For plug flow, points were observed to locate near a vertically directed line, indicating uniform particle movement orientation (Figure 55C). It is also worthwhile to note that the randomness of particle movement generally decreased with an increase in AAI diameter. This is because with the increased AAI open area, less fluidization air passed through annular bed, causing more and more uniform particle movement in the annular bed.

In order to differentiate plug flow from the other flow patterns, standard deviation of the time series velocity orientation (*STSO*) was proposed for quantifying the randomness of velocity orientation.

$$STSO = \sqrt{\frac{1}{n}\sum_{i=1}^{N}\left(\hat{\varphi}_i - \mu_{\varphi}\right)^2} \tag{40}$$

where $$\hat{\varphi}_i = \begin{cases} \varphi_i & \text{for} \varphi_i \le \pi \\ \varphi_i - \pi & \text{for } \varphi_i > \pi \end{cases} \tag{41}$$

where φ_i is the i^{th} velocity orientation; $\hat{\varphi}_i$ is the i^{th} velocity orientation mapped to the region between 0 to π; and μ_φ is the mean of mapped velocity orientation. This definition is similar to standard deviation and is a measurement of the spread of velocity orientation in the annular bed region. The orientation relative to π was used as the measurement of velocity orientation as the particle velocity along the same line did not contribute to the measurement of spreadness. The orientation of plug flow was much more uniform than those of the other flow patterns.

Hence, plug flow was identified by images from the observation window and analysis of time series velocity orientation data. Moreover, white seed particles were used in this investigation mainly due to the need for a large area to be illuminated. Seed particles are not needed with intense local illumination over a small area in a practical application. In such cases, pulsed lighting synchronized with image capture may be advantageous. Thus, it is possible to use an observation window and a camera to monitor and ensure that a suitable annular bed flow pattern is present during a coating process. As such, a real-time annular bed flow pattern monitoring based PAT tool could be developed.

CHAPTER 5. CONCLUSION

CHAPTER 5. CONCLUSION

Following the results and discussion presented in the previous chapter, the conclusion of the investigations would be given in this chapter. The limitations, significance and possible future work would also be further discussed.

5.A. Spheronization process

By using the verified method of high speed video imaging coupled with Ferret diameter measurement, the remodelling theory was found to be more reflective of particle growth kinetics in the spheronization process. The current remodelling theory was also refined to incorporate a wider range of process conditions. A better understanding of the spheronization process was gained and foundations for developing process models as well as better process control.

The particle motion in the near plate region can be divided into two kinetic zones: fluidization zone and frictional motion zone. By using dimensionless surface plots, both mean speed and mean granular temperature in the near plate region were found to be indicative of particle growth kinetics. Endpoint of phase II growth can be reliably detected by monitoring particle mean speed as well as granular temperature in the near plate region. The changes in bed surface mean speed were also found to be reflective of particle growth kinetics. Hence, for timely detection of endpoint of phase II growth, monitoring of bed surface mean speed may be a third method.

5.B. Bottom spray fluid bed coating

High speed video imaging and ensemble correlation PIV were found to be able to quantify particle recirculation within the partition column with adequate accuracy and robustness. One key contribution of this part is that online particle recirculation measurement was made possible for the first time. By using the developed process analyzer, cluster formation and drag reduction was found to the mechanism of particle recirculation within the partition column, thus laying foundations for small particle coating and coating apparatus modification.

In the third investigation on bottom spray fluid bed coating, a visiometric process analyzer was developed to measure particle MFR online. Compared with the previous mass flow measurement method (Chan *et al.*, 2006), the proposed method is non-invasive and more accurate. In the last investigation, annular bed flow patterns were classified and their influences on coat uniformity were determined. The study was the first to demonstrate the influences of annular bed flow patterns on coat uniformity experimentally. Results from simulated observation window also showed the feasibility of monitoring annular bed flow pattern online.

5.C. Limitations and future directions

The experiments carried out in this PhD project were limited to pilot scale pharmaceutical processes and the feasibility for large-scale application was not tested. For large-scale bottom spray fluid bed coating, the proposed visiometric process analyzers need to be modified. High intensity laser light may be used for illumination considering the depth of field issue in a large-

scale coating process. The representative observation position for a large-scale manufacture process may also need to be chosen with care. As the aim of this project was to investigate the feasibility and potential of using visiometric process analyzers for monitoring pharmaceutical processes, only prototypes of visiometric process analyzers were developed. Hence, the detailed engineering limitations in view of their large-scale application are beyond the scope of this study.

The requirement of high speed computing is a restriction of visiometric process analyzers, especially for the ensemble correlation PIV method and flow pattern detection in the spheronization process. Distributed computing or parallel computing may be used to increase the computing speed significantly. Some computing systems include hundreds of computing cores and hence, could be extremely efficient in computing repetitive tasks such as correlation and pattern matching. For bottom spray fluid bed coating, although the particle motion was not significantly affected by the usage of coating fluid, the application of the proposed visiometric process analyzers in a large-scale manufacturing process may encounter view shielding problem. In view of this potential problem, a retractable image probe, which has clean-in-place property, may be developed for application in the large-scale manufacturing process.

Although extrusion-spheronization and bottom spray fluid bed coating have been used in the pharmaceutical industry for more than 30 years, work related to their process modelling and system identification have been limited. This

PhD study, which focused on measuring basic physical phenomena in these processes could serve as part of the basis for their system identification, process modelling and process control. Future research work should focus on developing control models for spheronization and bottom spray fluid bed coating based on visiometric process analyzers. Self-tuning control systems for spheronization and coating may then be attempted based on the control models, visiometric process analyzers and feedback process analyzers.

REFERENCES

Adrian, R. Double exposure, multiple-field particle image velocimetry for turbulent probability density. Opt Laser Eng. 1988; 9 (3-4): 211-228.

Adrian, R.J. Particle-imaging techniques for experimental fluid mechanics. Annu Rev Fluid Mech. 1991; 23 (1): 261-304.

Adrian, R.J., Yao, C.S. Pulsed laser technique application to liquid and gaseous flows and the scattering power of seed materials. Appl Optics. 1985; 24 (1): 44-52.

Andersson, M., Folestad, S., Gottfries, J., Johansson, M.O., Joseffson, M., Wahlund, K.G. Quantitative analysis of film coating in a fluidized bed process by in-line NIR spectrometry and multivariate batch calibration. Anal Chem. 2000; 72 (9): 2099-2108.

Andersson, M., Josefson, M., Langkilde, F.W., Wahlund, K.G. Monitoring of a film coating process for tablets using near infrared reflectance spectrometry. J Pharm Biomed Anal. 1999; 20 (1-2): 27-37.

Baert, L., Remon, J.P. Influence of amount of granulation liquid on the drug release rate from pellets made by extrusion spheronisation. Int J Pharm. 1993; 95 (1-3): 135-141.

Baert, L., Remon, J.P., Elbers, J.A.C., Van Bommel, E.M.G. Comparison between a gravity feed extruder and a twin screw extruder. Int J Pharm. 1993; 99 (1): 7-12.

Baert, L., Remon, J.P., Knight, P., Newton, J.M. A comparison between the extrusion forces and sphere quality of a gravity feed extruder and a ram extruder. Int J Pharm. 1992; 86 (2-3): 187-192.

Basu, P. Quality by design - comparison with other industries. 2009 AAPS Annual Meeting and Exposition. Los Angeles.

Bechgaard, H., Ladefoged, K. Distribution of pellets in the gastrointestinal tract. The influence on transit time exerted by the density or diameter of pellets. J Pharm Pharmacol. 1978; 30 (11): 690-692.

Bi, H.T., Grace, J.R., Zhu, J.X. On types of choking in pneumatic systems. Int J Multiphas Flow. 1993; 19: 1077-1192.

Bi, X., Pugsley, T. Investigation of the Sources of Variability in the Wurster Coater: Analysis of Particle Cycle Times using PEPT. In: Berruti, F., editor. 2007 ECI Conference on The 12th International Conference on Fluidization - New Horizons in Fluidization Engineering; Vancouver, Canada: The Berkeley Electronic Press; 2007. pp. 431-440.

Bodmeier, R. Tableting of coated pellets. Eur J Pharm Biopharm. 1997; 43 (1): 1-8.

Bokkers, G.A., Van Sint Annaland, M., Kuipers, J.A.M. Mixing and segregation in a bidisperse gas-solid fluidised bed: a numerical and experimental study. Powder Technol. 2004; 140 (3): 176-186.

Brennen, C.E. Fundamentals of multiphase flow. New York: Cambridge University Press; 2005. pp. 127-154.

Brilliantov, N.V., Poschel, T. Granular gases - velocity distribution. Kinetic theory of granular gases. Oxford: Oxford University Press; 2004. pp. 51-104.

CDER, F.D.A. PAT — a framework for innovative pharmaceutical development, manufacturing, and quality assurance. 2004 [Accessed May 2008]; Available from: http://www.fda.gov/CDER/GUIDANCE/6419fnl.htm

Chan, L.W., Chan, W.Y., Heng, P.W.S. An improved method for the measurement of colour uniformity in pellet coating. Int J Pharm. 2001; 213 (1-2): 63-74.

Chan, L.W., Tang, E.S.K., Heng, P.W.S. Comparative study of the fluid dynamics of bottom spray fluid bed coaters. AAPS PharmSciTech. 2006; 7 (2): 9.

Chang, R.-K., Robinson, J.R. Sustained drug release from tablets and particles through coating. In: Lieberman, H.A., Lachman, L., Schwartz, J.B., editors. Pharmaceutical dosage forms - tablets 2ed. New York: Dekker; 1990. pp. 209-214.

Chen, C.-T. Linear system theory and design. 3rd ed. New York: Oxford University Press; 1999. pp. 1-4.

Cheng, X., Turton, R. The prediction of variability occurring in fluidized bed coating equipment. I. The measurement of particle circulation rates in a bottom-spray fluidized bed coater. Pharm Dev Technol. 2000a; 5 (3): 311-322.

Cheng, X., Turton, R. The prediction of variability occurring in fluidized bed coating equipment. II. The role of nonuniform particle coverage as particles pass through the spray zone. Pharm Dev Technol. 2000b; 5 (3): 323-332.

Cheremisinoff, N.P. Guidebook to extrusion technology. Englewood Cliffs, N.J.: Prentice Hall 1993. pp. 39-69.

Christensen, F.N., Bertelsen, P. Qualitative description of the Wurster-based fluid-bed coating process. Drug Dev Ind Pharm. 1997; 23 (5): 451-463.

Cole, G. Introduction and overview of pharmaceutical coating. In: Cole, G., editor. Pharmaceutical coating technology. Bristol: Taylor & Francis; 1995. pp. 1-5.

Conway, S., Lekhal, A., Khinast, J., Glasser, B. Granular flow and segregation in a four-bladed mixer. Chem Eng Sci. 2005 DEC 2005; 60 (24): 7091-7107.

Cooper, P. Practical solutions to critical solids handling problems. In: Hoyle, W., editor. Powders and solids : developments in handling and processing technologies. Cambridge, UK: Royal Society of Chemistry; 2001. pp. vii.

Corvari, V., Fry, W.C., Seibert, W.L., Augsburger, L. Instrumentation of a high-shear mixer: Evaluation and comparison of a new capacitive sensor, a watt meter, and a strain-gage torque sensor for wet granulation monitoring. Pharm Res. 1992; 9 (12): 1525-1533.

Crites, T., Turton, R. Mathematical model for the prediction of cycle-time distributions for the Wurster column-coating process. Ind Eng Chem Res. 2005 JUL 6 2005; 44 (14): 5397-5402.

Dallavalle, J.M. Micromeritics: the technology of fine particles. 2nd ed. New York: Pitman; 1948. pp. 12-40.

Darelius, A., Lennartsson, E., Rasmuson, A., Niklasson Bjorn, I., Folestad, S. Measurement of the velocity field and frictional properties of wet masses in a high shear mixer. Chem Eng Sci. 2007; 62 (9): 2366-2374.

Di Felice, R. The voidage function for fluid-particle interaction systems. Int J Multiphas Flow. 1994; 20 (1): 153-159.

Dry, R.J., White, C.C. Gas-solid contact in a circulating fluidized bed: The effect of particle size. Powder Technol. 1992; 70 (3): 277-284.

Duran, J. Sands, powders, and grains. New York: Springer; 2000. pp. 9-12.

Duran, J. Static and dynamic arching effect in granular materials. In: Herrmann, H.J., Hovi, J.-P., Luding, S., editors. Physics of dry granular media. Boston: Kluwer academic publishers; 1998. pp. 197-216.

Duursma, G.R., Glass, D.H., Rix, S.J.L., Yorquez-Ramirez, M.I. PIV investigations of flow structures in the fluidised bed freeboard region. Powder Technol. 2001; 120 (1-2): 2-11.

Elsinga, G.E., Wieneke, B., Scarano, F., Schro?der, A. Tomographic 3D-PIV and applications. Topics in Applied Physics; 2008. p. 103-125.

Erkoboni, D.F. Extrusion/Spheronization. In: Ghebre-Sellassie, I., editor. Pharmaceutical extrusion technology. New York: Marcel Dekker; 2003. pp. 277-318.

FDA. ICH Q8. 2006 [Accessed June 2010]; Available from: http://www.fda.gov/downloads/RegulatoryInformation/Guidances/ucm128029.pdf

Fitzpatrick, S., Ding, Y., Seiler, C., Lovegrove, C. Positron emission particle tracking studies of a Wurster process for coating. Pharmaceutical Technology. 2003; 27 (9): 5.

Fukumori, Y. Coating of multiparticulates using polymeric dispersions - formulation and process considerations. In: Ghebre-Sellassie, I., editor. Multiparticulate oral drug delivery. New York: Marcek Dekker; 1994. pp. 79-111.

Fukumori, Y., Ichikawa, H., Jono, K., Takeuchi, Y., Fukuda, T., Jm. Computer-simulation of agglomeration in the wurster process. Chem Pharm Bull (Tokyo). 1992 Aug; 40(8):2159-2163.

Funck, J.A.B., Schwartz, J.B., Reilly, W.J., Ghali, E.S. Binder effectiveness for beads with high drug levels. Drug Dev Ind Pharm. 1991; 17(9):1143-1156.

Geldart, D., Rhodes, M.J. From minimum fluidization to pneumatic transport-a critical review of the hydrodynamics. In: Basu, P., editor. Circulating Fluidized Bed Technology : Proceedings of the First International Conference on Circulating Fluidized Beds; 1985; Halifax, Nova Scotia, Canada: Pergamon Press; 1985. pp. 21-31.

Ghebre-Sellassie, I., Knoch, A. Pelletization techniques. In: Swarbrick, J., editor. Encyclopedia of pharmaceutical technology. 3 ed. New York: Informa Healthcare; 2007. pp. 2651-2663.

Ghebre-Sellassie, I., Martin, C., Elliot, B. Continuous melt spheronization apparatus and process for the production of pharmaceutical pellets. U.S. Patent Office, 2007: 20070264328.

Gonzalez, R.C., Woods, R.E., Eddins, S.L. Image segmentation. Digital image processing using MATLAB. Upper Saddle River, N. J.: Pearson Prentice Hall; 2004a. pp. 378-425.

Gonzalez, R.C., Woods, R.E., Eddins, S.L. Morphological image processing. Digital image processing using MATLAB. Upper Saddle River, N. J.: Pearson Prentice Hall; 2004b. pp. 334-377.

Grace, J.R., Bi, H. Introduction to circulating fluidized beds. In: Grace, J.R., Avidian, A. A., Knowlton, T. M., editors. Circulating fluidized beds. London: Blackie academic & professional; 1997. pp. 10-14.

Grace, J.R., Tuot, J. A theory for cluster formation in vertically conveyed suspensions of intermediate density Transactions of the institution of chemical engineers. 1979; 57: 5.

Haddish-Berhane, N., Jeong, S.H., Haghighi, K., Park, K. Modeling film-coat non-uniformity in polymer coated pellets: A stochastic approach. Int J Pharm. 2006; 323 (1-2): 64-71.

Hall, H.S., Pondell, R.E. The Wurster process. In: Kydonieus, A.F., editor. Controlled Release Technologies: Methods, Theory and Applications. Boca Raton, Florida: CRC Press; 1980. pp. 133-154.

Harrison, P.J., Newton, J.M. and Rowe, R.C., Convergent flow analysis in the extrusion of wet powder masses. J. Pharm. Pharmacol. 1984; 36 (12): 796-798.

Harrison, P.J., Newton, J.M., Rowe, R.C. The characterization of wet powder masses suitable for extrusion/spheronization. J Pharm Pharmacol. 1985;37 (10): 686-691.

He, Y., Qin, S., Lim, C., Grace, J. Particle-velocity profiles and solid flow patterns in spouted beds. Can J Chem Eng. 1994 AUG 1994;72 (4): 561-568.

Hellen, L., Ritala, M., Yliruusi, J., Palmoroos, P., Kristoffersson, E. Process variables of the radial screen extruder: I. Production capacity of the extruder and the properties of the extrudate. J Pharm Technol Int. 1992; 4: 50-60.

Heng, P.W.S., Chan, L.W., Tang, E.S.K. Use of swirling airflow to enhance coating performance of bottom spray fluid bed coaters. Int J Pharm. 2006; 327 (1-2): 26-35.

Heng, P.W.S., Wan, L.S.C., Tan, Y.T.F. Relationship between aggregation of HPMC coated spheroids and tackiness/viscosity/additives of the coating formulations. Int J Pharm. 1996; 138 (1): 57-66.

Heng, P.W.S., Wong, T.W., Shu, J.J., Wan, L.S.C. A new method for the control of size of pellets in the melt pelletization process with a high shear mixer. Chem Pharm Bull (Tokyo). 1999; 47 (5): 633-638.

Hill, D.T., Daniel; Walters, Geoffrey; Lai, Wing; Sharp, Kendra. Volumetric 3-component velocimetry (V3V) measurements of the turbulent flow in stirred tank reactors. 14th International Symposium on Applications of Laser Techniques to Fluid Mechanics. Lisbon; 2008.

Hogan, J.E. Modified release coating. In: Cole, G., editor. Pharmaceutical coating technology. London: Taylor & Francis; 1995. pp. 411.

Horio, M. Hydrodynamics. In: Grace, J.R., Avidan, A.A., Knowlton, T.M., editors. Circulating fluidized beds. London: Blackie academic & professional; 1997. pp. 21-42.

Hu, X., Cunningham, J.C., Winstead, D. Study growth kinetics in fluidized bed granulation with at-line FBRM. Int J Pharm. 2008; 347 (1-2): 54-61.

Jenkins, J.T. Kinetic theory for nearly elastic spheres. In: Herrmann, H.J., Hovi, J.P., Luding, S., editors. Physics of dry granular media. London: Kluwer academic publishers; 1998. pp. 353-369.

Jones, D. Air suspension coating for multiparticulates. Drug Dev Ind Pharm. 1994; 20(20): 3175-3206.

Jones, R., and Soille, P, Periodic lines: definition, cascades, and application to granulometrie, Pattern Recogn Lett. 1996; 17(10): 1057-1063.

Karlsson, S., Bjorn, I., Folestad, S., Rasmuson, A. Measurement of the particle movement in the fountain region of a Wurster type bed. Powder Technol. 2006; 165 (1): 22-29.

Keane, R.D., Adrian, R.J. Theory of cross-correlation analysis of PIV images. Appl Sci Res. 1992; 49 (3): 25.

Kilian, C.T. Modern control technology : components and systems 2nd ed. Novato, CA Delmar Thomson Learning; 2000. pp. 453-500.

Kirsch, J.D., Drennen, J.K. Near-infrared spectroscopic monitoring of the film coating process. Pharm Res. 1996; 13 (2): 234-237.

Koenig, D.M. Practical control engineering: a guide for engineers, managers, and practitioners. New York: McGraw-Hill; 2009. pp. 1-16.

KuShaari, K., Pandey, P., Song, Y., Turton, R. Monte Carlo simulations to determine coating uniformity in a Wurster fluidized bed coating process. Powder Technol. 2006; 166 (2): 81-90.

Lehmann, K. Coating of multiparticulates using polymeric solutions - formulation and process considerations. In: Ghebre-Sellassie, I., editor. Multiparticulate oral drug delivery. New York: Marcel Dekker; 1994. pp. 51-76.

Li, J., Tung, Y., Kwauk, M. Method of energy minimization in multi-scale modeling of particle-fluid two-phase flow. In: Basu, P., Large, J.F., editors. Circulating fluidized bed technology II : proceedings of the Second International Conference on Circulating Fluidized Beds; 1988; Compiègne, France: Pergamon Press; 1988. pp. 89-103.

Liew, C., Chua, S., Heng, P. Elucidation of Spheroid Formation With and Without the Extrusion Step. AAPS PharmSciTech. 2007; 8 (1): 10.

Liew, C.V. Spheronization by rotary processing - a single step process for producing spheroids [PhD thesis]: National University of Singapore; Singapore, 1996. pp. 81-116.

Liew, C.V., Gu, L., Soh, J.L.P., Heng, P.W.S. Functionality of cross-linked polyvinylpyrrolidone as a spheronization aid: A promising alternative to microcrystalline cellulose. Pharm Res. 2005; 22 (8): 1387-1388.

MathWorks, T. Matlab distributed computing server. [Accessed September 2010]; Available from: http://www.mathworks.com/products/distriben/

McGinity, J.W., Zhang, F. Melt-extrudated controlled-release dosage forms. In: Ghebre-Sellassie, I., editor. Pharmaceutical extrusion technology. New York Marcel Dekker; 2003. pp. 183-206.

Merkus, H.G. Particle size, size distributions and shape. Particle Size Measurements: Fundamentals, Practice, Quality Springer Netherlands; 2009. pp. 13-42.

Mori, N., Chang, K.-A. MPIV - Matlab PIV toolbox. 2006. [Accessed July 2010]; Available from: http://www.oceanwave.jp/softwares/mpiv/index.php?FrontPage

Nakahara, N. Method and apparatus for making spherical granules. US Patent Office, 1966: 3277520

Nakayama, Y., Boucher, R.F. Introduction to Fluid Mechanics. New York: John Wiley & Sons Inc; 1999. pp. 42.

Nasr, M. FDA's quality initiatives: An update. [Accessed May 2009]; Available from: http://www.gmp-compliance.com/daten/download/FDAs_Quality_Initiative.pdf

Newton, J.M. Extrusion and extruders. In: Swarbrick, J., editor. Encyclopedia of pharmaceutical technology 3rd ed. New York: Informa Healthcare; 2007. pp. 1713-1727.

Nilpawar, A., Reynolds, G., Salman, A., Hounslow, M. Surface velocity measurement in a high shear mixer. Chem Eng Sci. 2006; 61 (13): 4172-4178.

Ostendorf, M., Schwedes, J. Application of Particle Image Velocimetry for velocity measurements during silo discharge. Powder Technol. 2005; 158(1-3):69-75.

Otsu, N., A threshold selection method from gray-level histograms. IEEE T Sys Man Cyb.1979; 9(1): 62-66.

Palmer, S.E., Seville, J.P.K., Ingram, A., Fitzpatrick, S., Fan, X. Tracking pellet motion in a Wurster coater using positron emission. Fifth World Congress on Particle Technology (Session #158b) on 2006 AIChE Spring National Meeting; 2006; Orlando: American Institute of Chemical Engineers; 2006.

Parker, M.D., Rowe, R.C., G., U.N. Mixer torque rheometry: a method of quantifying the consistency of wet granulations. Pharm Technol Int. 1990; 2: 50-62.

Porter, S.C. Coating of tablets and multiparticulates. In: Aulton, M.E., editor. Aulton's pharmaceutics - the design and manufacture of medicines. New York: Churchill Livingstone; 2007. pp. 500-514.

Raffel, M., Willert, C.E., Wereley, S.T., Kompenhans, J. Particle image velocimetry : a practical guide. 2nd ed. New York: Springer; 2007. pp 138.

Ramaker, J., Jelgersma, M., Vonk, P., Kossen, N. Scale-down of a high-shear pelletisation process: Flow profile and growth kinetics. Int J Pharm. 1998; 166 (1): 89-97.

Reynolds, A.D. A new technique for the production of spherical particles. Manuf Chem Aerosol News. 1970; 41: 4.

Ritala, M., Holm, P., Schaefer, T., Kristensen, H.G. Influence of liquid bonding strength on power consumption during granulation in a high shear mixer. Drug Dev Ind Pharm. 1988; 14 (8): 1041-1060.

Romero-Torres, S., Perez-Ramos, J.D., Morris, K.R., Grant, E.R. Raman spectroscopy for tablet coating thickness quantification and coating

characterization in the presence of strong fluorescent interference. J Pharm Biomed Anal. 2006; 41 (3): 811-819.

Rowe, R.C. The effect of the molecular weight of ethyl cellulose on the drug release properties of mixed films of ethyl cellulose and hydroxypropyl methylcellulose. Int J Pharm. 1986; 29 (1): 37-41.

Rowe, R.C. Spheronization: a novel pill-making process? Pharm Int. 1985; 6: 119-123.

Rowe, R.C., Parker, M.D. Mixer torque rheometry: an update. Pharm Technol Int. 1994; 3: 74-82.

Saadevandi, B.A., Turton, R. The application of computer-based imaging to the measurements of particle velocity and voidage profiles in a fluidized bed. Powder Technol. 1998; 98 (2): 183-189.

Schaafsma, S., Marx, T., Hoffmann, A. Investigation of the particle flowpattern and segregation in tapered fluidized bed granulators. Chem Eng Sci. 2006; 61 (14): 4467-4475.

Slominski, C., Niedostatkiewicz, M., Tejchman, J. Application of particle image velocimetry (PIV) for deformation measurement during granular silo flow. Powder Technol. 2007; 173 (1): 1-18.

Soille, P. Erosion and dilation. Morphological image analysis: principles and applications. New York: Springer; 2003a. pp. 63-104.

Soille, P. Geodesic transformations. Morphological image analysis: principles and applications. 2nd ed. Berlin; New York: Springer; 2003b. pp. 219-238.

Soille, P. Introduction. Morphological image analysis: principles and applications. 2nd ed. Berlin; New York: Springer; 2003c. pp. 1-12.

Soille, P. Opening and closing. Morphological image analysis: principles and applications. 2nd ed. Berlin; New York: Springer; 2003d. pp. 105-137.

Sriamornsak, P., Burton, M.A., Kennedy, R.A. Development of polysaccharide gel coated pellets for oral administration: 1. Physico-mechanical properties. Int J Pharm. 2006; 326 (1-2): 80-88.

Sriamornsak, P., Nunthanid, J., Luangtana-anan, M., Puttipipatkhachorn, S. Alginate-based pellets prepared by extrusion/spheronization: A preliminary study on the effect of additive in granulating liquid. Eur J Pharm Biopharm. 2007; 67 (1): 227-235.

Sudsakorn, K., Turton, R. Nonuniformity of particle coating on a size distribution of particles in a fluidized bed coater. Powder Technol. 2000; 110 (1-2): 37-43.

Suh, Y.K. Multi-frame MQD-PIV. KSME Int J. 2003; 17 (10): 1552-1562.

Taberlet, N., Richard, P., Jenkins, J.T., Delannay, R. Density inversion in rapid granular flows: The supported regime. European Physical Journal E. 2007; 22 (1): 17-24.

Tang, E.S.K., Chan, L.W., Heng, P.W.S. Coating of multiparticulates for sustained release. American Journal of Drug Delivery. 2005; 3 (1): 17-28.

Tang, E.S.K., Wang, L., Liew, C.V., Chan, L.W., Heng, P.W.S. Drying efficiency and particle movement in coating--Impact on particle agglomeration and yield. Int J Pharm. 2008; 350 (1-2): 172-180.

Tian, Y., Peng, X.F. Analysis of particle motion and heat transfer in circulating fluidized beds. Int J Energ Res. 2004; 28:287-297.

Vervaet, C., Baert, L., Risha, P.A., Remon, J.-P. The influence of the extrusion screen on pellet quality using an instrumented basket extruder. Int J Pharm. 1994; 107 (1): 29-39.

Walter, K. Apparatus for coating solid particles. US Patent Office, 1998: 5718764

Wan, L.S.C., Heng, P.W.S., Liew, C.V. Spheronization conditions on spheroid shape and size. Int J Pharm. 1993; 96 (1-3): 59-65.

Wang, X.S., Gibbs, B.M. Hydrodynamics of a circulating fluidized bed with secondary air injection. Circulating fluidized bed technology III: Pergamon Press; 1991. pp. 225-230.

Wen, C.Y., Yu, Y.H. A generalized method for predicting the minimum fluidization velocity. AICHE J. 1966; 12: 610-612.

Westerweel, J. Digital particle image velocimetry: theory and application [PhD thesis]. Technische Universiteit Delft; the Neverthelands, 1993.

Wildman, R.D., Martin, T.W., Huntley, J.M., Jenkins, J.T., Viswanathan, H., Fen, X. *et al.* Experimental investigation and kinetic-theory-based model of a rapid granular shear flow. Journal of Fluid Mechanics. 2008; 602: 63-79.

Wirth, M. Instrumental colour measurement: A method for judging the appearance of tablets. J Pharm Sci. 1991; 80 (12): 1177-1179.

Woodcock, J. The Concept of Pharmaceutical Quality. Americian pharmaceutical review. 2004; 7 (6): 6.

Wurster, D.E., Lincllof, J.A., inventors; Particle Coating Apparatus. US Patent Office, 1966: 3241520

Xu, M., Turton, R. A new data processing technique for noisy signals: application to measuring particle circulation times in a draft tube equipped fluidized bed. Powder Technol. 1997; 92 (2): 111-117.

Yang, N., Wang, W., Ge, W., Li, J. CFD simulation of concurrent-up gas–solid flow in circulating fluidized beds with structure-dependent drag coefficient. Chem Eng J. 2003; 96: 71-80.

Young, D.F., Munson, B.R., Okiishi, T.H. A brief introduction to fluid mechanics. 3rd ed. Hoboken: Wiley; 2004. pp. 362-406.

Yu, L.X. Pharmaceutical Quality by Design: Product and Process Development, Understanding, and Control. Pharm Res. 2008; 25 (4):11.

Zhang, W.N., Johnsson, F., Leckner, B. Fluid-dynamic boundary layers in CFB boiler. Chem Eng Sci. 1995; 150 (2): 201-210.

LIST OF PUBLICATIONS

JOURNAL PUBLICATIONS:

[1] **L.K. Wang**, P.W.S. Heng, C.V. Liew, Online monitoring of particle mass flow rate in bottom spray fluid bed coating – development and application. ***International Journal of Pharmaceutics***, accepted, publication in progress, DOI:10.1016/j.ijpharm.2010.05.044

[2] **L.K. Wang**, P.W.S. Heng, C.V. Liew, Classification of annular bed flow patterns and investigation on their influence on the bottom spray fluid bed coating process. ***Pharmaceutical Research***, **27**, pp. 756-766

[3] C.V. Liew, **L.K. Wang**, P.W.S. Heng, Development of a visiometric process analyzer for real-time monitoring of bottom spray fluid bed coating, ***Journal of Pharmaceutical Sciences***, **99,** pp. 346-356.

[4] E.S.K. Tang, **L.K. Wang**, C.V. Liew, L.W. Chan, P.W.S. Heng, Drying efficiency and particle movement in coating—Impact on particle agglomeration and yield, ***International Journal of Pharmaceutics,*** **350,** pp.172-180.

POSTER PRESENTATIONS:

[1] **L.K. Wang**, C.V. Liew, P.W.S. Heng, Visiometric mapping of particle recirculation within the partition column of bottom spray fluid bed coater, AAPS 2009 Annual Conference, Los Angeles, USA

[2] **L.K. Wang**, C.V. Liew, P.W.S. Heng, Annular bed flow patterns and their influences on pellet coat uniformity, AAPS 2009 Annual Conference, Los Angeles, USA

[3] **L.K. Wang,** M.M. Chua, C.V. Liew, A study on the role of swirling fin in precision coating process, Asian Association of Schools of Pharmacy 2009 Conference, Penang, Malaysia

[4] **L.K. Wang**, C.V. Liew, P.W.S. Heng, Development of a high speed imaging and image analysis based process analyzer for bottom spray fluid bed coating process, AAPS 2008 Annual Conference, Atlanta, USA

[5] **L.K. Wang**, C.V. Liew, P.W.S. Heng, Prediction of particle movement using air velocity patterns within the partition column of bottom spray fluid bed coater, Asian Association of Schools of Pharmacy 2007 Conference, Makati City, Philippines

ORAL PRESENTATIONS:

[1] "Mapping process variability sources of bottom spray fluid bed coating using visiometric process analyzer". On: ***Pharmaceutical Seminar 2009: Process analytical technology, the way forward to quality excellence 27-28 July 2009***, NUSS Guild House, NUS, Singapore

[2] "Development of a visiometric process analyzer for real-time monitoring of particle mass flow rate in bottom spray fluid bed coating". On: ***The 4th International Pharmaceutical Symposium. 24-26 Sept 2009***, Shanghai, China